Anton Michaël (Twanne) Roor

Assessing beach width dynamics through earth observations

Deltares
Enabling Delta Life

TU Delft

Assessing beach width dynamics through earth observations

By

Anton Michaël (Twanne) Roor

in partial fulfilment of the requirements for the degree of

Master of Science
in Civil Engineering

at the Delft University of Technology,
to be defended publicly on Thursday March 3, 2022, at 16:15.

Student number:	1533614	
Thesis committee:	Prof.dr.ir. S.G.J. Aarninkhof,	TU Delft
	Dr.ir. S. de Vries,	TU Delft
	Ir. W.P. de Boer	Deltares, TU Delft
	Ir. G. Santinelli	Deltares
	Ir. G. Hagenaars	Deltares (former)

An electronic version of this thesis is available at http://repository.tudelft.nl/.

Cover: source: ESA / André Kuipers, acquired from Netherlands Space Office

T̃U Delft

Preface

This thesis concludes the Master of Science programme in Hydraulic Engineering at the Faculty of Civil Engineering and Geosciences at the Delft University of Technology. This research has been carried out with the support of Rijkswaterstaat and research institute Deltares, for which I am grateful.

First of all, I would like to thank the members and former members of my graduation committee; Stefan Aarninkhof, Sierd de Vries, Wiebe de Boer, Giorgio Santinelli, and Gerben Hagenaars. Thank you for your invaluable guidance, constructive feedback, and counselling. Most of all I would like to thank you for giving me the chance to finish my thesis after a long break and for the confidence you kept in my capabilities, which I often found difficult to maintain.

Special thanks to Joep Keijsers for providing the measurement data of his research on the interaction between sedimentation and vegetation on a multi-annual time scale at Ameland.

Furthermore, I'm very grateful to my employer, Van den Herik, and especially to Isolde, Jan, and Roger, for giving me the opportunity to work part-time so that I could complete my thesis.

Also, I would like to express my sincere gratitude to the Fundatie van Renswoude fonds for their support, for without it, I probably would not have been able to complete the MSc Programme.

Karel Karsen, thank you for all the talks we had the past *few* years. Thank you for your great advice, your ability to help me put things in perspective, and the confidence you always kept in me. I hope you have a phenomenal retirement.

Finally, I would like to sincerely thank my dear family and friends, since I do not know where I would be without them. Thank you, moeder, for your endless care and for always being there for me. Many thanks to my brother and sisters, my great friends and Marte for all your support the past few years. Special thanks go out to Bram, Emilie, Lexy, Marijke, and especially Martine for helping me with my thesis and pulling me through these last weeks. It has been a rough ride, but you all made it so much more bearable. Sometimes I forget with how many you are. Thank you.

Twanne Roor
Rotterdam, February 2022

Abstract

Coasts are constantly under the pressure of hydrodynamic conditions such as waves, tides, and storms. In the Netherlands, sand nourishments are executed every few years in order to maintain the country's sandy beaches for purposes of safety, recreation, and ecology. In order to determine where to carry out these nourishments, the whole sandy coastline of the Netherlands is measured annually by Rijkswaterstaat. This annual survey, called JAarlijkse KUStmetingen (JARKUS), monitors where (increasing) erosive trends appear or persist and, due to its timespan (dating back to 1843), is a valuable dataset to understand the evolution of the Dutch coast. However, this measurement survey is restricted to its annual frequency and is costly. The use of optical satellite imagery for measuring land cover types and geographic features is rapidly becoming more popular due to their high temporal frequency and relatively low costs (due to the public availability of some satellite missions, such as NASA's Landsat and ESA's Sentinel-2 missions). This research studied the possibilities of using optical satellite imagery for measuring beach width dynamics in addition to the existing measurement campaigns.

In this study, we derived the Satellite-Derived Beach Width (SDBW) as the cross-shore distance between the Satellite-Derived Shoreline (SDS) and the Satellite-Derived Vegetation line (SDV). We adopted a widely used and validated method for SDS detection and adapted this method to establish the SDV detection method. The SDS and SDV are derived from optical satellites by deriving vectors from the border between two contrasting land cover types that are identified by differences in (sun)light reflectance values. The SDS and is derived from the contrast between water and land, the SDV from the contrast between and sand/sediment and vegetation. The SDBW data was measured from both composite and individual satellite images. The different techniques are suited for different applications, and both have their advantages and disadvantages. A composite image is an image that is composed of a sequence of individual satellite images available within a set window. E.g., a composite is the average image of all those images. Recent research showed that, at the cost of temporal resolution, composite images are suited for analysis of long-term (structural) shoreline trends since they mitigate certain factors influencing image quality (such as clouds and cloud shadows, waves and tides, and satellite instrument errors). Individual images are better suited for analyses of short-term dynamics since they provide instantaneous measurement data. However, they are hampered more by the factors mentioned above, and hence need to be screened before use.

In order to assess the performance of the SDBW, we compared the results of up to 34 years of satellite data (Landsat 5, Landsat 8, and Sentinel-2) with JARKUS data at the sandy beach located on the northern coast of the island of Ameland. This island is located at the interface of the Wadden Sea and the North Sea in the north of the Netherlands. The island is characterized by a *dynamic* western area subject to strong currents due to its neighbouring tidal inlet and the landing of an offshore sandbank several decades ago. The larger eastern part of the coast (the *uniform* area) is less dynamic and is mainly influenced by the eastward spreading of the landed sandbank.

We compared the offsets, standard deviations, and dynamics of the SDV with the Dunefoot, the SDS with the Mean Low Water (MLW) and Mean High Water (MHW) and the SDBW with the Total Beach Width and Dry Beach Width. The Dunefoot, MLW and MHW are parameters defined as certain elevation levels that intersect elevation-based cross-shore beach profiles (transects). Here, the Dunefoot is defined at the +3m NAP elevation level, estimated to represent the approximate location of the break-in-slope between the flat beach and steep foredunes in the Netherlands. The MLW and MHW represent the positions of the mean low and mean high water elevation levels at the cross-shore profile. The distance between the MLW and Dunefoot is called the Total Beach Width, and the distance between the MHW and Dunefoot is called the Dry Beach Width. The Total Beach Width is the sum of the Dry Beach Width and the Wet Beach Width (e.g., the area between MLW and MHW or the intertidal area). Hence, it should be taken into account that the compared

parameters are physically not identical, but the comparison with JARKUS was nonetheless expected to provide an excellent first impression of the SDBW's performance.

The comparison between the SDBW with the JARKUS data gave a lot of insight and confidence in the performance of the SDBW detection method. Overall, we found that the SDBW size and dynamics are (much) more similar to the Dry Beach Width than the Total Beach Width. We relate this to the degree of correspondence of the SDS with MHW. An important remark when looking at the results is that there are considerable differences between the offsets and dynamics measured at the dynamic and uniform areas of the Ameland beach. The data from both composite and individual images showed that, on average, there is a consistent offset between the SDV and Dunefoot of 40 to 50 meters at the uniform area, where there is a typical beach-dune profile. This offset is primarily related to the actual in-situ distance between the two parameters, with the SDV located landward of the Dunefoot, rather than the method's accuracy. The SDS is located, on average, between MLW and MHW (following the tidal variation) and has a strong bias towards MHW. This bias is likely related to (a combination of) wave run-up, soil moisture of the beach and the local beach profile (slope). This bias is particularly apparent at the uniform area where the longshore averages of the offsets between SDS and MHW vary between +12 and -37 meters, and the longshore averages of the offsets between SDS and MLW vary between 120 and 178 meters. The bias towards the MHW results in the previously mentioned bias of the SDBW towards the Dry Beach Width.

The beach width dynamics were analysed by deriving the trends from the time series of positional data. At the uniform area, the trends of the SDBW and JARKUS parameters showed strong similarities in trend direction and order of magnitude. The SDBW and JARKUS parameters showed fewer similarities at the dynamic area, but some correspondence was definitely noticeable. The SDV and Dunefoot dynamics acted as a predictor of the other. In other words, at some locations, the most seaward vegetation limit (measured by the SDV) significantly expanded in seaward direction several years before the position of the +3m elevation contour (the Dunefoot) caught up with this seaward shift. The latter can be explained by the natural relationship between sedimentation and vegetation; when (dune or marsh) vegetation gets the chance to develop in a seaward direction, sedimentation accumulates between the new vegetation, reinforcing the development of both sedimentation and vegetation. This process works both ways, be it with a certain delay of the other parameter. The measured SDS dynamics corresponded to the MLW and (mostly) MHW dynamics mainly in direction (growth or decay) but less in magnitude. Overall, at Ameland, the shoreline dynamics dominate the SDBW dynamics.

The outcome of this research provides a first impression of the potential functionality of the SDBW measurement method. This research shows that with the developed SDV detection method, it is possible to obtain an accurate position of the vegetation line from both composite and individual images, given that the images are of good enough quality. Based on the Ameland case study results, we conclude that the SDBW, derived from the SDV and SDS, is a good proxy for measuring beach width and beach width dynamics. At dynamic beaches, it is less clear how the beach width is defined, and significant differences might be present between the SDBW and in-situ measurements. It is essential to keep in mind that this is not necessarily related to the accuracy of the SDBW detection method. In general, we can conclude that the SDBW method can become a complementary measurement method for assessing data on beach width dynamics in addition to traditional measurement surveys.

For the SDBW method to be generally embraced as a coastal measurement tool, various actions must be carried out. First, a direct comparison of the SDBW data from composite and individual images should be executed with matching study period and satellite image type. Since in this research, a comparison was made of two datasets with different study periods and satellite image types. Subsequently, additional case studies in the Netherlands must further validate the tool and assist in optimizing the algorithm settings and quality/accuracy of the measurement data. Although we are confident about the performance of the SDV, the accuracy of the SDV detection should be assessed more thoroughly with high-resolution in-situ vegetation

cover data if available. Since the SDV is a new parameter, it has not yet been validated much with detailed in-situ data other than this study, in contrast with the SDS which has been validated sufficiently in other studies. In addition, we suggested several ideas to optimise the detection process and the pre- and post-processing of the image data by using more advanced alternative algorithms and mathematical techniques. Lastly, the applicability of the SDBW should be investigated for locations worldwide with different geographic characteristics and features. We are confident that the SDBW tool has the potential to measure beach width (dynamics) at sandy beaches of different characteristics all around the world after sufficient validation has been achieved. The latter will enable countries where traditional measurement surveys are less accessible or too costly to study the state of local beaches at a very low cost. In time, the pixel resolution and return period of publicly available optical satellites will improve, resulting in higher spatial and temporal resolution of the measurement data, overall providing a higher measurement accuracy, and enabling more detailed research on beach width dynamics.

Contents

1 Introduction

The state of Earth's sandy beaches is vital to a large part of the global population. Primarily because a stable dune-beach system can ensure safety against the forces of the sea; but also, a clean and wide beach can be just as vital to business owners that are dependent on sufficient people coming to the beaches near their businesses; not to mention the importance of a healthy beach to the local biodiversity of a coastal area. The Netherlands, as one of the most densely populated countries in the world, depends heavily on the health and stability of its coastal system. The country's coast is divided into three distinct types of coastal zones: the Wadden Sea barrier islands, the relatively straight coast of North and South Holland and Zeeland's Delta Area, known as the Wadden Coast, Holland Coast and Delta Coast, respectively. Most of the country's population and economic value are located directly behind the beach-dune system of the Holland Coast. For a long time, especially after the 1953 disaster, Dutch coastal policy mainly focused on flood protection (van Koningsveld & Mulder, 2004). The implementation of so-called "hard" engineering measures such as sea dikes, dams and storm surge barriers was common practice. In the late twentieth century, the soft engineering approach, i.e., widening and raising the beach through sand nourishments, gradually became the new standard for maintaining the Dutch coast and protecting it against structural erosion. Figure 1 depicts the sandy beach on the northern coast of the Wadden Sea Island of Ameland and sand nourishments being carried out on the same beach. In 1990, the Dynamic Preservation program was initiated to provide a sustainable and environmentally friendly way of battling erosion and maintaining coastal safety (Roelse, 2002). The program proved successful (Roelse, 2002), and its execution was effective and efficient (DHV, 2005).

Figure 1 Sandy beach with vegetated dunes (left panel) and sand nourishments being carried out on the beach through pipes (right panel) in the context of Dynamic Preservation, on the north side of the Wadden Sea Island of Ameland, The Netherlands. From: "Kustonderhoud Waddeneilanden", source: Rijkswaterstaat, n.d. Public domain (CC0)

In assessing the state of a beach, various indicators are used to quantify relevant parameters of a beach. The beach width is one example of these so-called Coastal State Indicators (CSI's). The evolution of the beach width can provide information on coastal safety, ecology, and recreation. The beach width is essential for the dissipation of incoming wave energy in case of storm events. Also, de Vries et al. (2011) identified a positive trend between beach width and dune growth rate by suggesting a supportive relationship between beach width and dune stability. Furthermore, the beach width in terms of available visitor space is a critical factor of a beach its "*recreational carrying capacity*" (Jiménez et al., 2007). With this capacity, one can determine the recreational (and economic) potential for a beach.

Currently, there are a lot of recurring nourishment operations along various locations on the Dutch coast. On average, 12 million m^3 of sand is nourished yearly, either on the foreshore or directly on the beach (Rijkswaterstaat, 2017). Detailed measurement data in space and time is essential to increase knowledge on the effects of nourishments and optimise future applications. Apart from a few exceptions, such as the Sand

Engine mega-nourishment and the nourishments at the Hondsbossche and Pettemer Zeewering (HBPZ), there is no abundance of intra-annual measurement data on the development of beaches targeted by nourishments. In the Netherlands, the annual coastal monitoring survey JAarlijkse KUStmetingen (JARKUS) provides a detailed but fragmentary image of the Dutch coast; the survey does not measure intra-annual coastal dynamics. In their study on the initial spreading of the Sand Engine, which covered a monthly monitoring survey, de Schipper et al. (2016) observed that the most significant morphological changes occurred in the first six months. Valuable insight into these short-term morphological changes or coastal dynamics due to nourishments (or storms) is therefore not measured for most nourishments along the Dutch coast. The JARKUS data has proven valuable in understanding the Dutch coastal system and assessing the need and locations for regular nourishments. Nevertheless, a higher temporal and spatial resolution of coastal measurement data could further improve our understanding of the coastal system (e.g., short-term coastal dynamics, such as influences of storms and seasonal variation of the beach) and its response to nourishments (e.g., alongshore spreading).

From 1984 onwards, an increasing number of satellite missions constantly monitor the Earth. Until recently, the use of optical satellite imagery for coastal monitoring was hindered by high costs, pixel resolution and labour intensity of image processing (Boak & Turner, 2005; G. Hagenaars et al., 2018). For a long time, satellite data was restricted to governments and commercial institutions. Until 2008, when the National Aeronautics and Space Administration (NASA) and U.S. Geological Services (USGS) made the data collection of their Landsat satellite program available to the public, covering data of their satellite missions since 1984 (U.S. Geological Survey, 2015). A few years later, the European Space Agency (ESA) launched their Sentinel-2 mission, of which the data is also publicly available. These satellites capture images with an even higher pixel resolution (10m) and with shorter return periods (5 days) than the satellite missions from NASA (30m and 16 days). Satellites can have multi-spectral imagery of up to 0.31-meter pixel resolution. With Google Earth Engine™ (GEE) introduced recently, the ever-growing database of more than 37 years of optical satellite imagery is now easily accessible and processable. Since optical satellite images are freely available and can be as frequent as once every five days (ESA, 2018), it promises significant benefits in terms of temporal resolution relative to the traditional, less-frequent measurement campaigns for beach assessments. So that (the consequences of) short-term morphological events occurring on sandy beaches can potentially be captured in much more detail than previously possible.

1.1 Problem Definition

The use of nourishments to stabilise and preserve sandy beach-dune systems is becoming more and more common (de Schipper et al., 2016). Many morphological effects due to nourishments occur on shorter time scales than the recurrence window of standard coastal monitoring campaigns. In the Netherlands, measurement campaigns of higher frequency than the annual JARKUS survey are rare. Additionally, traditional in-situ and aerial surveys are expensive, time-consuming and they do not provide data of one time instant but of subsequent segments in time. Monitoring with a higher temporal resolution can prove to be very valuable to increase the knowledge of short-term morphological effects on beach widths. Furthermore, increasing quantitative insight into the physical mechanisms behind the natural and forced shore behaviour responsible for coastal change contributes to scientific and engineering improvements relevant to decision making and interventions related to coastal safety (Stive et al., 2002).

1.2 Research Objective

The main objective of this thesis is to explore the possibility of deriving beach width dynamics from optical satellite imagery in a semi-automated way. Beach width data in terms of position and dynamics will be compared to available in-situ data to help interpret the Satellite-Derived Beach Width (SDBW), assess its accuracy, and identify geographic conditions and algorithm settings influencing the detection process of the measurement method. The final goal is to assess the contribution of the new method to existing (in-situ) measurement options and to understanding coastal dynamics. This objective leads to the following main research question:

How can beach width (dynamics) be derived from optical satellite imagery along sandy coasts, and how do the results contribute to the current options for measuring and analysing beach width (dynamics)?

To formulate an answer to the main research question, we will first answer the following sub-questions:

1. *What are commonly used definitions for the beach width, and which are suitable for detection from optical satellite imagery?*

2. *How can beach width and beach width dynamics be derived from optical satellite imagery in a semi-automated way?*

3. *How does the Satellite-Derived Beach Width (SDBW) compare to beach widths from in-situ measurement surveys (such as JARKUS)?*

4. *How does the increased spatial and temporal resolution of the SDBW contribute to the existing (in-situ) possibilities for measuring and analysing beach width dynamics?*

5. *How do (local) geographic conditions and algorithm settings influence the detection process of the SDBW?*

1.3 Thesis Outline

The research questions are answered in the following chapters. Chapter 2 gives a literature review of user functions ascribed to beach width as a coastal indicator, presents commonly used physical definitions and describes different beach width measuring methods. Chapter 3 describes the methodology we follow for measuring the Satellite-Derived Beach Width from optical satellite imagery, introduces the case study of Ameland and presents the approach for comparing the SDBW data with the JARKUS data. Chapter 4 interprets the SDBW data and presents the results from the comparison between SDBW and JARKUS. In Chapter 5, we reflect on the results from the previous chapter and discuss several topics regarding the SDBW methodology, such as the method's potential, limitations, and applicability at alternate locations. Chapter 6 concludes this thesis by answering the research questions and presenting suitable recommendations for future research.

2 Literature review

This chapter presents relevant background information for the remainder of this research by (partly) answering research questions 1 and 2 as defined in Chapter 1. Section 2.1 presents functions, physical definitions, and surveying methods of the beach width. Section 2.2 introduces several core principles for measuring geographic features from optical satellite imagery. Section 2.3 elaborates on beach width dynamics and what to expect from the data when measuring beach width dynamics from optical satellite imagery.

2.1 Beach Width

Section 2.1.1 presents various examples of beach width functions commonly found in literature. In Section 2.1.2, we describe the different physical definitions used for the beach width. Common methods for measuring the beach width are presented in Section 2.1.3.

2.1.1 Functions

Coastal State Indicators (CSIs) are used to assess, inter-compare, and communicate coastal systems' dynamic-state and evolutionary trends (Davidson et al., 2007; Giardino et al., 2014). The beach width is one of these CSIs. In literature, beach width is related to user functions such as coastal safety, ecology, and recreation. Concerning coastal safety, the beach width is used as an indicator for flood risk (Durán et al., 2016), storm erosion (Harley et al., 2009), and dune development (Damsma, 2009; de Groot et al., 2012; de Vries et al., 2012; Nolet & Riksen, 2018; van Puijenbroek et al., 2017). Dune development is mainly controlled by the potential of aeolian sediment transport and the frequency and magnitude of storms (Damsma, 2009; Keijsers et al., 2014; Nolet & Riksen, 2018). The beach width is used as an indicator for the maximum wind fetch distance, over which sediment grains accumulate and transport towards the dunes. Additionally, the beach width is used to predict the amount of wave dissipation, to quantify the resilience against dune erosion during storms. Dugan et al. (2013) investigated the beach width in relation to ecological features using the "ecological envelope" concept. This parameter reflects a cross-shore habitat that beach biota (e.g., plants and animals) use to cope with constantly changing beach conditions. Decisio (2011) and Jiménez et al. (2017) studied the beach width in relation to recreation. Jiménez et al. (2017) studied the beach width to quantify the accommodation space for recreational activities under sea-level rise of Catalan beaches. Decisio (2011) determined minimum and optimum beach widths for different recreational use intensities for beaches in the Netherlands. They concluded that, depending on the use intensity, a beach requires minimum space for recreation (up to 50m), pavilions (20 to 30m) and accessibility for emergency services (10 to 20m). In summary, these studies show that the beach width is a relevant indicator for different user functions in the coastal zone.

2.1.2 Physical Definitions

Although the beach width is a widely used CSI in many countries, the applied definition is not universal. In its simplest form, the beach width is defined as the cross-shore distance between a seaward and a landward boundary. The demarcation of those boundaries varies widely amongst applications and countries. In the Netherlands, the beach width is often defined as the distance between a type of waterline and the dune foot (de Vries et al., 2012; Decisio, 2011; Keijsers et al., 2014). Figure 2 depicts a typical beach and foreshore profile used in Belgium and the Netherlands (Vandebroek et al., 2017). Commonly used demarcations of the waterline include Mean Sea Level (MSL), Mean Low Water (MLW) and Mean High Water (MHW). Which of these definitions is most suitable depends on the application. For example, when defining MHW as the seaward boundary of the beach width, one only looks at the dry beach, which is relevant for beach recreation (Decisio, 2011). In contrast, when defining MLW as the seaward boundary, one also includes the wet part of the beach (the intertidal area), which enables the assessment of aeolian transport to the dunes (de Vries et

al., 2014). Hence, in literature one universal beach width definition does not exist, and the use and definition of the beach width as a metric depends on the purpose you wish to analyse or quantify.
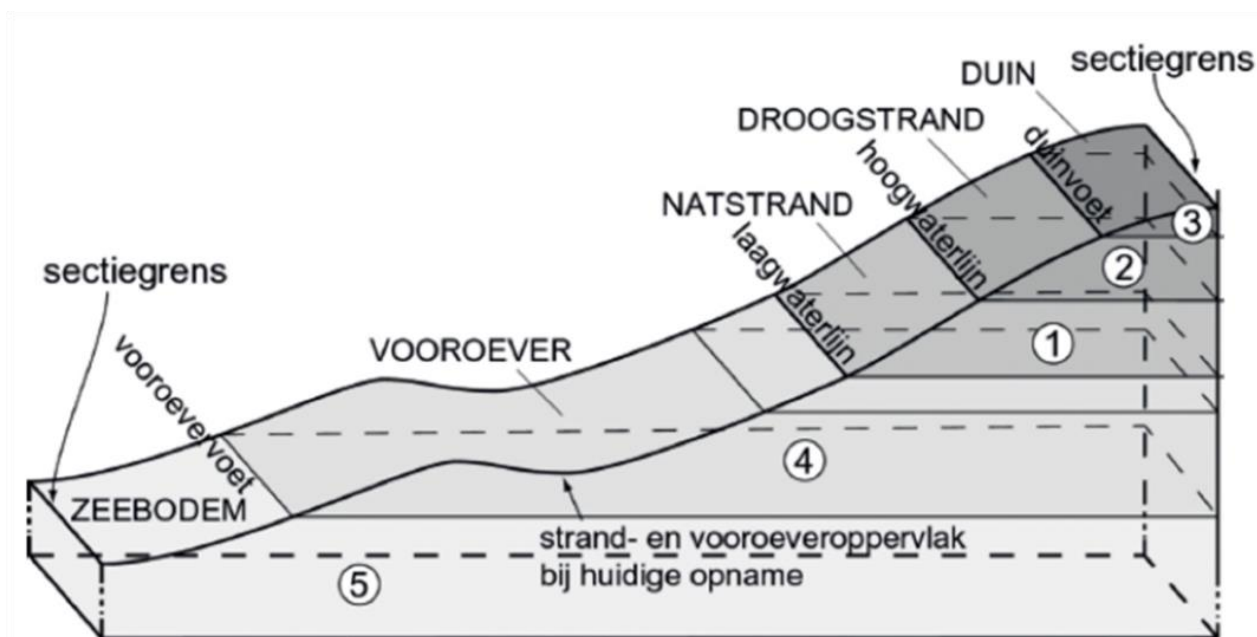

Figure 2 Beach and foreshore profile with Dutch definitions. Definitions translated from left to right: section border (sectiegrens), sea bottom (zeebodem), foreshore foot (vooroevervoet), foreshore (vooroever), beach- and foreshore surface at present survey (strand- en vooroeveroppervlak bij huidige opname), Mean Low Water (laagwaterlijn), Wet Beach (natstrand), Mean High Water (hoogwaterlijn), Dry Beach (droogstrand), Dunefoot (duinvoet), Dune (duin). Adjusted from Vandebroek et al. (2017)

Two commonly used definitions for the landward boundary of the beach width (of a dune-beach system) are the dune foot (or dune toe) and the vegetation line. The dune foot is defined as a (visible) break in slope representing the transition between the relatively flat beach to the steep foredunes (Battiau-Queney et al., 2003; de Vries et al., 2012; Guillén et al., 1999; Ruessink & Jeuken, 2002). This physical definition is referred to as the (*natural) dune foot* in this report. The position of this break in slope is somewhat arbitrarily. Therefore, in the Netherlands, the dune foot is often defined as the most seaward intersection of the cross-shore beach profile with a fixed elevation level above the local ordnance datum (Nieuw Amsterdams Peil, NAP). We refer to this definition of the dune foot as the *Dunefoot* in this report. This elevation level is commonly defined between 3 and 4 meters above NAP and is assumed to roughly correspond with the natural dune foot definition for the Dutch coast (Keijsers et al., 2015; Ruessink & Jeuken, 2002). For a study on the U.S. Pacific Northwest coast, Cohn et al. (2019) demarcate the landward boundary as the dune toe. Like the Dutch definition, they arbitrarily defined the dune toe at a fixed elevation level (+4m) relative to the local ordnance datum (NAVD88).

Another demarcation of the landward boundary of the beach width is the optically discernible vegetation line, which is defined in this research as the contour of the most seaward extent of high-density dune vegetation. In their research on the relationship between sedimentation and vegetation, Keijsers et al. (2015) found, at the sandy beaches of Ameland, that this contour is mainly located at the natural dune foot (e.g., the break in slope) but in some cases can also be located at a more seaward positioned foredune or embryo dune. In literature originating outside the Netherlands, the vegetation line is frequently used as a proxy for the shoreline because it is easily recognizable from aerial photos and it is a good indicator for coastal erosion (Adnan et al., 2016; Battiau-queney et al., 2003; Boak & Turner, 2005; Mahabot et al., 2017). Rader et al. (2018) used the vegetation line to quantify dune morphodynamics. Battiau-Queney et al. (2003) and Rader et al. (2018) mentioned that the vegetation line often coincides with the natural dune foot, suggesting that the vegetation line might be used as an alternative measure for the dune foot. Bauer & Davidson-Arnott (2003) demarcate the landward boundary as the dune line, which they simply refer to as either the geographic break in slope or

the limit of dune vegetation, basically stating they are the same geographic feature. One can, however, argue whether the latter statement is not too simply put and that it is very dependent on the examined location. In conclusion, we find that the elevation-based dune foot is often used as the landward demarcation of the beach width, and we find the optical discernible vegetation line as an alternative (of which the depiction is less unambiguous throughout literature).

2.1.3 Surveying methods
To quantify the beach width, we require measurements of beach profiles (i.e., elevation measurements), water levels or tidal datums, and vegetation (i.e., spatial spreading, type and density). The monitoring of coastal features is traditionally executed with in-situ geographic measurements and aerial photography (G. Hagenaars et al., 2018; van der Werff, 2019). These survey methods are often time-consuming and costly. Therefore, extensive monitoring campaigns of high spatial- and temporal resolution are rare. In recent years, the possibilities in monitoring have widely expanded with the advance of remote sensing techniques, such as Light Detection And Ranging (LIDAR), Radio Detection and Ranging (RADAR), video monitoring and optical satellite imagery (Boak & Turner, 2005; Gens, 2010). The ongoing evolution of these techniques has induced significant improvements for surveying methods in terms of spatial- and temporal resolution, accessibility, and reduction of costs.

This study is focused on the use of optical satellite imagery to monitor beach width dynamics. Feature detection through optical imagery is based on contrasts between solar radiation values reflected by different land cover types. In other words, to detect coastal features, we are looking at differences in the light reflectance spectrum. The previous section concluded that the beach width is a cross-shore distance between a type of shoreline and the dune foot or vegetation line. The shoreline can be detected from the difference between the light reflectance of land and water. The seaward contour of vegetated dunes (or other vegetated areas), e.g., the vegetation line, can be detected from the differences in solar radiation between sediment and vegetation. In conclusion, in this research, the beach width will be derived from the distance between an optically discernible shoreline and vegetation line, further referred to as the Satellite-Derived Shoreline (SDS) and Satellite-Derived Vegetation line (SDV). The beach width computed from these parameters, as the cross-shore distance between them, will be referred to as the Satellite-Derived Beach Width (SDBW). In the remainder of this thesis, these three parameters are sometimes comprehensively referred to as Satellite-Derived Parameters (SDPs).

2.2 Feature detection from optical satellite imagery
This section describes the current state of the art methods of deriving shorelines and vegetation lines from satellite imagery to derive beach width. We focus on optical detection methods, particularly optical feature detection from freely available satellite image data of NASA's Landsat 5 (1984-2011) and Landsat 8 (2013-present) missions, and ESA's Sentinel-2 (2015-present) mission. The images are accessed and processed with the cloud-based geospatial processing platform Google Earth Engine™.

2.2.1 Optical satellite imagery and current satellite missions
Optical remote sensing is based on the solar radiation reflected by different land cover types on the earth's surface. The radiation is captured in a wide range of wavelengths with multi- or hyperspectral sensors aboard satellites or other airborne agents. The spectral regions are divided into several bands (or bandwidths), representing, for example, the visible spectra (red, green, and blue) and invisible spectra (Near Infra-Red (NIR), Short-Wave Infra-Red (SWIR) and Thermal). Specialized algorithms based on combining variations of these bands, enable measuring geographic features and land cover types from optical satellite imagery. We describe the basic principle of two of those Algorithms in the following subsection (Section 2.2.2).

The NASA and ESA satellite missions carry the following multispectral sensors: the Landsat 5 carries the Thematic Mapper (TM), Landsat 8 carries the Operational Land Imager (OLI) and Sentinel-2A the Multi-Spectral Instrument (MSI). Depending on the satellite mission, the number of bands, the resolution at which the wavelengths are measured, and the designation of band numbers vary. Figure 3 shows the spectral bands of the multispectral sensors of Landsat 7, Landsat 8, and Sentinel-2. The spectral bands of Landsat 5's TM are the same as the bands of Landsat 7's Enhanced Thematic Mapper Plus (ETM+).
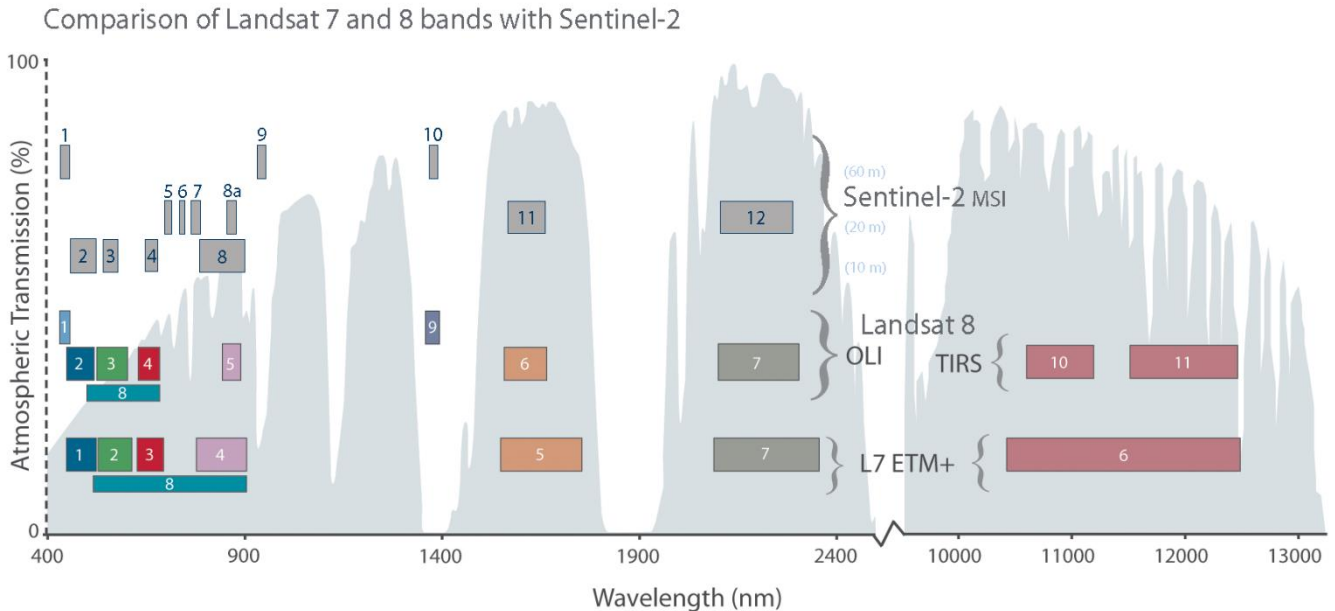
Figure 3 Comparison of Landsat 7 and 8 spectral bands with Sentinel-2. The spectral bands of Landsat 7's ETM+ are the same for Landsat 5's TM. From "Sentinel-2B succesfully launches", by NASA, 2017 (https://landsat.gsfc.nasa.gov/article/sentinel-2b-successfully-launches/). Public Domain.

NASA's Landsat 5 and Landsat 8 satellite sensors have a 30-meter pixel resolution for the visible, NIR and SWIR bands, and ESA's Sentinel 2 has a 10-meter pixel resolution for the visible and NIR bands (The European Space Agency (ESA), n.d.; U.S. Geological Survey, n.d.). The sensors installed on the mentioned satellite missions also measure other spectral bands but at lower pixel resolutions. Furthermore, the Landsat 5 and Landsat 8 missions both have a 16-day return period, and the dual Sentinel 2 satellites have a combined return period of 5 days (The European Space Agency (ESA), n.d.; U.S. Geological Survey, n.d.). There are two Sentinel-2 satellites with a 10-day return period

Since the introduction of the Google Earth Engine (GEE) API several years ago, the extraction and pre-processing of the ever-growing database of publicly available satellite imagery became much more accessible. The computational power of GEE's servers significantly reduces computation time by taking care of pre-processing steps with the cloud computing possibilities provided by the platform. For example, before extraction of Landsat or Sentinel-2 image collections from the GEE servers, satellite image pixels are transformed into spectral radiance values, these radiance values are then transformed to Top-Of-Atmosphere (TOA) reflectance values, and finally, the images are orthorectified, resulting in L1T TOA satellite images (G. Hagenaars et al., 2018). The resulting reduction of computation time per image decreases the time needed for obtaining the satellite (and coastal measurement) data and offers additional computation time for implementing other image-processing steps.

2.2.2 Land cover detection based on Normalised Difference Indices
A popular approach for land-cover detection from multispectral satellite imagery is the use of change indices that enhance the contrast between two (or more) spectral regions. One of the most commonly used change indices is the Normalised Difference Vegetation Index (NDVI). The NDVI is a graphical indicator that amplifies

the reflection of alive vegetation through a mathematical ratio, based on the differences between the Red and Near Infra-Red (NIR) spectral bands, see Eq. 1. This method builds on the fact that plant leaves effectively absorb radiation through the visible Red wavelengths and, on the other hand, strongly reflect the radiation through the invisible NIR wavelengths. The NDVI distributes the image pixels according to their reflectance values in a histogram ranging between -1 and +1. From these values, positive values represent vegetation.

$$NDVI = \frac{\lambda_{NIR} - \lambda_{RED}}{\lambda_{NIR} + \lambda_{RED}} \qquad \textit{Eq. 1}$$

The pixels representing a specific land cover type are distinguished from the pixel distribution with supervised or unsupervised threshold values. The NDVI is thus used to distinguish vegetated areas from non-vegetated areas. An alternative index applied to multispectral satellite imagery, used to distinguish land and water areas, is the Normalised Difference Water Index (NDWI). NDWI is based on the differences between the Green and Near Infra-Red (NIR) spectral bands, see Eq. 2.

$$NDWI = \frac{\lambda_{NIR} - \lambda_{GREEN}}{\lambda_{NIR} + \lambda_{GREEN}} \qquad \textit{Eq. 2}$$

2.2.3 Satellite-Derived Shoreline (SDS) – Detection and accuracy

Numerous researchers worldwide have researched the detection of sandy shorelines from optical imagery. The type of waterline these shorelines represent, together with the detection accuracy, varies for the different approaches followed.

The most basic definition of the shoreline is the interface between land and water (Dolan et al. (1980), as cited in Boak & Turner, (2005)). Depending on the hydrodynamic conditions, this interface can represent various waterlines, as mentioned in Section 2.1.2. Regarding the detection from optical satellite images, the choice for single images or composites of multiple images determines what the satellite-derived shoreline physically represents. The shoreline derived from a single image would represent the instantaneous waterline, corresponding to the hydrodynamic data at the moment of image acquisition. On the other hand, shorelines derived from composite images represent a wave- and tide-averaged waterline, likely resembling Mean Sea Level.

A popular approach to derive shorelines from optical imagery is based on the previously introduced NDWI to derive a threshold that separates the image pixels representing land and water areas. Otsu (1979) developed an unsupervised classification method to determine an adaptive threshold, which can be used to divide the NDWI pixel histogram to construct a binary image from the NDWI grey scale image. This binary image shows a clear separation between land and water, from which the SDS is then extracted as a vector from the border between the two areas. The latter is demonstrated by Hagenaars et al. (2018), see Figure 4 and Figure 5, who present a method based on the approach of Kuleli et al. (2011) for automated shoreline detection from optical satellite imagery extracted from and processed on the GEE servers.
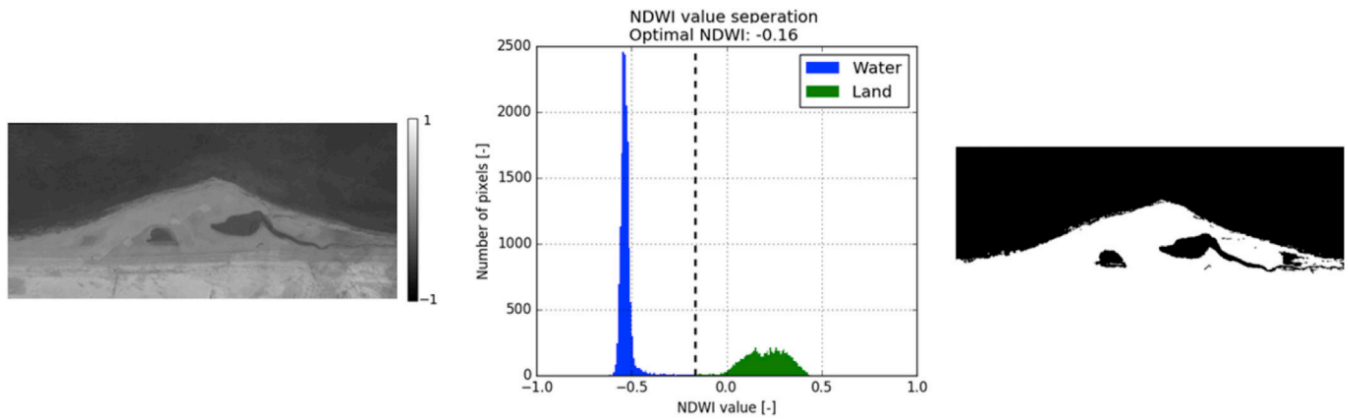
Figure 4. NDWI greyscale image (left), NDWI histogram (middle) and resulting binary image (right) for a Sentinel 2 image acquired on 12-03-2015 10:33:27 (GMT). An optimal threshold value of 0.16 classifies the NDWI values into water (blue) and land (green) pixel. From Hagenaars et al. (2018).

Figure 5 Satellite image acquired by the Sentinel 2 satellite acquired on 12-03-2015 10:33:27 (GMT) for the Sand Motor study site. The derived SDS is plotted in black. From Hagenaars et al. (2018).

To assess the positional accuracy of the SDS, Hagenaars et al. (2018) compared 143 satellite images with high-resolution in-situ measurement data of the Sand Motor mega-scale nourishment located along the South Holland coast in the Netherlands. It was found that the positional accuracy of the SDS (1) depends on the intertidal beach slope and the pixel resolution of the satellite images, (2) has a seaward bias, and (3) is adversely affected by the presence of clouds, waves, sensor corrections and georeferencing errors (Hagenaars et al., 2018). In the same research, Hagenaars et al. (2018) conclude that for ideal conditions, images without clouds and waves, "the accuracy of the SDS is within subpixel precision (smaller than 10-30m, depending on the satellite mission)" and for the highest resolution images they found "an average offset of 1m between the SDS position and the in-situ shoreline in the considered domain." As such ideal conditions are seldom the case, Hagenaars et al. (2018) quantified the effect of drivers of inaccuracy. These so-called drivers of inaccuracy are either related to environmental conditions or the satellite instrument. The SDS accuracy is affected, foremost, by the presence of clouds and to a lesser degree by the presence of waves, corresponding to seaward deviations in the order of 200m to 40m, respectively.

Instead of single satellite images, the use of composite images is an established method to reduce or eliminate the effects of cloud cover, shadows and other disruptions (Gómez et al., 2016). Hagenaars et al. (2018) used image composites to reduce the effects of the abovementioned drivers of inaccuracy. A composite image comprises a number of sequential satellite images within a certain time frame. From an image collection, one creates a composite of each image acquired within a predefined number of days prior and post the acquisition date of that image. E.g., a composite image with a 180-day window comprises all images with their acquisition data 90 days prior and post the acquisition data of the "centre"-image. The use of composite images for shoreline detection provides a sound method for reducing offsets caused by drivers of inaccuracy, such as clouds, waves, soil moisture and sensor corrections. The composite images reduce

the temporal resolution and therefore produce shorelines that only show variations on a semi- to bi-annual scale.

In order to validate the satellite-derived beach width with available beach width in-situ data, it is essential to be aware of what the detected SDS physically represents. As explained in section 2.1, different water levels are used for the seaward demarcation of the beach width, e.g., MLW, MSL and MHW. Whether the SDS is derived from a single satellite image or a composite image is decisive for the type of waterline it represents or corresponds with most. A waterline derived from a single image, arbitrary in time, represents the instantaneous waterline. Ideally, a derived SDS on a given date would be validated with the actual water level retrieved from a historic hydrodynamics database from that same day and time. As such detailed information is usually unavailable, a validation study with in-situ data needs to take into account the difference in acquisition timing of the satellite images versus in-situ measurement. Typically, an offset is expected, which needs to be quantified. Moreover, the use of composite images brings in an additional factor that needs to be considered in the validation assessment. For example, the shorelines derived by Hagenaars et al. (2018) from composite images are validated with an in-situ shoreline constructed to represent the Mean Sea Level.

Recent research has shown that a shoreline can be detected from optical satellite imagery in an automated way and with a promising spatial- and temporal resolution. The accuracy of detected shorelines is dependent on the presence or occurrence of several drivers of inaccuracy: most importantly, cloud conditions. Furthermore, the spatiotemporal resolution is dependent on the choice of using either single or composite satellite images.

2.2.4 Satellite-Derived Vegetation line (SDV)
Since we are looking at beach width detection from optical imagery, we will use the vegetation line as the landward boundary of the beach width. Studies that measure vegetation and use it to analyse coastal (dune) processes and morphodynamics often extract the data from small datasets of aerial photographs or LIDAR (Boak & Turner, 2005; Keijsers et al., 2015; Pollard et al., 2020; Rader et al., 2018; Lalimi et al., 2017). Vegetation lines are already measured from non-satellite optical imagery (often as a measure for the shoreline), but a generic method to automatically derive large numbers of coastal vegetation lines from optical satellite imagery has yet to be presented. In theory, by using a vegetation index (e.g., NDVI) instead of the NDWI, the approach for SDS detection presented by Hagenaars et al. (2018) can be adopted and adjusted for the detection of vegetation lines by taking the border between sandy and vegetated areas. In line with the SDS, we further refer to the vegetation line detected from optical satellite imagery as the Satellite-Derived Vegetation line (SDV).

Part of this study will assess the relationship between the vegetation line and the elevation-based dune foot because of the freely accessible and extensive dataset of the dune foot in the Netherlands. However, measuring elevation data is laborious and expensive and, therefore, infrequent compared to the historical database of multi-temporal satellite imagery.

Correspondence between the seaward limit of dune vegetation (vegetation line) and features discernible from the elevation profile (such as the dune foot or dune toe) is implied by various authors; see, for example, Battiau-queney et al. (2003) and Rader et al. (2018). Wernette et al. (2018) make the notion of the advantage of defining dune features based on the vegetation cover, whereas temporal dynamics of, for instance, vegetation lines can be derived from extensive databases of historical aerial (and satellite) imagery. However, the same researchers also stress that the presence of vegetation cannot always be used to represent dune morphology, considering the seasonal variation of vegetation and location-specific environmental conditions. The research of Keijsers et al. (2015), about the relationship between vegetation cover and sedimentation (involving the seaward vegetation contour and dune foot), also shows there can be a variable offset between the vegetation contour and dune foot depending on locally varying characteristics and development in time,

as depicted in Figure 6 and Figure 7. Figure 6 shows the multi-annual development of the vegetation cover, dune crest and dune foot for one transect located at the beach on the north side of Ameland. Figure 7 shows the vegetation cover and sedimentation rate (m/year) in 2006 for 27 transects at the same beach at Ameland. The figures show that the cross-shore offset between the dune foot and seaward vegetation contour can vary widely within a few kilometres on the same beach or within years along the same transect. For example, at one location, the vegetation contour and dune foot position coincide with each other, and at hundred meters alongshore distance, the vegetation contour and dune foot can be tens of meters apart. Hence, since this research will compare the optically discerned vegetation line with the elevation based Dunefoot, an offset will be expected between these indicators, regardless of the accuracy of the measurement methods.
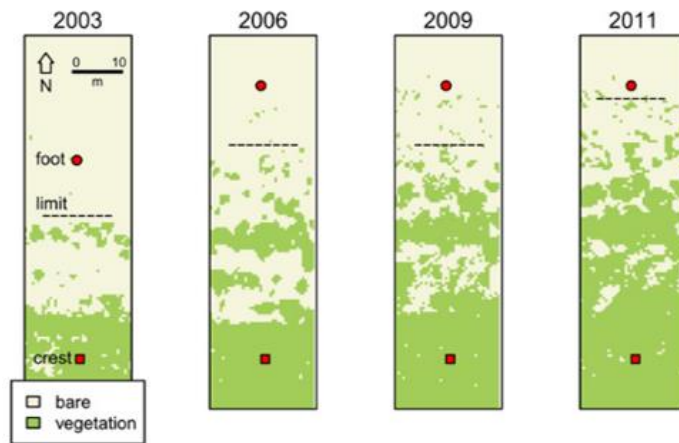
Figure 6 Changes in vegetation cover across a foredune. Development of vegetation cover from 2003 to 2011, profile 9.6 (transect 3000960). Dashed lines indicate the seaward limit of vegetation (at least 5% cover). Adjusted from: "Vegetation and sedimentation on coastal foredunes", by Keijsers et al., 2015.
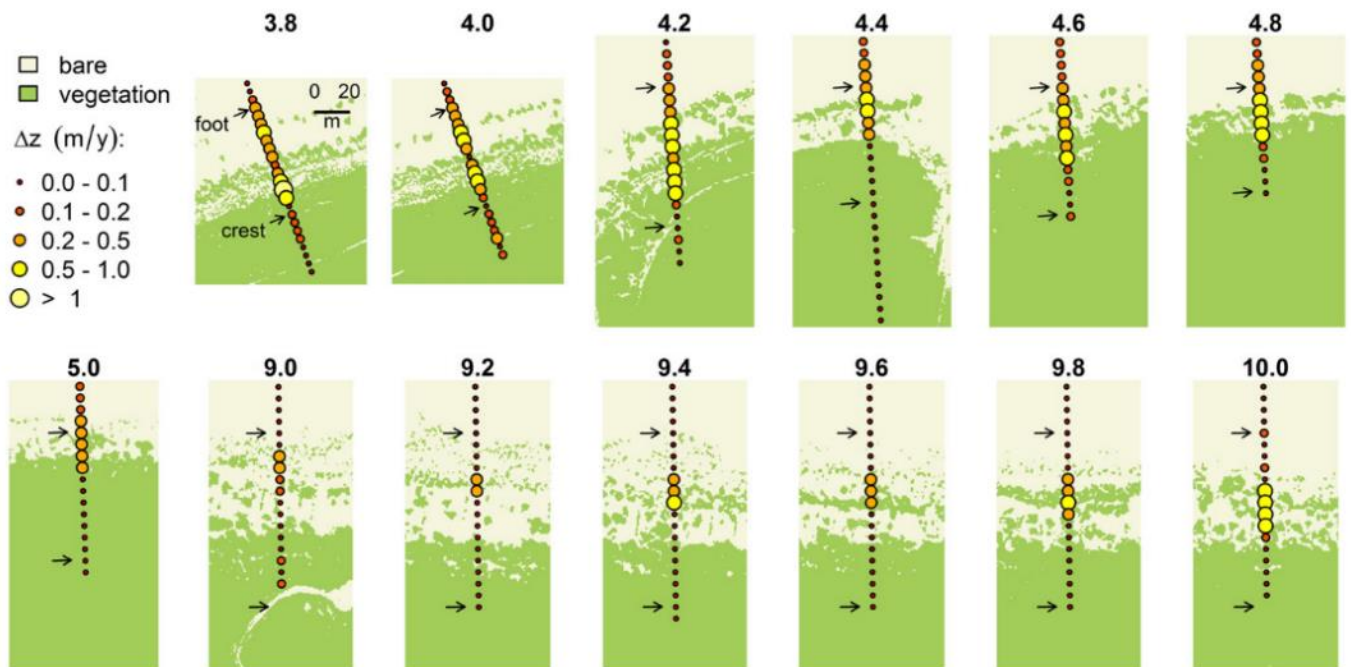
Figure 7. Vegetation map for each profile (transect) with an indication of the amount (of) sedimentation at each measurement point. Arrows indicate the position of the dunefoot and crest. Sea is located at the top of each image. Data from 2006 aerial photo. Adjusted from: "Vegetation and sedimentation on coastal foredunes", by Keijsers et al., 2015.

2.3 Beach width dynamics

This section describes the dynamics one can observe when measuring beach width (and subcomponents) over different scales in space and time. Beach width dynamics depend on the dynamics of the seaward and landward beach boundary and can be related to natural or human-induced causes and factors. Some of these natural causes and factors are, for example, the seasonal variation of the beach profile, interfered longshore-currents, sea-level rise and land subsidence, storm erosion or the landing of sandbanks; human-induced causes or factors can be consequences due to nourishments or the construction of coastal works in the surf zone (Giardino et al., 2014; Stive et al., 2002).

Stive et al. (2002) inventoried both natural and human-induced causes and factors for typical coastal evolution trends according to four different scales:

- Very long term (time scale: centuries to millennia; spatial scale: 100km and more)

- Long term   (time scale: decades to centuries; spatial scale: 10 – 100km)

- Middle term   (time scale: years to decades; spatial scale: 1 – 5 km)

- Short term   (time scale: hours to years; spatial scale: 10m – 1km)

We consider that the dynamics of shorelines, dune foot and vegetation line, and thus the beach width dynamics, can be categorized into the same spatiotemporal scales.

Different underlying causes and factors can influence the beach width variability with varying intensity at different locations since every shore is unique. When measuring beach width dynamics, one essentially measures the sum of the dynamics of the seaward and landward beach width boundaries. Whether the dynamics of the beach width's subcomponents are somewhat similar or deviate entirely from each other determines the signal of the beach width dynamics. In their research, Stive et al. (2002) give an example (see Figure 8) of the temporal and spatial variability of the MLW, MHW and Dunefoot along the Dutch coast (in their research, all three parameters are considered as an indicator for the shoreline's evolution). The timelines in the figure show the evolution of the mentioned parameters for a location (panel a) at the northwest side of the Schiermonnikoog Wadden island and a location (panel b) at the west side of Goeree in Zeeland. We observe different evolutions: a slowly prograding and long-term oscillating trend for Schiermonnikoog and a for a long time retrograding but recently prograding trend for Goeree. The two timelines display that the evolutions of these shoreline indicators fluctuate with different scales in space and time at different locations but also vary between parameters among different locations. For example, at Goeree, the three parameters' evolutions are (almost) synchronized, whereas, at Schiermonnikoog, the three evolutions are not synchronized, especially the evolution of the Dunefoot deviates from the evolutions of the MLW and MHW.
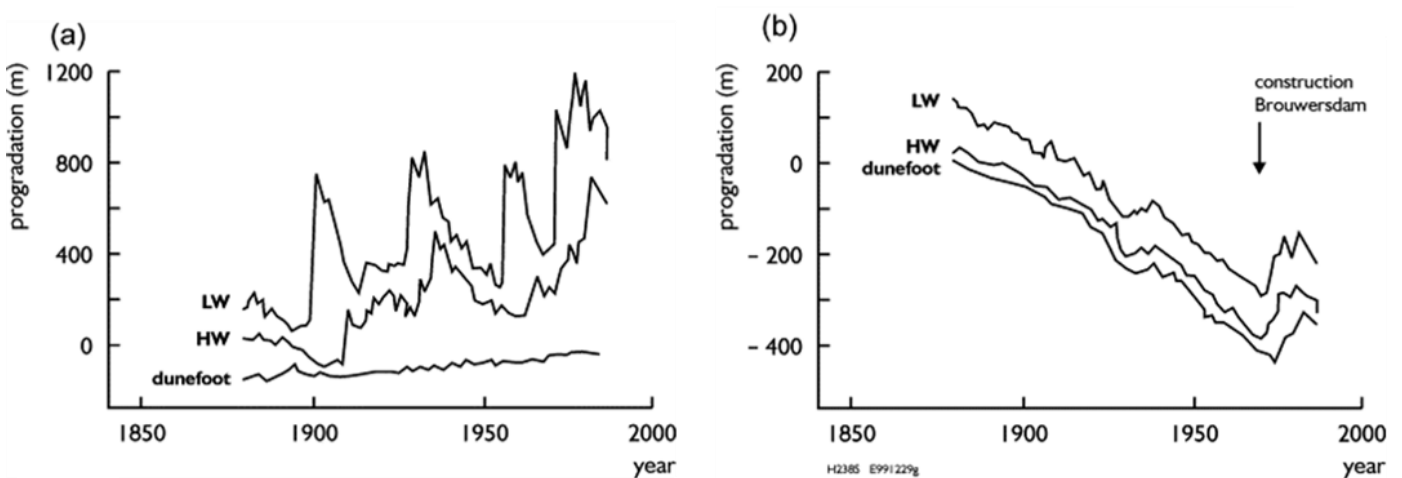

Figure 8. Evolution of the (M)LW, (M)HW (based on tide records) and dunefoot since 1880. (a) Northwest location of Schiermonnikoog. (b) West location of Goeree (The Netherlands). Adjusted from Stive et al. (2002)

The Total Beach Width and Dry Beach Width, as presented in Section 2.1.2, are defined as the distance between the MLW and Dunefoot and MHW and Dunefoot. Looking at the evolutions of the parameters in Figure 8, one can imagine that the beach width's evolutions at those locations show significantly different behaviours. Since the Dunefoot's evolution is relatively static at Schiermonnikoog, the evolution of the Beach Width will be dominated by the (more heavily) prograding and oscillatory evolution of the MLW and MHW. However, at Goeree, the beach width's evolution will show small scale fluctuations but no long-term growth or decay since the Dunefoot evolves at a similar pace and scale as the MLW and (especially) the MHW.

Hence, significant differences are expected for varying locations between the spatiotemporal evolution of the beach width and its subcomponents and the underlying relationship between those parameters. Therefore, these underlying relationships between the parameters representing the seaward and landward beach width boundaries must be evaluated carefully in every case study at different locations.

2.4 Summarising remarks

This chapter presented a brief overview of Beach Width definitions, functions and dynamics and introduced optical satellite imagery and optical feature detection techniques relevant to coastal science. We introduced a proven method for accurately deriving the shoreline from optical satellite imagery, which can analyse (long-term) shoreline dynamics. Using an alternative Normalized Difference Index (the NDVI), we hypothesize that the SDS method (using the NDWI) presented by Hagenaars et al. (2018) can be adjusted to detect the vegetation line from optical satellite imagery. With the SDS and SDV, we can derive a beach width as the cross-shore distance between those parameters, the Satellite-Derived Beach Width (SDBW). We occasionally refer to the SDS, SDV, and SDBW as the Satellite-Derived Parameters (SDPs).
Extensive in-situ coastal datasets are globally scarce. In the Netherlands, the whole coastline is measured annually through the JARKUS measurement survey, containing elevation-based parameters. Coastal evolution varies with spatial and temporal scale, ranging from meters and minutes to kilometres and centuries. Beach width dynamics depend on the dynamics of its seaward and landward boundary.

The next chapter will explain the method for deriving the SDBW and elaborate on the assessment of the SDBW detection and dynamics by comparing the SDBW to the JARKUS measurement data. An essential part of this assessment will be to investigate what the new parameter SDV represents and how it relates to the Dunefoot. Since we do not have extensive high-resolution vegetation cover data, we will not perform a detailed accuracy assessment of the SDV. Since we adapt and augment the SDS detection method of Hagenaars et al. (2018) for detecting the SDV, we initially assume a similar accuracy for the SDV detection in this research.

3 Methods

The previous chapter provided background information on the relevance of (measuring) beach width (dynamics) and existing methods for deriving coastal state indicators from optical satellite imagery. Section 3.1 elaborates on the overall approach we use in this research to derive beach width from optical satellite imagery and analyse changes in time and space. Section 3.2 describes the case study and the available data we use for this research. The computation method for deriving the Satellite-Derived Beach Width (SDBW) from the satellite-derived shoreline (SDS) and vegetation line (SDV) is explained in Section 3.3, together with sensitivities relevant to the computation method. Section 3.5 describes how we will analyse the SDBW derived from composite satellite images and individual satellite images by comparing the SDBW with in-situ measurement data, and Section 3.4 introduces the data we use for those assessments.

3.1 Satellite-Derived Beach Width − Overall approach

The Satellite-Derived Beach Width (SDBW) detection method determines the cross-shore distance between a sandy beach's seaward and landward boundary. This research defines these boundaries as the optically visible waterline and vegetation line (e.g., visually detectable with optical satellites). This research leaves out other possible landward boundaries of the beach, such as the built environment or dike revetments. In short, the SDBW is defined as the cross-shore distance between the positions of the Satellite-Derived Shoreline (SDS) and the Satellite-Derived Vegetation line (SDV) along a predefined transect on a beach (see Figure 9).
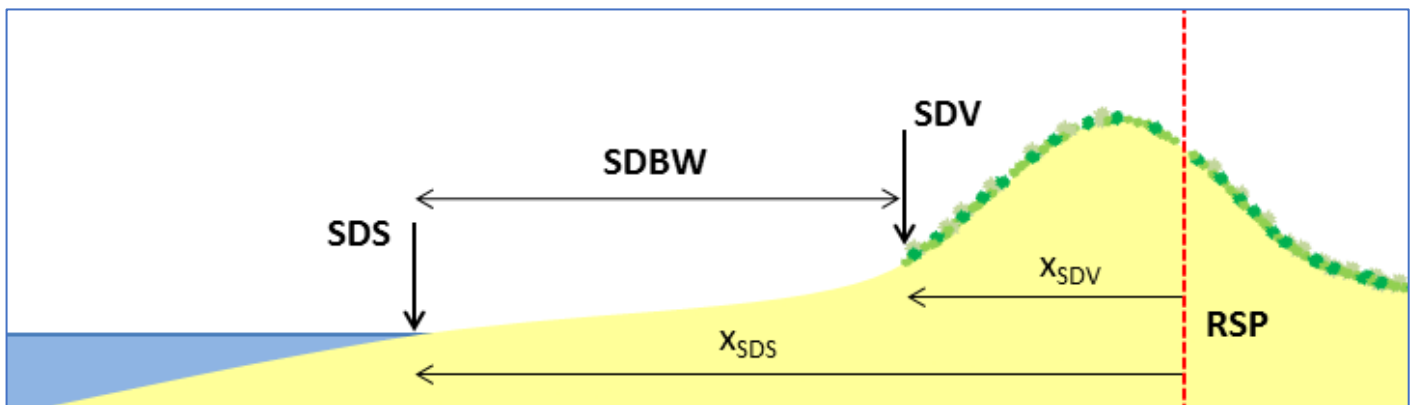
Figure 9 Cross-shore schematic of a sandy beach profile, including the boundaries of the Satellite-Derived Beach Width, the Satellite-Derived Shoreline (SDS) as the seaward boundary of the beach and the Satellite-Derived Vegetation line (SDV) as the landward boundary of the beach. The cross-shore distances of the SDS (X_{SDS}) and SDV (X_{SDV}) are plotted relative to the fixed RijksStrandPalen (RSP) reference line.

To analyse the SDBW and compare it with in-situ measurements, we will study the sandy coast on the northern side of Ameland.

The core principle of the SDBW detection method exists of first computing the SDS and subsequently (but in the same process) computing the SDV. When these indicators are computed, we can derive the SDBW by simply calculating the cross-shore distance between the SDS and SDV along the transect. We determine the positions of the SDS and the SDV along the transect relative to a fixed reference point. In Figure 9, this reference point is represented by the RijksStrandPalen (RSP) (line), which is commonly used in the Netherlands.

There is a difference between coastal features detected from either composite or individual satellite images (as mentioned in Section 2.2). Both have their advantages and disadvantages. We know from Hagenaars et al. (2018) that composite images can be used to detect shorelines and analyse the long-term dynamics of

shorelines. We do not yet know whether this will also hold for the SDV and the SDBW. The measurement data from composite images correspond with the temporal scale of the JARKUS Measurement survey. Individual images can offer an advantage over the JARKUS Measurement survey and composite images because of their significantly higher temporal resolution. Depending on the usability of the individual images, the difference in temporal resolution can be (bi-)weekly for the individual image data versus (semi-)annual for the JARKUS survey and composite image data. We will study the SDBW, and its subcomponents, computed from both types of images and separately compare them with in-situ measurements.

To investigate the quality and potential of the SDBW measurement data, we compare it with the in-situ elevation-based measurement data from JARKUS. Along the JARKUS transects, the MLW, MHW and Dunefoot positional data are provided as a cross-shore distance relative to the intersection of the RSP line with the corresponding transect. We project the SDS and SDV vectors over the same transects. In this way, we can compare the positions of the SDS and SDV with those of the JARKUS parameters. Figure 10 provides a schematic overview of the relevant parameters and how we expect them to relate to each other spatially. We compare the SDS with the MLW and MHW, the SDV with the Dunefoot and the SDBW with the Dry Beach Width and Total Beach width. The analyses and comparisons might show different relationships between the parameters, as displayed in Figure 10. We know that these parameters are not equal to each other. However, we expect that analysis of the differences and similarities will provide insight into the validity of the SDBW detection method and the detection of its components.
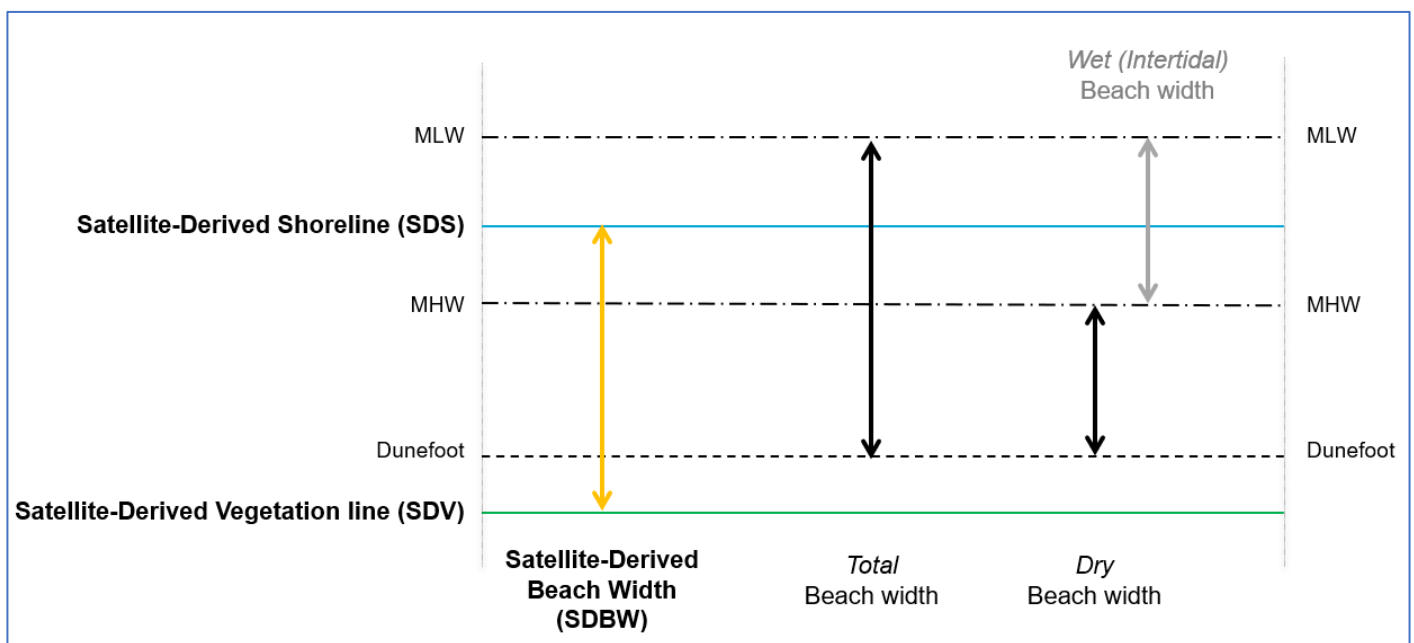
Figure 10 Schematic overview of the indicators of the SDBW and JARKUS beach widths with positions relative to each other

The flow chart in Figure 11 gives an overview of the different steps in the study on the Satellite-Derived Beach Width. It includes a description of the SDBW detection method and the sensitivities we encounter in the process (described in Section 3.3) together with the comparison of the SDBW data with in-situ JARKUS data (introduced in Section 3.4 and Section 3.5) leading to the results in Chapter 4.
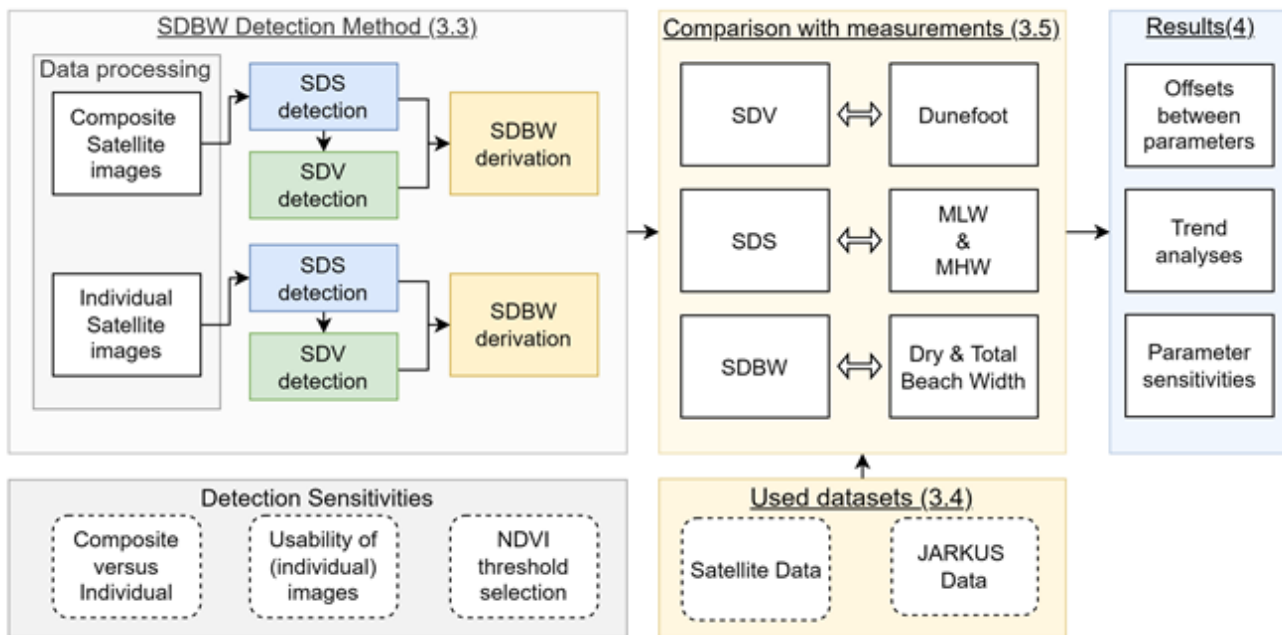
Figure 11. Flow chart of the overall approach of the method to be executed for the research on the Satellite-Derived Beach Width.

3.2 Case study: Ameland

This section introduces the Ameland case study; we describe the island characteristics, the local morphology, and the available data. For studying the SDBW following the aforementioned conditions, any sandy beach in the Netherlands with a natural landward boundary would do. In this research, the island of Ameland was chosen for the case study because it offers two advantages compared to other sandy shores in the Netherlands. The first is the dynamic nature of the northern coast of Ameland, so we expect to be able to see the consequences of past events translated to dynamics in the SDBW. The second is the availability of data on vegetation cover in the dunes originating from Keijsers et al. (2015), which might say something about the relation between vegetation cover, elevation, and the satellite-derived vegetation line.

3.2.1 Island description and morphology

The barrier island Ameland is one of the Dutch Wadden Islands, which separate the North Sea from the Wadden Sea. Figure 12 displays the island and its location within the Wadden Sea. The island is approximately 24 kilometres long and has a maximum width of 4.5 kilometres. The island's northern side, including the eastern and western island heads, exists of a sandy beach-dune system. Dikes and revetments protect the southern side of the island. Due to local gullies, the Borndiep on the West and the Pinkegat on the East, the two island heads are subject to different morphological processes. In order to counter erosion on the western island head, several coastal defence structures have been placed, and nourishments are regularly carried out. The latter contrasts with the eastern head, where natural dynamics occur without human interventions (Mastbergen et al., 2018). Between 1980 and 1985, the offshore sandbank "Bornrif" landed on the western side of the beach, which has been spreading out and migrating in an eastward direction since then (Mastbergen et al., 2018). Due to this ongoing migration, the northern beach sees a trend of sedimentation east of the landed sandbank. Nevertheless, nourishments are applied regularly on the whole northern coast of Ameland. The development of the Ameland morphology between 1965 and 2016 is displayed in Figure 13. The landing and spreading of the Bornrif sandbank are well depicted in the figure.
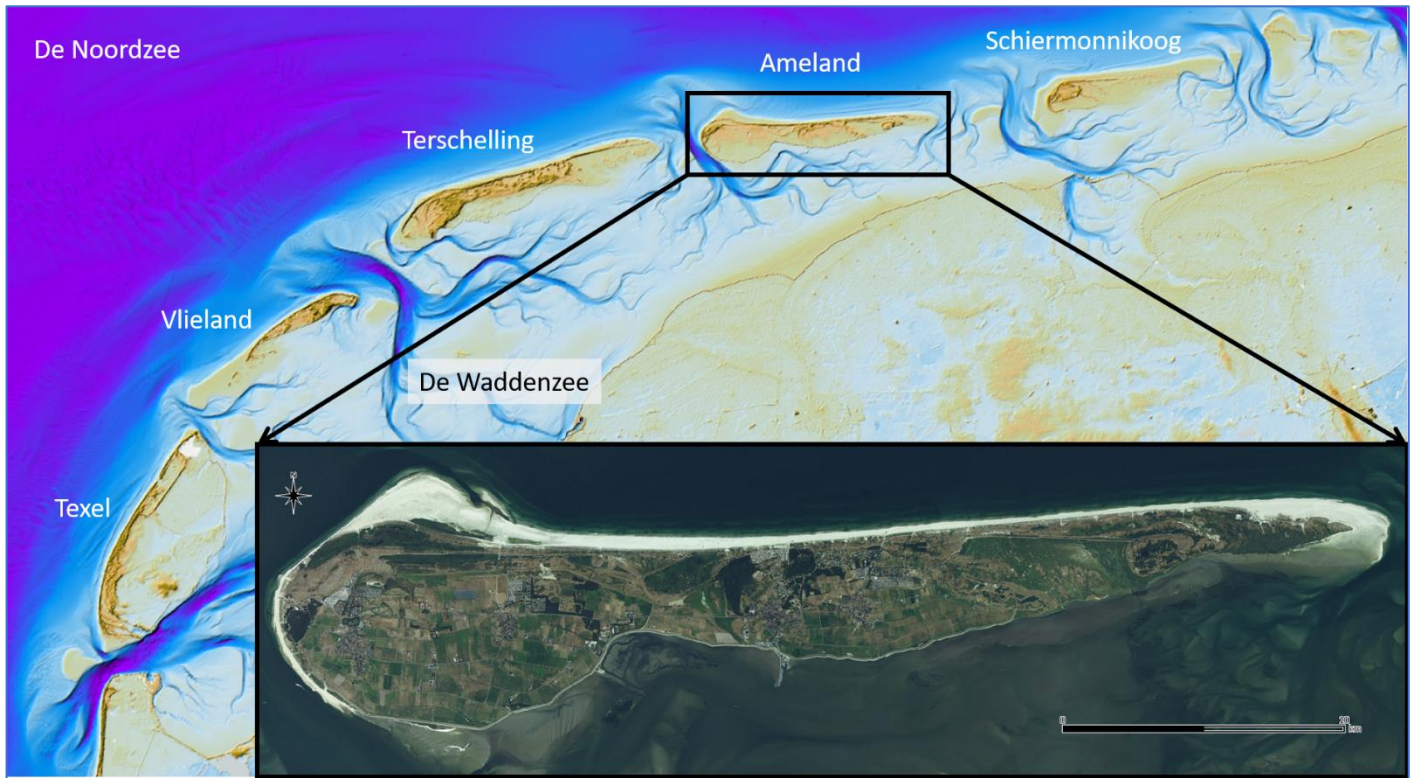
Figure 12 Wadden Sea overview (OpenEarth – Coastviewer - Vaklodingen, https://www.openearth.nl/coastviewer-static/#/). Zoom-in Ameland (TripleSat image, 80cm pixel resolution, August 2018, https://www.satellietdataportaal.nl/).
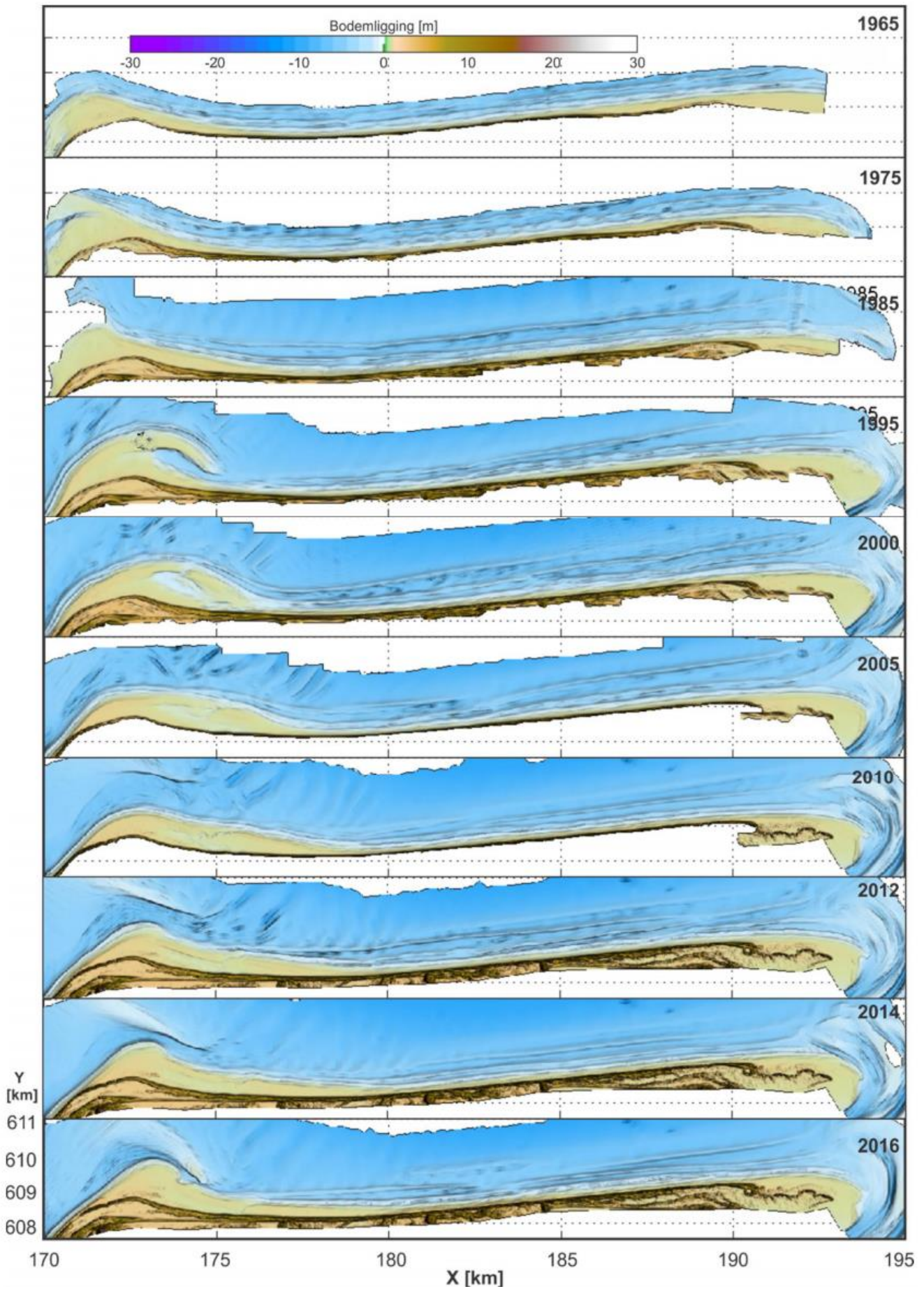
Figure 13. Top view of the morphology of the (northern) island coast of Ameland based on gridded JARKUS data representative of the period 1965-2016. Reprinted from "Beheerbibliotheek Ameland", by Mastbergen et al., 2018, p30.

3.2.2 Data availability

In order to assess the quality and potential of earth observation data to assess beach widths, we compare in-situ measurement data from the annual coastal survey by Rijkswaterstaat (RWS), also known as JARKUS, with earth-observation data of coastal features derived from satellite imagery from NASA and ESA. We use these data collections since they are free of cost and contain extensive data for the whole coast of the Netherlands.

Beach profile data

We use the JARKUS data (which contains annual measurement data from 1965 to 2021) to compare with the positional data of the SDS, SDV and SDBW. The measurements are a combination of bathymetry measurements for the underwater part of the coast and LiDAR (aerial) elevation measurements for the above-water part of the coast. The data is transposed as elevation profiles on a system of cross-shore transects perpendicular to the coast, the JARKUS transects. These transects are oriented towards the national RijksStrandPalen (RSP) line, which serves as the transect's zero point. The transects have a 5-meter resolution and are alongshore-spaced every 200 to 250 meters along the Dutch Coast. On average, the survey measurements are done post-storm season, in late winter or early spring. The dataset contains positional data of the MLW, MHW and Dunefoot on each transect. The JARKUS dataset provides beach widths derived from the distances between those features; the Wet Beach Width or Intertidal Area (MLW-MHW), the Dry Beach Width (MHW - Dunefoot) and the Total Beach Width (MLW – Dunefoot).

The analyses of this case study focus on the reach between transects 3000300 and 3002100, shown in Figure 14. The selected reach is 18 kilometres long and comprises 91 transects, 200 meters apart from each other. This study site was selected for different reasons, but mainly because we expect to see the effects of the landing of the Bornrif sandbank and multiple nourishments in the beach width dynamics. Also, we select these specific transects for ease of programming and data visuality; to have a straight line from West to East. Therefore, the study site does not include all transects along the Ameland coast. We exclude the transects at the island heads. These are transects 3000100 to 3000280 and 3004600 to 3004966 at the western head and transects 3002100 to 3002516 at the eastern head. Also, we exclude the "corner" transects 3000301 to -304 and 3000401 to -404 to have equal distances between transects. From here on, since we only look at Ameland in this study, we refer to the transects with their site-specific numbers, without the administrative numbers referring to the coastal zone ("Kustvak"). For example, we will refer to transect 720 instead of transect 3000720, and so on.

Figure 14 Ameland study site, with the RSP line in red. The JARKUS transects (in blue) are labelled every 2 kilometres. Sentinel-2 image (July 2018)

Satellite data

In this research, we use the optical satellite imagery of the Landsat 5, Landsat 8, and Sentinel 2 missions to detect the SDS, SDV and SDBW. Table 1 gives information about the temporal extent, the pixel resolution and revisit time corresponding to the used satellite missions. The sizeable temporal extent of the combination of Landsat 5 and Landsat 8 data allows looking at (relatively) large-scale trends of coastal state indicators. Whereas the high pixel resolution and short revisit time of the Sentinel-2 data enable research of more detailed intra-annual dynamics.

Table 1 Overview of used satellite missions, data extent and spatial and temporal resolution.

Satellite mission	Temporal extent	Pixel resolution [m]	Revisit time [days]
Landsat 5	01/1984 – 10/2011	30 x 30	16
Landsat 8	> 04/2013	30 x 30	16
Sentinel 2	> 07/2015	10 x 10	5

3.3 Method for deriving the Satellite-Derived Beach Width

This section describes the method to derive the Satellite-Derived Beach Width. We define the Satellite-Derived Beach width as the cross-shore distance between the SDS and the SDV. The basic principle of this method is to extract the SDS and SDV vectors from satellite images using two normalised difference indices (see Section 2.2.2). First, we use the NDWI index to derive the SDS vector, and subsequently, we use the NDVI index to derive the SDV vector. The method is an augmentation of the SDS detection method by Hagenaars et al. (2018) (see Section 2.2.3). Figure 15 presents the main steps of the detection method through a flow chart. Section 3.3.1 describes the steps (depicted in Figure 15) for detecting the SDS and SDV and the sensitivities we pay extra attention to during the different processes. Finally, Section 3.3.2 describes how we derive the SDBW from the SDS and SDV vectors.
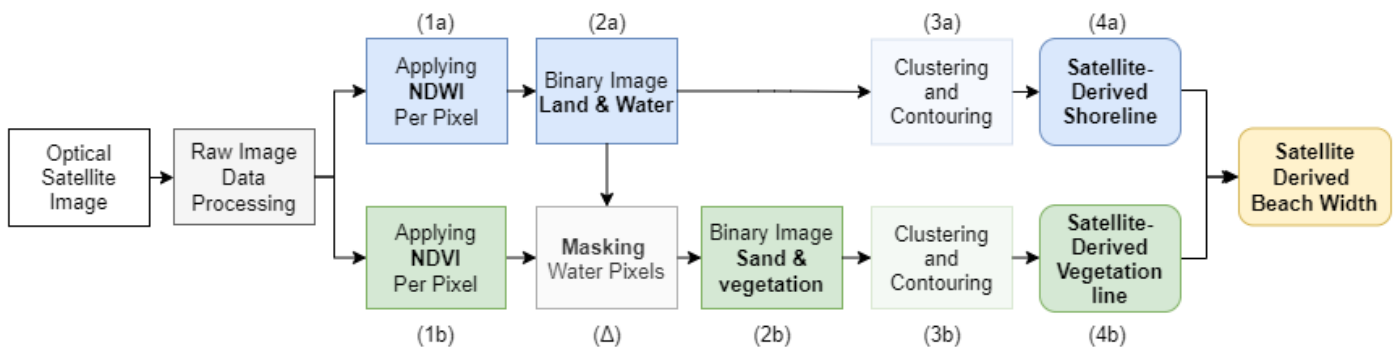
Figure 15 Flow chart displaying the sequence of the main steps for deriving the Satellite Derived Beach Width. Adaptation from Hagenaars et al. (2018).

3.3.1 SDS and SDV Detection

To derive the SDS and SDV from one satellite image, the raw image data is first prepared on the GEE servers with several pre-processing steps. For more information on these pre-processing steps, see the studies of Hagenaars et al. (2018) and Kuleli et al. (2011). Next, the script calculates the NDWI and NDVI indices for every pixel of the pre-processed satellite image (steps 1a and 1b). With this step, we initiate two separate loops. We begin with the loop for determining the seaward boundary vector or Satellite-Derived Shoreline. First, we determine an optimal threshold value (with Otsu's method), which separates the two dominant pixel masses of the NDWI pixel distribution (left panel of Figure 16) into two parts: one representing "water" (blue) and the other representing "land" (green). This pixel partition enables creating a binary image by assigning the image pixels as either land or water (step 2a), of which an example is depicted in the right panel of Figure 4. The land and water pixels are clustered into two groups (step 3a). The SDS vector is then formed by contouring the binary image's land-water border (step 3a/4a).

The second loop is the detection of the Satellite-Derived Vegetation line. We compute the SDV similarly to the SDS from the *water-masked* image. First, to obtain the water-masked image, we mask (exclude) the "water" pixels from the NDVI processed image (step Δ). Next, we divide the NDVI values of the remaining "land" pixels of the image (right panel of Figure 16) with another threshold value; a supervised value. The difference between supervised and automated threshold values is explained in the following paragraph and Appendix A. The threshold separates the NDVI pixel distribution into "sand" pixels (yellow) and "vegetation" pixels (green). Next, we create another binary image from the sand and vegetation pixels (step 2b). The SDV

vector is then formed similarly to the SDS vector: by clustering the sand and vegetation pixels into two groups, of which the contour between the two groups resembles the SDV. Figure 17 presents an example of an SDS vector and an SDV vector computed for the Northern coast of Ameland.
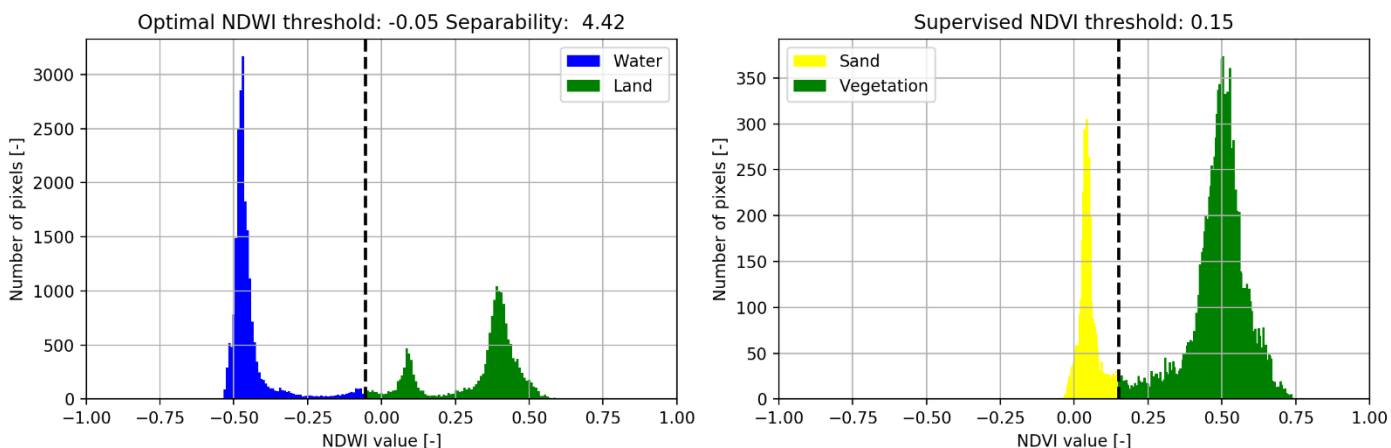
Figure 16 Example of NDWI and NDVI histograms derived from the pixels of a Sentinel-2 image (2016-09-15) within the confines of a selected area of interest of the northern coast of Ameland. The NDWI histogram on the left shows the partition of all image pixels into pixels corresponding to either water or land. This partition is done with an optimal threshold value automatically derived with Otsu's method. The separability value gives an indication of the ease of separating the pixel masses with Otsu's method. The NDVI histogram on the right shows the partition of the remaining land pixels into pixels corresponding to either vegetated or non-vegetated (sandy) areas. The masses are divided with a supervised threshold value of 0.15. Pay attention: the vertical axes of the histograms have different scales.
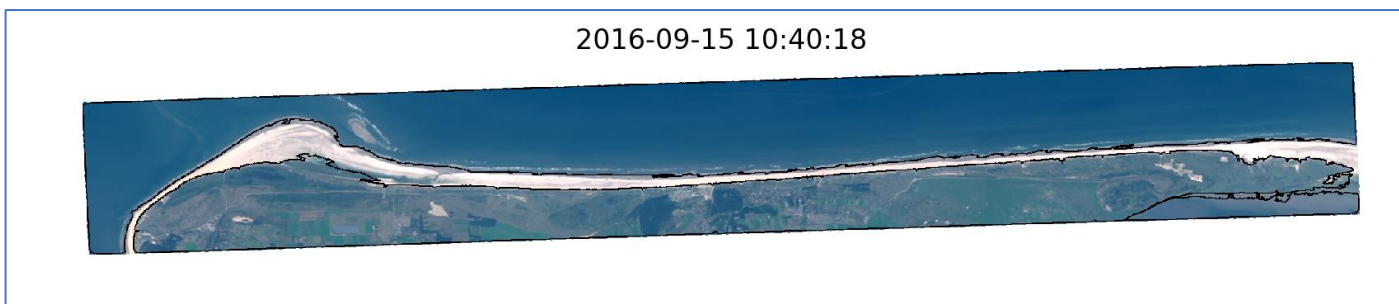
Figure 17 This figure shows the SDS and SDV vectors, plotted as black lines, derived from a Sentinel-2 image (2016-09-15) of the northern coast of Ameland. The computation of the SDS and SDV vector is based on the partition of the pixel distribution in the NDWI and NDVI histograms shown in Figure 16.

NDVI Threshold selection

We need a particular threshold value to separate the NDWI and NDVI pixel distributions for the SDS and SDV detection (see Section 2.2). We use Otsu's method to automatically derive an optimal threshold value to separate the NDWI pixels for shoreline detection. However, for detecting the vegetation line, we found that Otsu's method does not work very well for deriving an optimal threshold value for the NDVI pixels. The index values of the image pixels processed with the NDWI and NDVI show that the difference between sand and vegetation is less distinct than the difference between land and water (see Figure 16). Otsu's (automated) method requires two easily distinguishable pixel masses to determine the optimal threshold value, possibly explaining the difficulties the algorithm encounters in determining a suitable threshold value for SDV detection. Therefore, we assessed whether a supervised threshold value might perform better to detect a representative SDV than when using an automatically selected threshold value (i.e., derived with Otsu's method). Also, we did a sensitivity analysis to assess the most suitable supervised threshold value. Both assessments can be found in Appendix A.

Based on the results from those assessments, we conclude that a supervised threshold value is best for separating the pixel masses in an NDVI histogram (of a satellite image of a typical Dutch beach-dune system). The first assessment showed that, based on visual analyses, the SDVs with supervised threshold selection

represent the actual (most-seaward) vegetation line best. The SDV with automated threshold selection is located, on average, 40 to 50 meters landward from the SDV derived with the supervised threshold value and, hence, has a less realistic representation of the actual vegetation line. Figure 18 shows two SDV vectors detected from the same satellite image with the two different threshold selection methods; the yellow line presents an SDV vector detected with an automatically derived threshold value, and the red line presents an SDV vector detected with a supervised threshold value. The green line presents the JARKUS Dunefoot position for reference.
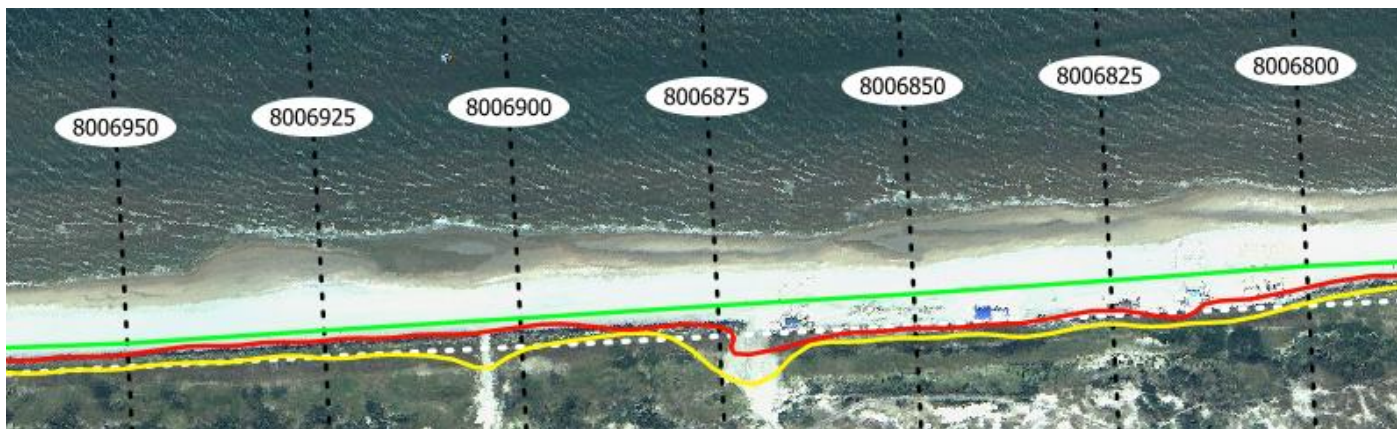
Figure 18 This figure displays two SDV vectors derived from a Landsat 8 image (May 2018) with different threshold selection methods, to give an example of the positional difference in threshold selection: the red line is a SDV derived with a supervised threshold value and the yellow line is a SDV detected with an automated threshold value. The green line is the Dunefoot position from the 2018 JARKUS survey. The black and white striped lines are the transects and RSP line respectively.

Although it varies per image, we conclude from the second assessment in Appendix A that, on average, a supervised threshold value of 0.15 is most suited for detecting the vegetation line for the Ameland case study (and likely for similar beaches in the Netherlands). Hence, in the remainder of this report, all SDVs are detected with a supervised threshold value of 0.15.

Following the sensitivity analyses in Appendix A, we conducted a supplementary study to investigate further which type of NDVI threshold selection resulted in detecting the most accurate (or realistic) SDV vectors. This study, found in Appendix B, involved a comparison of vegetation cover data from Keijsers et al. (2015) with the SDV's derived with either automated or supervised NDVI threshold value. This analysis strengthens the preferred choice for a supervised threshold value.

Composite images versus individual images
We will analyse the SDS and SDV detected from composite satellite images and individual satellite images. We know from previous studies that an SDS detected from an individual image represents a different shoreline than an SDS detected from a composite image. We also expect differences for the SDV, and we will study what those differences are.

A composite image shows the position of a coastal feature averaged over several images in a predefined timeframe, as was explained in-depth in Section 2.2. The research of Hagenaars et al. (2018) showed that with SDS derived from composite images, we can accurately detect large-scale structural shoreline trends. Based on their results, we decided to use composite images composed of images with less than 60% cloud cover within a 180-day window (Section 3.4.1). The number of images within a window varies for each composite because of the variable quality of the images (e.g., due to clouds, sensor distortions) and different time intervals of the Landsat 5 & 8 missions.
Composite images reduce the temporal resolution of the measurement method and are, therefore, less suited for studying short-term coastal dynamics. Hence, we also look at individual images (Section 3.4.2). Individual

images show (the situation of) a selected area of interest in one instant of time (e.g., the acquisition date of the satellite image). A return period of 5 to 16 days of the satellite image acquisition provides a higher resolution in time for a collection of individual images than a collection of composite images. In theory, with a collection of (high quality and cloud-free) individual images, it should be possible to analyse the dynamics of coastal features on a smaller timescale.

Image quality and usability
When using individual images, clouds, cloud shadows and other drivers of inaccuracy are not (partly) mitigated, as is the case with composite images. The usability of satellite images is hampered mainly by the presence of clouds and cloud shadows. The meta-data of a satellite image includes cloud cover percentage. This percentage describes the cloud cover of the whole satellite image in question. It occasionally happens that the given value for the whole image does not correspond to the cloud cover above the studied area of interest. For example, an image may have a low cloud cover percentage, but the small number of present clouds happen to be located precisely above the area of interest. Alternatively, an image may have a relatively high cloud cover percentage, but the area of interest is entirely free of clouds and cloud shadows since the area of interest is often only a small section of the complete satellite image. Therefore, when selecting a maximum percentage for the cloud cover metadata to filter the satellite images, a satellite image may be wrongfully omitted from the simulation.

To ensure we include all individual images in the spatial analysis with a visible area of interest, all satellite images covering our area of interest (and captured within the assigned time window) are included in the simulations and are screened afterwards for their usability. We use two mathematical algorithms (based on a similarity principle) to screen and qualify the individual images on their usability. Appendix C elaborates on these algorithms. By manually selecting a "perfect" image, free of clouds, cloud shadows or technical image corruptions, and mathematically comparing that image with all other images in a dataset, we filter out the unusable images from the dataset. Furthermore, we will analyse whether the number of usable images varies throughout the year. In the Netherlands, there are on average more cloudy days in fall and winter than in spring and summer. Thus, we expect that there will be more usable images available in spring and summer. Drivers of inaccuracy related to the satellite instrument or other factors can also influence the quality of satellite images, as was explained in Section 2.2. These drivers of inaccuracy are more often present with Landsat 5 and Landsat 8 images than with Sentinel-2 images. In our analysis of individual images, we will look at the Sentinel-2 images. Therefore, these other drivers of inaccuracy are almost entirely non-occurring in the analysis.

3.3.2 SDBW Derivation
To derive the beach width from the satellite-derived shoreline and satellite-derived vegetation line, we calculate the distance between the SDS and SDV vectors. For any location or case study to be analysed by the SDBW detection method, cross-shore transects of fixed length are defined perpendicular to the coastline. These transects will preferably be defined equidistant in alongshore direction and have a fixed reference point. For the Dutch Coast (e.g., the Ameland Case-Study), the earlier introduced system of JARKUS transects is well suited for this approach. The RSP line functions as the fixed reference line or per transect as the fixed reference point or zero point. We use the intersections of the SDS and SDV vectors with the transects as the measurement data for these parameters; an example is displayed in Figure 19. The SDS vector in blue and the SDV vector in green are plotted along the transects (black-dashed) with the RSP line as the reference line (white striped). Calculating the difference between the distances of these intersections relative to the reference line (the zero point) enables the computation (Eq. 3) of the Satellite-Derived Beach Width per transect, displayed in Figure 9.

$$SDBW = X_{SDS} - X_{SDV} \qquad \textit{Eq. 3}$$
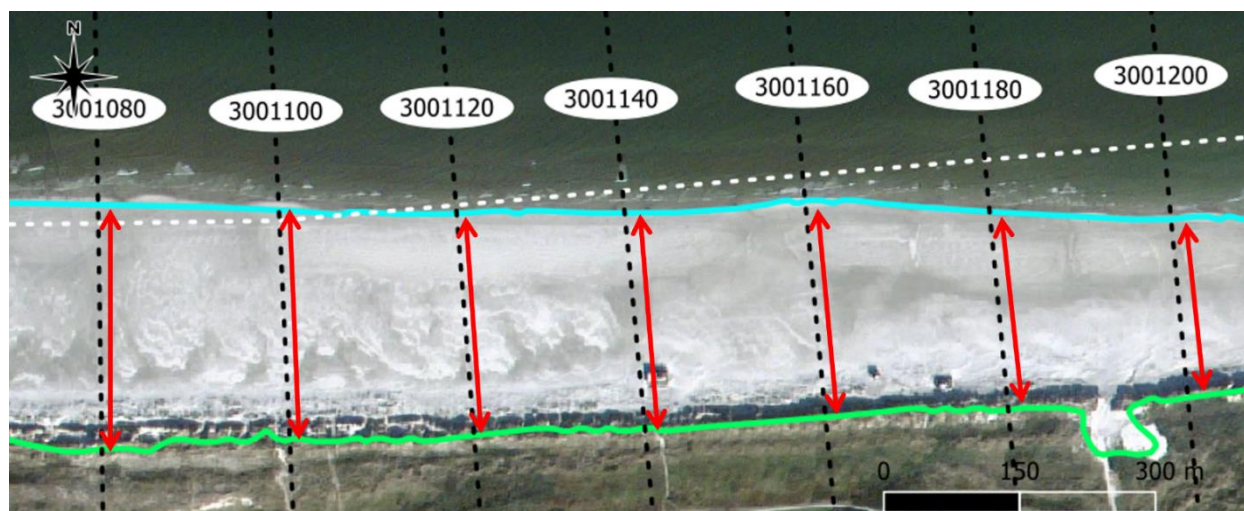
Figure 19 SDS and SDV vectors derived from a Sentinel-2 image (October 2018) plotted over transects 3001080 to 3001200 at Ameland; SDS in blue, SDV in green. The black and white striped lines are the transects and RSP line respectively. The red arrows represent the SDBW derived as the cross-shore distance between the intersections of the SDS and SDV vectors along each transect. (TripleSat image, 80cm pixel resolution, October 2018, acquired from www.satellietdataportaal.nl)

3.3.3 Summarising remarks

This section explained the method for computing the SDBW and its subcomponents and introduced the key aspects and parameters. In the following two sections, we describe the data we are going to use (Section 3.4) for the assessments (Section 3.5) we will carry out in Chapter 4 on the position and dynamics of the measured SDBW.

3.4 Data used in the assessment of the SDBW and comparison with JARKUS

This section describes the datasets used to analyse the SDBW derived from Composite satellite images (Section 3.4.1) and Individual satellite images (Section 3.4.2). As far as possible, a comparison will be made between the outcomes of the two different analyses. It should be taken into account that this will not be a direct comparison, as the datasets differ in the considered study period, satellite type (e.g., different pixel resolution and return period) and image technique. Nevertheless, we expect the comparison to provide some insight into the differences and similarities of the performance of the SDBW detection from either dataset.

3.4.1 Description of the composite image dataset

The analyses of the composite data are based on measurements from 477 Landsat composite images acquired between November 1984 and November 2018. This set of composites consists of 366 Landsat 5 images (1984-2013) and 111 Landsat 8 images (2013-2018). We use the measurement data of 33 JARKUS surveys between 1984 and 2018.

With 477 satellite images in the selected period and 91 transects on the reach, the dataset would potentially consist of a total of 43407 data points. However, due to various drivers of inaccuracy, it sometimes occurs that the SDV and SDS are not, or wrongly, detected for parts of the image or the complete image, see Figure 20. Hence, for some of the images, there are no intersections of the SDV or SDS vector along certain transects. When this was the case, these points were excluded from the dataset. Furthermore, to exclude any remaining unrealistic SDV or SDS positions, datapoints that are located further than three standard deviations from the transect's temporal mean SDS or SDV positions are also excluded.
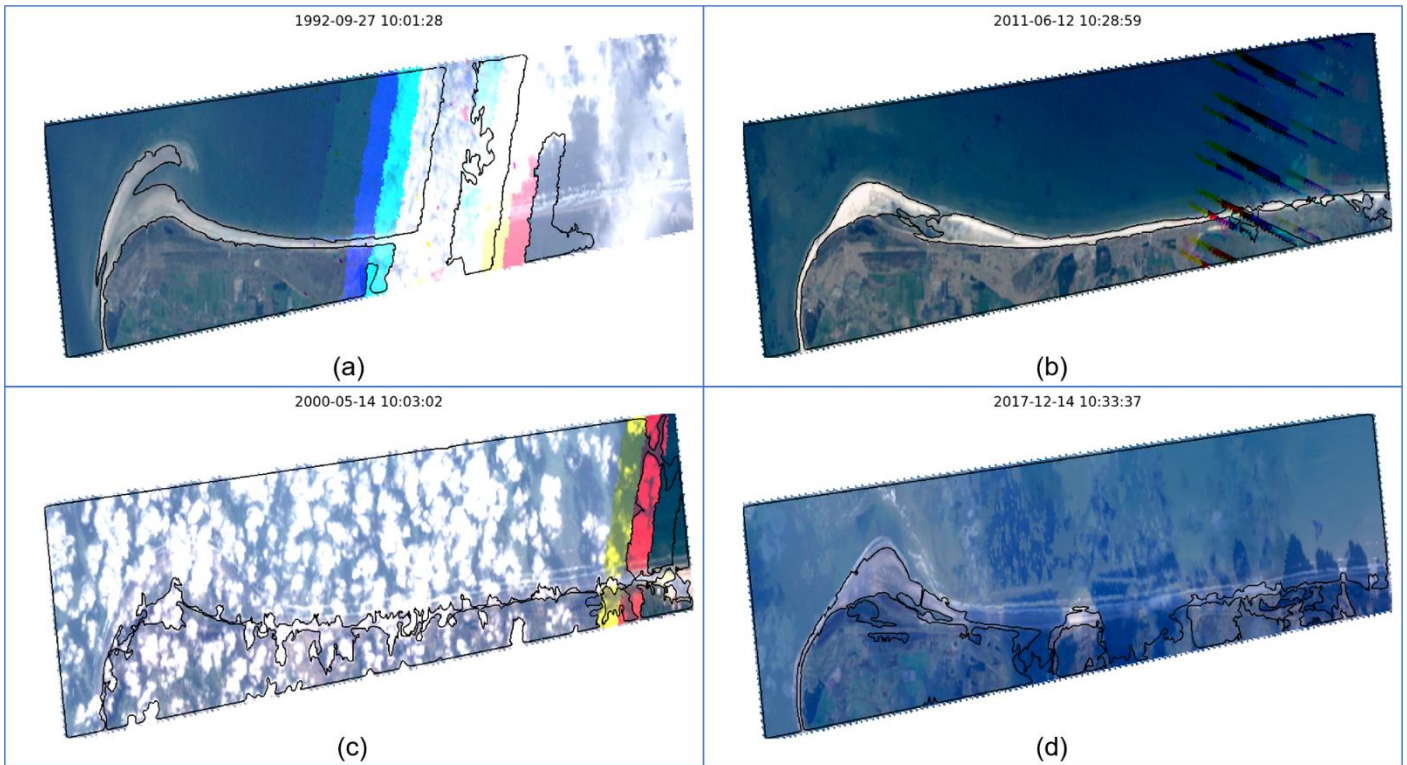
Figure 20. Four types of inaccuracy drivers found on composite satellite images (180-day composites of Landsat 5 and 8 images, with max 60% Cloud cover). (a) & (b) Satellite instrument errors caused by issues which originate at the overlap of adjacent satellite swaths. Clouds (c) and Cloud shadows (d) above the area of interest, without being filtered out by the composite of the images.

3.4.2 Description of the individual image dataset

The analyses of individual image data are based on measurements from Sentinel-2 images between 2015-07-01 and 2019-04-11 and JARKUS surveys between 2015 and 2018. When simulating the results (May 2019), there was no measurement data of the 2019 JARKUS survey (and later). There are 376 Sentinel-2 images available within the selected period. The usability of those images is often reduced by clouds or cloud shadows since we do not use the composite technique to even those errors out. Other drivers of inaccuracy do not occur or occur significantly less frequent for Sentinel-2 images than for Landsat images (such as swath-related issues).

Before analysis, we use two image-processing algorithms to assess the usability of the Sentinel images based on the principle of image similarity. The methodology of the image quality assessment is further elaborated in Appendix C. From the assessment, we found 89 out of 376 images to be suited for analysis within the selected period. Figure 21 shows a timeline with available and usable Sentinel-2 images between 2015-07-01 and 2019-04-11, the JARKUS survey dates and launch dates of Sentinel-2A and Sentinel-2B. The number of available images significantly increased after the launch of Sentinel-2B on the 7th of March 2017. Table 2 categorizes the Sentinel-2 images according to the seasons in which they were acquired. We note significantly more usable images in spring and summer than in autumn and winter, and we assume that this is related to the weather conditions in the Netherlands.
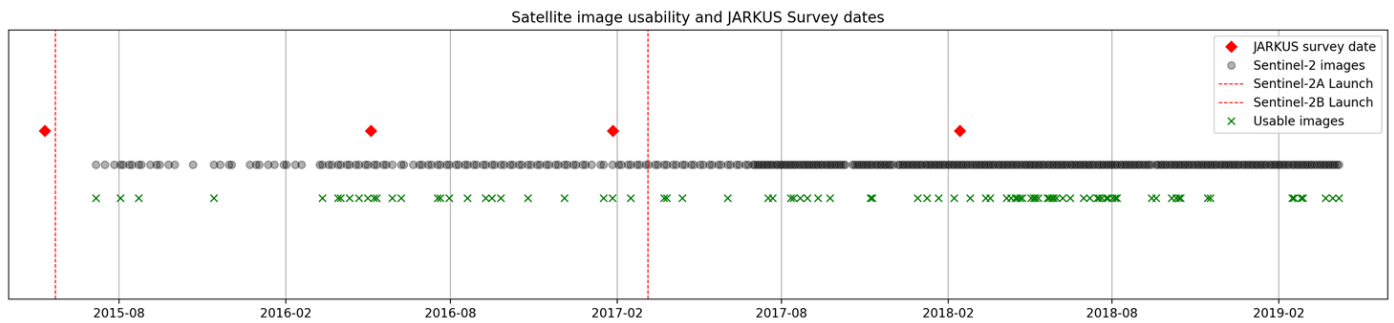
Figure 21 The black circles in this timeline represent all the Sentinel-2 images that have been acquired since the launch of the Sentinel-2A satellite in July 2015 up to 04-11-2019. The green crosses display the images from that collection which have been qualified as usable trough post-processing algorithms. The JARKUS survey dates are depicted as the red diamonds.

Table 2 Inventory of image usability for all Sentinel-2 images extracted between 2015-07-01 and 2019-04-11. The image usability is assessed for an Area of Interest covering the island of Ameland.

	Total	Spring	Summer	Autumn	Winter
All images	376	80	102	94	100
Usable images	89	33	28	13	15
Percentage	24%	41%	28%	14%	15%

3.5 Methods to analyse the Satellite-Derived Beach Width and compare with JARKUS data

This section describes the methodology for analysing the SDS, SDV, and SDBW derived from composite and individual satellite images and comparing them with the in-situ measurement data of JARKUS: the MLW, MHW, Dunefoot, Total Beach Width (MLW - Dunefoot) and Dry Beach Width (MHW - Dunefoot). First, Section 3.5.1 describes how we determine the offsets between the SDV and Dunefoot and the SDS and MLW and MHW and the differences in size between the SDBW and JARKUS beach widths. Next, in Section 3.5.2, we elaborate on the dynamics of the measured parameters in both datasets.

3.5.1 Analysing the offsets and differences between the (subcomponents of the) SDBW and JARKUS beach widths

We determine one SDV and one SDS position per transect from the SDS and SDV vectors derived from each satellite image. We select the most seaward SDV intersection with a transect as the SDV position to compare with the Dunefoot and the most landward SDS intersection (the one closest to the RSP line) as the SDS position to compare with MLW and MHW. Occasionally a satellite image has an SDV/SDS vector that intersects more than once with a transect. The latter occurs when the SDV or SDS vectors have detected an actual multitude of geographic features crossing that transect or when the images are hampered by clouds, cloud shadows or erroneous image data (see Figure 20). The distance between the SDV and SDS positions gives the SDBW, which we compare with the Total and Dry Beach Widths from JARKUS. The offsets between the subcomponents of the beach widths assist in interpreting the differences and similarities between the said beach widths.

We compare the feature data of all the satellite images with the JARKUS data of the survey that is closest in time to the acquisition date of each specific satellite image. Per transect, we derive the temporal means and standard deviations of the offsets between the SDV and Dunefoot and between the SDS and MLW and MHW.

In the analysis of the individual satellite images, we do an extra analysis in which we compare the (instantaneous) SDS positions with the MLW and MHW data of the JARKUS dataset. The positional spreading of the SDS detected from cloud-free individual images is controlled mainly by the tidal variation and, to a lesser extent, wave run-up and foam due to breaking waves. In theory, the SDS should be in the intertidal area. The distance between the MLW and MHW lines is defined as the wet beach width and gives a rough

estimation of the size of the intertidal area. Hence, we expect that the majority of SDS is located between MLW and MHW.

We derive the SDS from images acquired in a window spanning 180 days before and after the JARKUS survey dates of 2016, 2017 and 2018. Table 3 shows the number of available images in the 180 days before and after the JARKUS measurement dates. Due to the varying dates of the surveys throughout the year, some images may be in two image collections. Note: the 180 days window is unrelated to composite images. We exclude the JARKUS surveys of 2015 and 2019 from this analysis. Regarding the 2015 survey, there are not enough images available within the range of ±180 days around the survey date to derive sensible statistics.

Table 3 Inventory of available Sentinel-2 images 180 days before and after each JARKUS survey, from 2016 to 2018.

Image collection	Survey date T_{Jarkus}	Sentinel-2 images -180 days	+180 days	Total
2016	2016-05-05	7	12	19
2017	2017-01-27	8	7	15
2018	2018-02-14	10	30	40

3.5.2 Assessing and comparing the dynamics of the (subcomponents of the) SDBW and JARKUS beach widths

For this analysis, we will compare the (long- and short-term) trends derived from the SDV with the trends of the Dunefoot. We do the same for the SDS with the MLW and MHW, and the SDBW with the Total and Dry Beach Width.

We determine the trends with the widely-used linear regression rate-of-change statistic, following the methodology presented in Digital Shoreline Analysis System (DSAS) User Guide Version 5.1 by Himmelstoss et al. (2021) and adopted by Hagenaars et al. (2018). This method computes a least-squares regression line (in short: linear fit) from a time series of indicator measurement data found for a certain transect. These time series span the temporal extent of the datasets introduced in Section 3.4. If a long enough period (10+ years) is selected, one could say the linear fit represents a long-term trend. Shorter periods would represent short- (<1 to 5y) to middle-term (5 - 10y) trends. The trends computed for every transect will be plotted in one graph to present a reach-wide overview of the trends. We aim to identify the differences and similarities between the structural trends of the SDBW and the JARKUS Beach Widths and their subcomponents.

The linear fits are computed according to the following equation:

$$y(t) = at + b \qquad\qquad \text{Eq. 4}$$

In which:

in case of the SDS, SDV, MLW, MHW and Dunefoot (e.g., the beach width's subcomponents):
- $y(t)$ $[m]$ represents the distance between the measured indicator and the origin of the transect at the time instance t;
- b $[m]$ represents the distance between the first measured indicator in the dataset and the origin of the transect;

in case of the SDBW, Total Beach Width and Dry Beach Width:
- $y(t)$ $[m]$ represents the size of the measured beach width at the time instance t;
- b $[m]$ represents the size of the first measured beach width in the dataset;

and overall:
- a $[m/y]$ represents the linear regression rate-of-change value for the considered indicator.

4 Results

This chapter analyses the detection and dynamics of the Satellite-Derived Beach Width (SDBW) along the Ameland coast and compares the data with in-situ measurements from the JARKUS dataset (as described in Section 3.5). The results in this chapter are relevant for answering research questions 3, 4 and 5 (see Chapter 1). SDBW data from composite (Section 3.4.1) and individual satellite images (Section 3.4.2) are separately analysed and compared with JARKUS data to assess the differences between these two alternate techniques. Per technique, first, the detection and dynamics of the subcomponents of the SDBW (i.e., the Satellite-Derived Vegetation line (SDV) and the Satellite-Derived Shoreline (SDS)) are analysed to help to understand and interpret the detection and dynamics of the SDBW. Section 4.1 presents the results from the composite image data, and Section 4.2 presents the results from the individual image data. In Section 4.3, we summarize the key findings from the results.

For ease of reading, the overview of the assessed study site is shown here again in Figure 22. This chapter frequently refers to the *dynamic area (*transects 300 to 700) and *uniform area* (transects 720 to 2100) because of their contrasting characteristics. This partition is based on the results found in the first analyses concerning the offset between the SDV and Dunefoot.
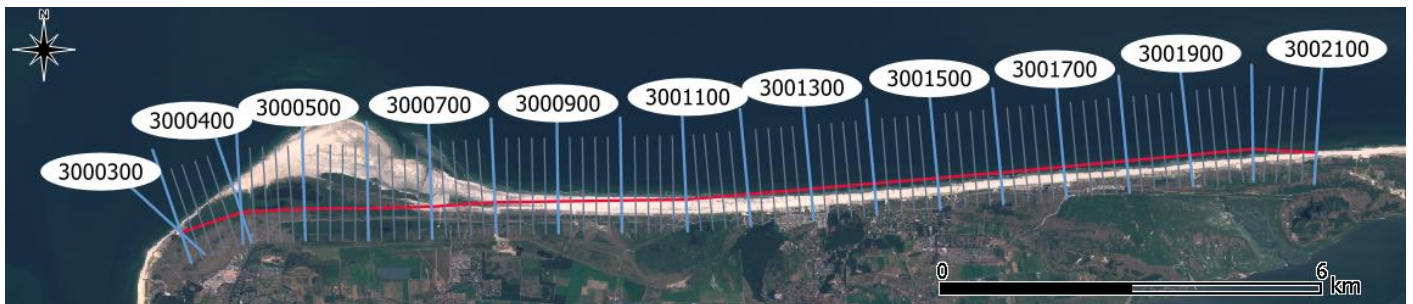
Figure 22 Ameland study site. The JARKUS transects (in blue) are labeled every 2 kilometers. The red line represents the RSP line. Sentinel-2 image (July 2018). Duplicate of Figure 11 (Section 3.2.2)

4.1 SDBW derived from composite Landsat images

This section analyses the SDV, SDS, and SDBW derived from composite Landsat images and compares those features with their counterpart JARKUS parameters. Section 4.1.1 and Section 4.1.2 elaborate on the offset between the SDV and the JARKUS Dunefoot and analyse and compare those parameters' long-term trends. Subsequently, Section 4.1.3 and Section 4.1.4 follow the same routine, but for the SDS, MLW and MHW. In Section 4.1.5, the findings of the first four sections come together when we analyse the SDBW and compare it to the beach widths from JARKUS.

4.1.1 Analysis of SDV detection and comparison with Dunefoot position

Figure 23 shows the temporal mean offset per transect between the SDV and the dunefoot position, where the temporal mean reflects the mean offset of the (max.) 477 composite images compared to the closest annual JARKUS survey over the period between November 1984 and November 2018. A positive offset value corresponds to an SDV that lies landward of the Dunefoot, and a negative value corresponds to an SDV that lies seaward of the Dunefoot. 92% of the offset values are positive for the total reach, at the dynamic and uniform areas; this accounts for 77% and 96%, respectively. Figure 24 shows the standard deviation of the measured offsets per transect. The standard deviation functions as a measure for the variability of the offset data around the transect its mean. This variability gives an indication of the precision or accuracy of the measurement tool. The first results indicate that the Dunefoot and SDV overall have a physical offset relative to each other, with a landward bias of the SDV relative to the Dunefoot, unrelated to the accuracy of the

detection method. Based on visual inspections of the image data and measured parameters, these offsets can be in the order of tens of meters, varying per transect.
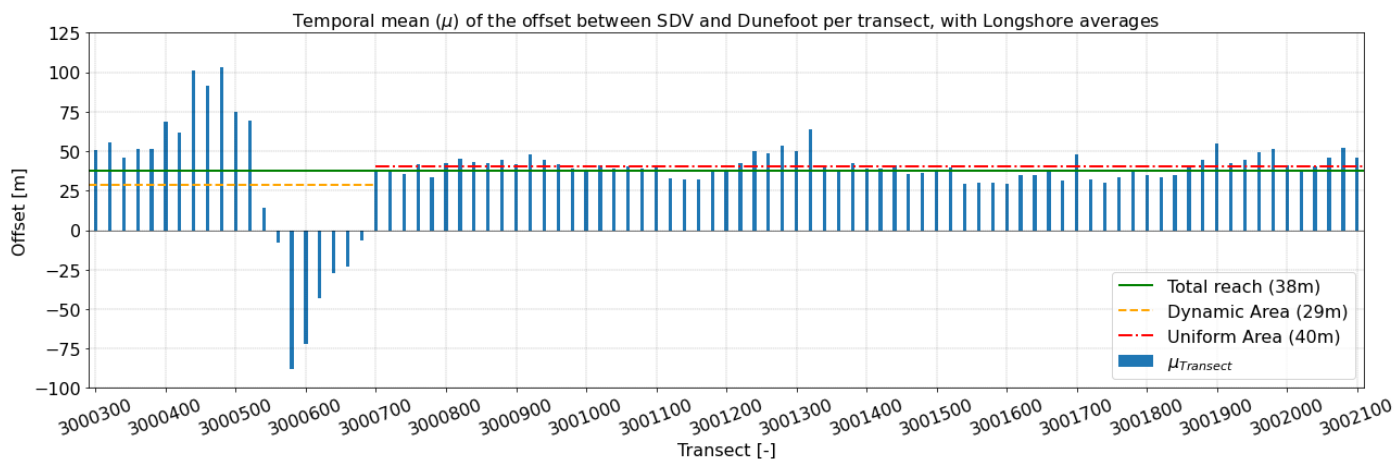
Figure 23 The blue bars show the temporal mean of the offset between the SDV and Dunefoot positions, per transect. The green line shows the longshore average of the temporal means for the total reach, the yellow dashed line for the dynamic area and the red dash-dotted line for the uniform area. Derived from the dataset of Landsat 5 and Landsat 8 composite images between 1984 and 2018.
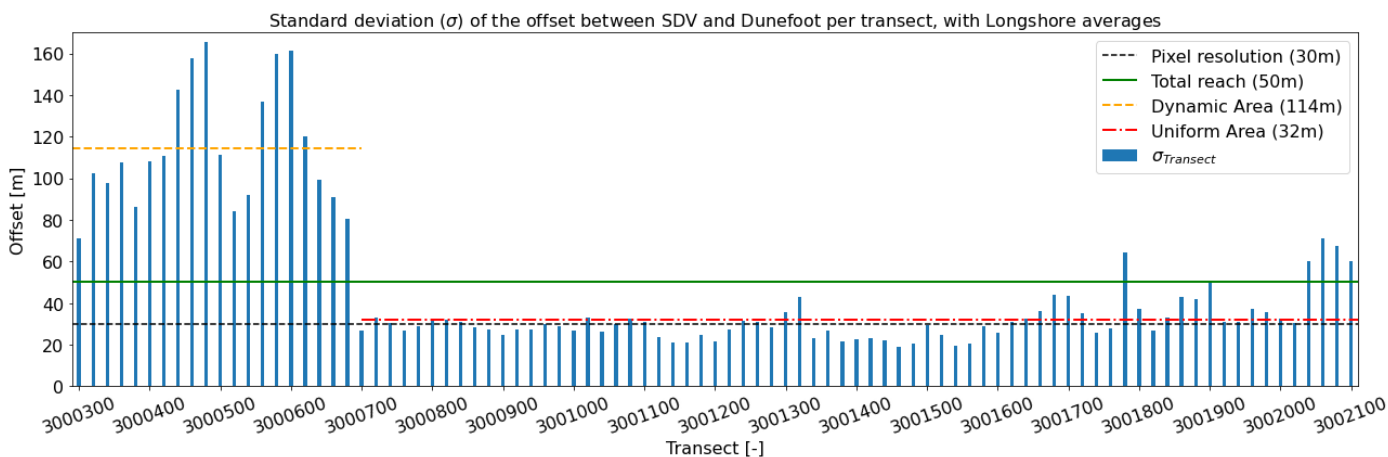
Figure 24 The blue bars show the standard deviation of the offset between the SDV and Dunefoot positions, per transect. The green line shows the longshore average of the standard deviations for the total reach, the yellow dashed line for the dynamic area and the red dash-dotted line for the uniform area. Derived from the dataset of Landsat 5 and Landsat 8 composite images between 1984 and 2018. The pixel resolution of the Landsat imagery is plotted as the black dashed line for reference.

Looking at the longshore averages of the data, we find a mean offset and standard deviation of 38 ± 50 m for the total reach. For the dynamic and uniform area, we find a mean offset and standard deviation of 29 ± 114 m and 40 ± 32 m, respectively. For the uniform area, we observe a relatively stable spatial pattern between the mean offsets per transect. At the uniform area, the temporal mean offset values are all positive (e.g., the SDV are located landward of the Dunefoot), and the average (40m) is close to the longshore average of 38 metres. We find the most significant offsets and standard deviations along the transects in the dynamic area. The offsets in the dynamic area are large and either positive or negative, which has to do with specific local geographic conditions. The spatial average of the offsets along the dynamic area is not that large because the positive and negative values per transect partly level each other out. On the other hand, the spatial average of the standard deviations (114m) measured along the dynamic area is very large and significantly influences the spatial average of the total reach (50m). Along the uniform area, the standard deviations are significantly smaller than in the dynamic area. The standard deviation along the uniform area (32m) is comparable to the satellite image's pixel resolution (30m). The latter implies that the accuracy of the detection of the SDV from Landsat composite images is in the order of the pixel resolution for areas where no deviating geographic features are present. We consider the uniform area of the studied reach to be representative of

the majority of non-urbanised beach-dune systems along the Holland coast. Site-specific observations of the dynamic and uniform areas are presented below.

The dynamic area

From Figure 23, along the dynamic area, two areas stand out; the area between transects 300 and 520 with relatively large positive offset values and the area between transects 520 and 700 with negative (and partly sizeable) offset values. We attribute these deviations to local geographic features that developed during the analysed 34-year period. The majority of the SDVs located seaward of the Dunefoot (negative offset values) can be ascribed to a specific (non-dune like) vegetated area that appears to show characteristics of a salt marsh, which are rare along Dutch sandy beaches. This salt marsh, named "Het Groene Strand" (the Green beach), developed between transects 540 and 680 from the year 2000 and onward (Krol, 2019). Over time, the development of the vegetation (in height and density) provided shelter for sediment to accumulate around the salt marsh, which provided a suitable habitat for embryo dunes to establish west of the salt marsh (transects 300 to 520). Hence, due to the accumulated sediment, the elevation-based dunefoot shifted in seaward position, and later the SDV position followed this seaward shift due to the sequential establishment of embryo dunes. We zoom in on the development of the SDV and Dunefoot and the relationship between those parameters at the dynamic area in Section 4.1.2 and Appendix D. The lag in the physical development of either dune foot or vegetation line relative to each other explains the high offset values between the SDV and Dunefoot positions at the dynamic area. This is in line with the relationship between sedimentation and vegetation; at locations where (dune or marsh) vegetation gets the chance to develop (in seaward direction), sedimentation accumulates around the new vegetation, subsequently reinforcing the development of both sedimentation and vegetation. This process works both ways, be it with a certain delay of the other parameter. One could say that when the geographic conditions are right, the SDV and Dunefoot act as predictors of each other.

The uniform area

Apart from a few outliers, the offset does not deviate much between transects in the uniform area. The SDV mostly shows a consistent offset with the dunefoot between 25 to 50 meters along the uniform area. Analysis of the data shows that this represents the actual situation of the beach at the uniform area, e.g., the elevation contour +3m NAP defined as the dunefoot lies at a distance from the most seaward vegetation contour. Along the area, several transects, such as transects 1320, 1700 and 1900, show mean offset values that deviate relative to the adjacent transects and the rest of the uniform area. We attribute these outliers to the presence of local beach entrances and areas of dune erosion, see Figure 25. At these inlets, the detected SDV vector bends land-inward, whereas the JARKUS dunefoot is not, or only slightly, affected by the presence of these inlets and, therefore, the offset between dunefoot and SDV is more significant (50+ m) for those transects compared to their neighbouring transects.

Additionally, we note various other observations from the images and SDV vectors depicted in Figure 25. As described earlier, we see a clear physical difference (offset) between the Dunefoot (defined as the +3m elevation contour) and the vegetation line. For the beach along the transects in Panel (a), you could say that the SDV represents the landward border of the beach (width) better than the Dunefoot. Whereas, in Panel (b), you could say it is the other way around. Based on visual inspection of the SDVs displayed in the figure and their corresponding satellite images, we find that the position of the vegetation line detected by the SDV detection method can vary per composite image, regardless of the image quality or dynamics of the actual vegetation contour. The latter aligns with expectations for the SDVs detected from Landsat images because the Landsat images have a 30-meter pixel resolution.

Figure 25 Two sections of the Ameland reach to display the beach inlets and areas with dune erosion. The turquoise dots show the 2018 Dunefoot position, the yellow vector shows the SDV from a 180-day composite image derived from Landsat images 90 days before and after 23-05-2018, the pink vector shows the SDV from a 180-day composite image derived from Landsat images 90 days before and after 02-08-2018. Panel (a) shows the reach between transects 1280 and 1360 and Panel (b) shows the reach between transects 1860 and 1940. (TripleSat image, 80cm pixel resolution, August 2018, acquired from www.satellietdataportaal.nl)

Analysis of the satellite images shows that errors due to swath related issues, such as depicted on panels (a) and (b) from Figure 20, sometimes hamper the correct detection of the SDV, regardless of the presence of clouds or cloud shadows. Something appears to go wrong with the overlap of the satellite image swaths. These errors frequently occur for Landsat 5 images but not for Landsat 8 images. With the introduction of Landsat 8 in 2013, the errors do not show anymore. Hence, the issue has appeared solved since then. Table 4 provides the longshore averages of the temporal mean offset and standard deviation per transect of all transects along the uniform area. Overall, the offset and the standard deviation of the Landsat 8 data (33 ± 24m) are smaller than the Landsat 5 data (43 ± 32m).

Table 4. Average of the Mean and standard deviation of the SDV-Dunefoot offset per transect for the uniform area, from Landsat 5 and Landsat 8 data.

Uniform area	Mean offset	Standard deviation
Satellite mission	*μ (m)*	*σ (m)*
Landsat 5	43	32
Landsat 8	33	24

Figure 26 shows the standard deviation of the offset between the SDV and Dunefoot for each transect along the uniform area for the Landsat 5 and Landsat 8 data separately. The figure shows that the standard deviation of the Landsat 8 data is for most transects smaller than the Landsat 5 data. The latter implies that the measured data from the Landsat 8 has a smaller variability (e.g., a higher accuracy) than data from Landsat 5. We find exceptions at transects where we see beach entrances and areas of dune erosion. Here the standard deviation for both satellites is relatively high and comparable to each other, which we relate to the local physical conditions. It is reasonable to assume that the relatively large standard deviations of the Landsat 5 data found for the other transects are (partly) explained by the swath related issues. It is also possible that change of physical conditions during the different periods (1984-2011 versus 2013-2019) might cause this difference, but from extensive visual analysis of the Landsat images, we conclude from the frequency of occurrence of the swath related issues that they are the most probable cause of influence.
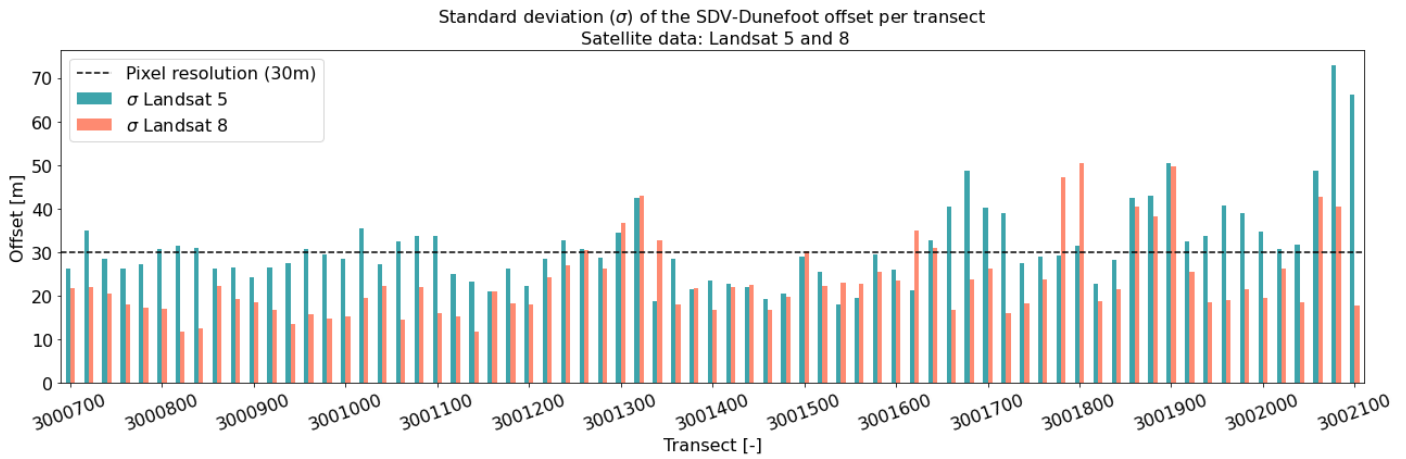
Figure 26. Standard deviation of the SDV-Dunefoot offset per transect along the uniform area. Data derived from Landsat 5 (1984-2011) and Landsat 8 (2013-2019) images separately.

4.1.2 Analysis of SDV dynamics in time in comparison with Dunefoot trends

This section elaborates on the analysis of the SDV dynamics and the comparison of the long-term trends of the SDV with the long-term trends of the JARKUS Dunefoot. Per transect, we made time series of all the measured positions of the JARKUS dunefoot and the SDV in the considered period (1984-2018). For example, Figure 27 shows the time-series of Transect 2000 (at the uniform area), which displays the positional data and the linear fits derived from the Dunefoot and SDV data. The legend displays the growth and decay values of the regression lines with the standard error of the regression (or mean). The standard error functions as a measure for the goodness of the regression line. The smaller the number, the better the goodness of the fit. Regarding the long-term trends, growth corresponds to a net seaward movement, and decay corresponds to a net landward movement.
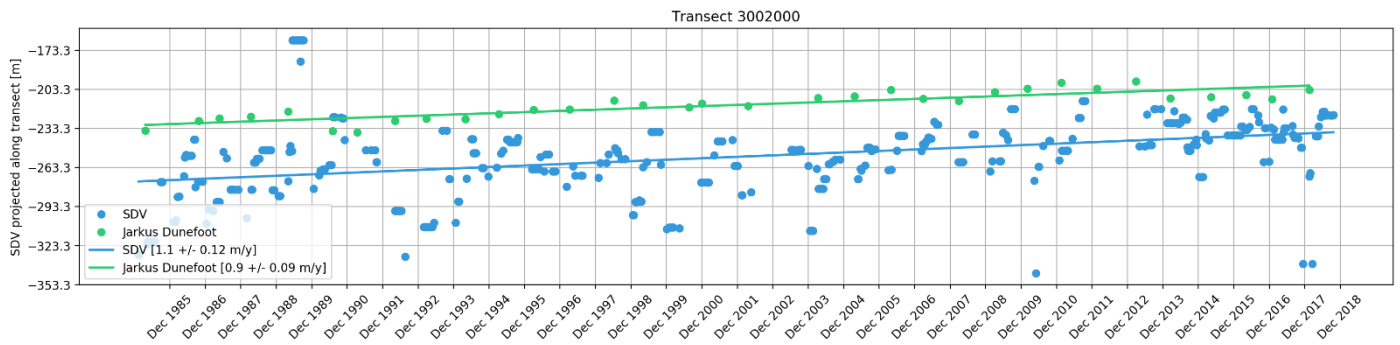
Figure 27 Time-series of 34 years data of dunefoot and SDV positions along Transect 2000. The linear fits of the Dunefoot and SDV positions give an indication of the long-term trends. The Dunefoot and SDV positions are relative to RSP, e.g., the origin of the

We note several things from the figure. We observe multiple outliers and a noticeable seasonal variation from the measured SDV data. It appears the spread of the positional data is broader for data derived from the Landsat 5 images (1984-2011) compared to the positional data derived from the Landsat 8 images (2013-2018). The latter confirms the observation in Section 4.1.1 about the difference in SDV detection accuracy between the two satellite missions. Furthermore, we observe a variable but relatively consistent offset between the dunefoot and the SDV (e.g., the distance between the regression lines is about 40-50 meters), as presented in Section 4.1.1.

Another thing we note is a yearly seasonal fluctuation of the SDV position. We observe this from the annual sequences of seaward moving SDV positions relative to the 34-year trend line. Section 4.2.1 presents a thorough analysis of this fluctuation based on SDV detected from single images.

Figure 28 displays the 34-year long-term trends of the Dunefoot and SDV for all transects along the studied reach. Apart from a few exceptions, the reach is mainly characterised by growing trends. Hence, over 34 years, we see a nett seaward movement of the Dunefoot and vegetation line. There is a clear difference between the magnitude of the long-term trends along the dynamic area and uniform area. The transects in the dynamic area show significantly larger growth values (up to 12 m/y) than the transects in the uniform area, where the trends do not surpass values of 2.5 meters per year. For the uniform area, we observe that the SDV and Dunefoot trends are very similar. Per transect, the trends show comparable magnitudes of growth.
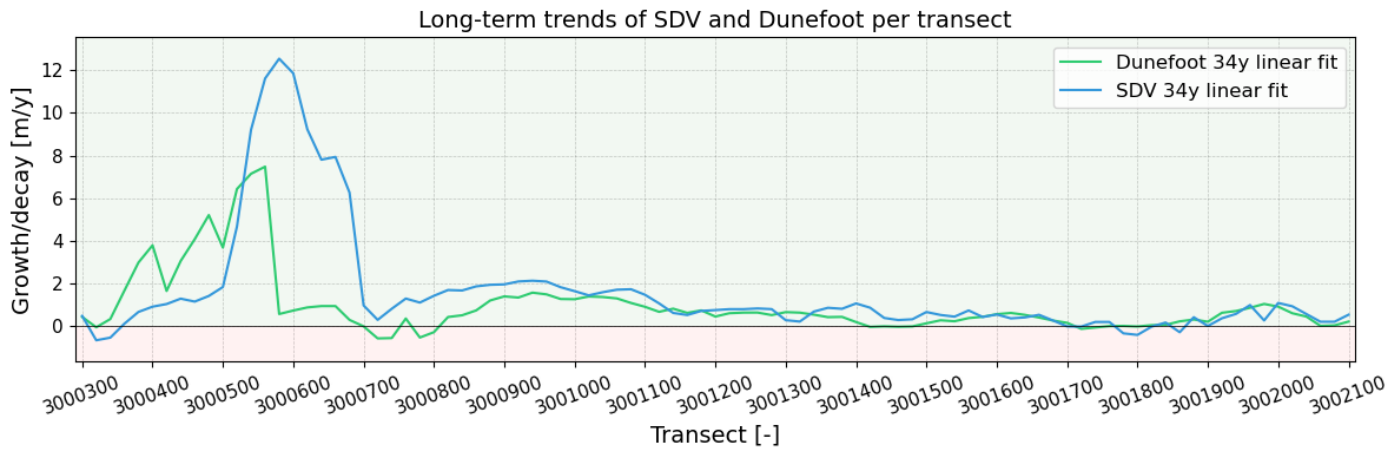
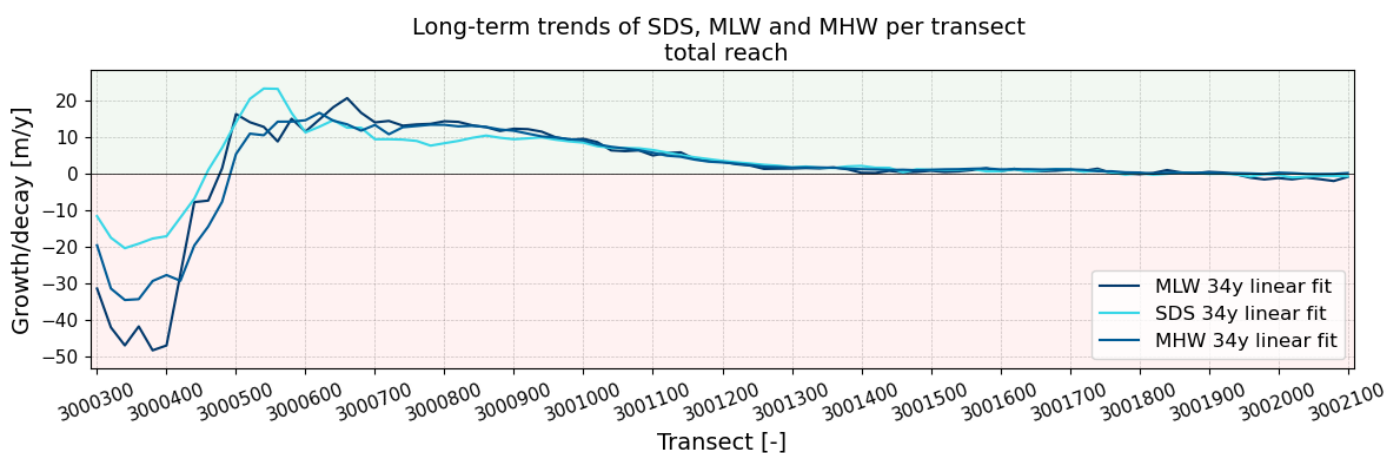*Figure 28 Long-term trends of the Dunefoot and SDV on the Ameland study reach, per transect. The trends are computed as 34-year linear fits of the Dunefoot and SDV positional data. SDV data derived from Landsat 5 and Landsat 8 composite satellite images, between 1985-01-01 and 2018-12-31.*

The time series of Transect 2000 in Figure 27 illustrates a strong resemblance between the trends of the Dunefoot and SDV; 0.9 ± 0.09 m/y versus 1.1 ± 0.12 m/y. Such a resemblance/correspondence of trends is common for the transects along the *uniform area* (transects 700 to 2100), where the magnitude and direction of the Dunefoot and SDV trends correspond well with each other. Along the dynamic area of the reach, the Dunefoot and SDV trends show significantly less resemblance with each other. See, for example, the Dunefoot and SDV trends in the time series of Transect 560 in Figure 29; 7.5 ± 1.35 m/y versus 11.4 ± 0.40 m/y. This deviation is explained by the unique geographic characteristics of the area (the salt marsh introduced in Section 4.1.1 and the "delayed" sedimentary developments surrounding the marsh), to which we ascribed a certain predictive reciprocal relationship between the SDV and Dunefoot. We elaborate more extensively on the findings on the Dunefoot and SDV dynamics along the transects of the dynamic area in Appendix D.
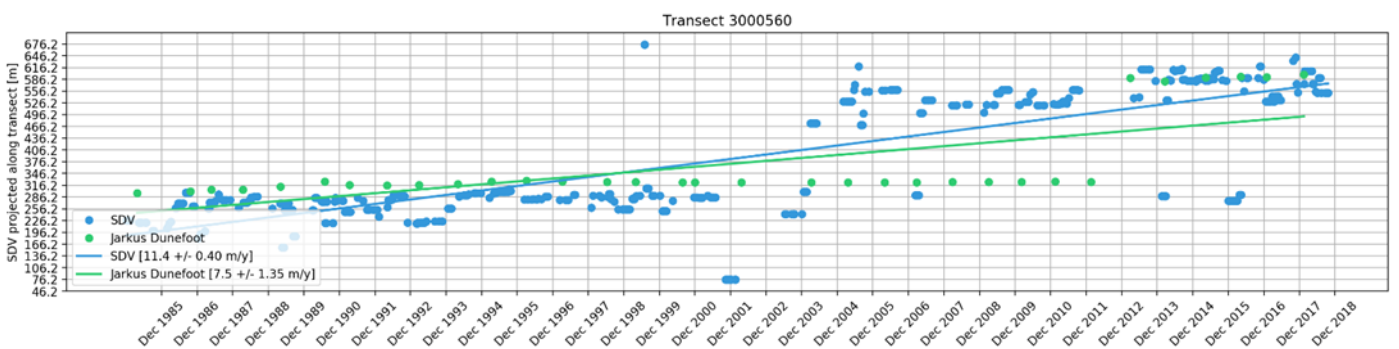
Figure 29 Time-series of 34 years data of dunefoot and SDV positions along Transect 560. The linear fits of the dunefoot and SDV position give an indication of the long-term trends. The dunefoot and SDV positions are relative to RSP, e.g., the origin of the transect.

Another finding worth mentioning about the time series of the transects along the Dynamic area is that, due to the abovementioned geographic characteristics, the SDV and Dunefoot linear fits show trend breaks at

different locations in time over the considered period. For example, the time series of Transect 560 in Figure 29 shows such trend breaks for the SDV (around 2003) and Dunefoot (around 2012). These trend breaks make it questionable whether using a 34-year linear fit to represent long-term trends of the SDV and Dunefoot at the transects along the dynamic area is fit for analysis. For example, the linear fit might give a correct representation of the relative development of either parameter over 34 years (and predict the position of the other parameter) but does not correctly display how this feature developed since the trend break occurred. In that case, it would be more reasonable to look at linear fits of shorter periods. Then the question arises: what period does one select for the linear fit? The positions in time of the trend breaks vary between transects and parameters because the development of the Dunefoot and vegetation line vary in space and time. Hence, the time-series of the transects neighbouring transect 560 show trend breaks of the SDV and Dunefoot at different positions in time. The latter explains the differences between the SDV and Dunefoot trends along the dynamic area, as seen in Figure 28.

4.1.3 Analysis of SDS detection and comparison with MLW and MHW positions

Figure 30 and Figure 31 show the temporal means and standard deviations per transect of the offsets between the SDS and MLW (panel a) and between the SDS and MHW (panel b). In Figure 30, a positive offset value corresponds to an SDS that lies landward of MLW or MHW, and a negative value corresponds to an SDS that lies seaward of MLW or MHW.

Figure 30 The blue bars in panel a) show the temporal mean of the offset between the SDS and MLW positions, per transect. The orange bars in panel b) show the temporal mean of the offset between the SDS and MHW positions, per transect. The green line shows the longshore average of the temporal means for the total reach, the yellow dashed line for the dynamic area and the red dash-dotted line for the uniform area. Derived from the dataset of Landsat 5 and Landsat 8 composite images between 1984 and 2018

Figure 31 The blue bars in panel a) show the standard deviation of the offset between the SDS and MLW positions, per transect. The orange bars in panel b) show the standard deviation of the offset between the SDS and MHW positions, per transect. The green line shows the longshore average of the temporal means for the total reach, the yellow dashed line for the dynamic area and the red dash-dotted line for the uniform area. Derived from the dataset of Landsat 5 and Landsat 8 composite images between 1984 and 2018

Looking at the longshore averages of the SDS-MLW offset, we find a mean offset and standard deviation of 253 ± 165 m for the total reach, 519 ± 446 m for the dynamic area and 178 ± 85 m for the uniform area. For the SDS-MHW offset data, we find a longshore average of the temporal mean offset and standard deviation of 57 ± 132 m for the total reach, 216 ± 345 m for the dynamic area and 12 ± 72 m for the uniform area. One can immediately observe that the offset between SDS and MHW is much smaller than the offset between SDS and MLW for every transect, implying the SDS has a bias towards the MHW. Furthermore, the temporal means and standard deviations of the SDS-MLW and SDS-MHW offsets are relatively high compared to those of the SDV-Dunefoot offset. The latter is likely related to (a) the tidal variability of the shoreline position, (b) the landing of the Bornrif sandbank (see Section 3.2.1), and (c) the natural or artificially induced morphological variability of the shore(line). At Ameland, the distance between the MLW and MHW positions is frequently in the order of (several) 100 meters, resulting in high variability of the shoreline position, caused solely by the tidal variation, explaining the overall high offset values. Furthermore, we again observe significant differences between the offsets found at the dynamic and uniform areas. Note: These differences are separated less discretely between the confinements of the dynamic and uniform area since the initial definition of those areas was based on the results of the SDV-Dunefoot offset values (see Figure 23 and Figure 24). The substantial offset values and standard deviations along the dynamic area are mainly explained by the landing of the Bornrif sandbank between 1980 and 1985. During the studied period, the MLW and (to a lesser extent) MHW positions were frequently measured at the location of the offshore sandbank before it landed onshore, whereas the SDS is derived as the most landward optically discernible

shoreline position, neglecting the offshore sandbank. This measurement difference resulted in offsets larger than 1000 meters for several periods, explaining the high mean offsets and standard deviations.

For the standard deviations along the uniform area, we observe a more stable pattern, which for a large share of the transects is in the order of the pixel resolution (see transects 1100 to 2100 in Figure 31, panel b). The standard deviations of the SDS-MLW offset and the SDS-MHW offset are more similar to each other than their temporal means, which makes sense because the core factor in those standard deviations is the SDS, which is the same for both offset calculations.

We can think of various reasons for the tendency of the SDS towards the MHW. The principal reason is that we expect that this tendency is related to wave run-up or soil moisture after high water or wave run-up. At locations where the sand is still wet, the soil can still reflect as if it were water (e.g., the sand pixels show similar NDWI values as water), although the tide has already lowered. Another reason could be that, since we look at composites, the most landward located shoreline of the shorelines of the underlying satellite images might be dominant in the generation of the SDS. To learn more about this, we will analyse the position of the SDS detected from individual images relative to the MLW and MHW in Section 4.2.2.

4.1.4 Analysis of SDS dynamics in time in comparison with MLW and MHW trends

This section briefly elaborates on the analysis of the SDS dynamics and the comparison of the long-term trends of the SDS with the long-term trends of the MLW and MHW. Figure 32 shows the 34-year linear fits of the SDS, MLW and MHW per transect. We see that the trends show similarities in direction (e.g., either growth or decay) but differences in magnitude. At the most western transects, 300 to 500, magnitudes of the MLW and MHW trends are much larger than the trends of the SDS. From transect 500 and more eastward, the trends show more similarities in magnitude as well. Analysis of the trends shows the landing of the Bornrif sandbank and its eastward migration, e.g., the sandbank landed on the western island tip around or just before the start of the Landsat-5 mission in 1984. Subsequently, due to the nett eastward sea currents, the sandbank starts eroding on the western side (Transects 300 to 500) after its attachment, and the sand migrates eastward. The sediment is widely spread out over the transects east of the western tip (beyond Transect 500), which can also be seen in Figure 13 in Section 3.2.1, displaying the morphological development of Ameland.

Figure 32 Long-term trends of the MLW, SDS and MHW on the Ameland study reach, per transect. The trends are computed as 34-year linear fits of the MLW, SDS and MHW positional data. SDS data derived from Landsat 5 and Landsat 8 composite satellite images, between 1985-01-01 and 2018-12-31

The SDS, MLW and MHW trends are of a larger scale than the trends of the SDV and Dunefoot. For the SDS, MLW and MHW, the minima and maxima lie between -50 and +25 m/y. Whereas, for the SDV and Dunefoot, these values lie between -1 and +12,5 m/y. This difference is in line with expectation since the seaward border of the beach is generally a more dynamic feature than the landward border of the beach. As mentioned in

, the dynamics of the SDS do not precisely follow the confinements of the previously introduced dynamic and uniform areas but do dominantly occur on the western side of the island.

4.1.5 Analysis of SDBW size and dynamics and comparison with JARKUS beach widths

Now that we know what the SDV and SDS detected from composite Landsat images represent in terms of position and trends, we will look at the derivation of the two parameters, the size and trends of the SDBW.

SDBW size compared to JARKUS beach widths

Figure 33 shows the temporal means per transect of the difference between the SDBW and Total Beach Width (panel a) and between the SDBW and Dry Beach Width (panel b). Note: a positive (negative) value equals an SDBW larger (smaller) than the Total or Dry Beach Width. The figure depicts the longshore averages of the temporal means for the total reach, the dynamic and the uniform area. The differences between the SDBW and Total Beach Width and SDBW and Dry Beach Width are -216m versus -19m for the total reach. These numbers indicate that the SDBW size is more similar to the Dry Beach Width than to the Total Beach Width. We see that (especially for the Western transects) the offset between the waterline parameters (up to 700m for SDS-MLW and 400m for SDS-MHW) has a dominant effect on the difference in beach width sizes, compared to the effect of the SDV-Dunefoot offset (max. ±100m). For the uniform area, the positions of the SDV and Dunefoot have a more significant influence, especially on the Dry Beach Width size.

Figure 33 The panels in this figure show the temporal means of the difference between the size of the SDBW and Total Beach Width (blue bars in panel a)), and the size of the SDBW and Dry Beach Width (orange bars in panel b)), per transect. The green line shows the longshore average of the temporal means for the total reach, the yellow dashed line for the dynamic area and the red dash-dotted line for the uniform area. Derived from the dataset of Landsat 5 and Landsat 8 composite images between 1984 and 2018.

SDBW dynamics compared to JARKUS beach widths

Figure 34 displays the long-term trends of the SDBW and JARKUS data between 1984 and 2018. The three panels display the trends [m/y] of the SDV with Dunefoot, SDS with MLW and MHW and SDBW with the Total and Dry beach widths. From the first two panels in the figure, we observe that the SDS, MLW, and MHW trends along transects 300 to 1300 are significantly larger than the SDV and Dunefoot trends, apart from the SDV and Dunefoot trends between transects 500 to 700. Therefore, the magnitudes of the beach width

dynamics are mainly driven by the shoreline components. The SDBW and JARKUS beach width trends are similar in direction (e.g., growth or decay) for most transects but less similar in magnitude. For transects 300 to 1000, the SDBW trends correspond most to the Dry Beach Width; for transects 1000 to 2100, the SDBW, Total and Dry Beach Width trends are more similar to each other (when looking at this scale).
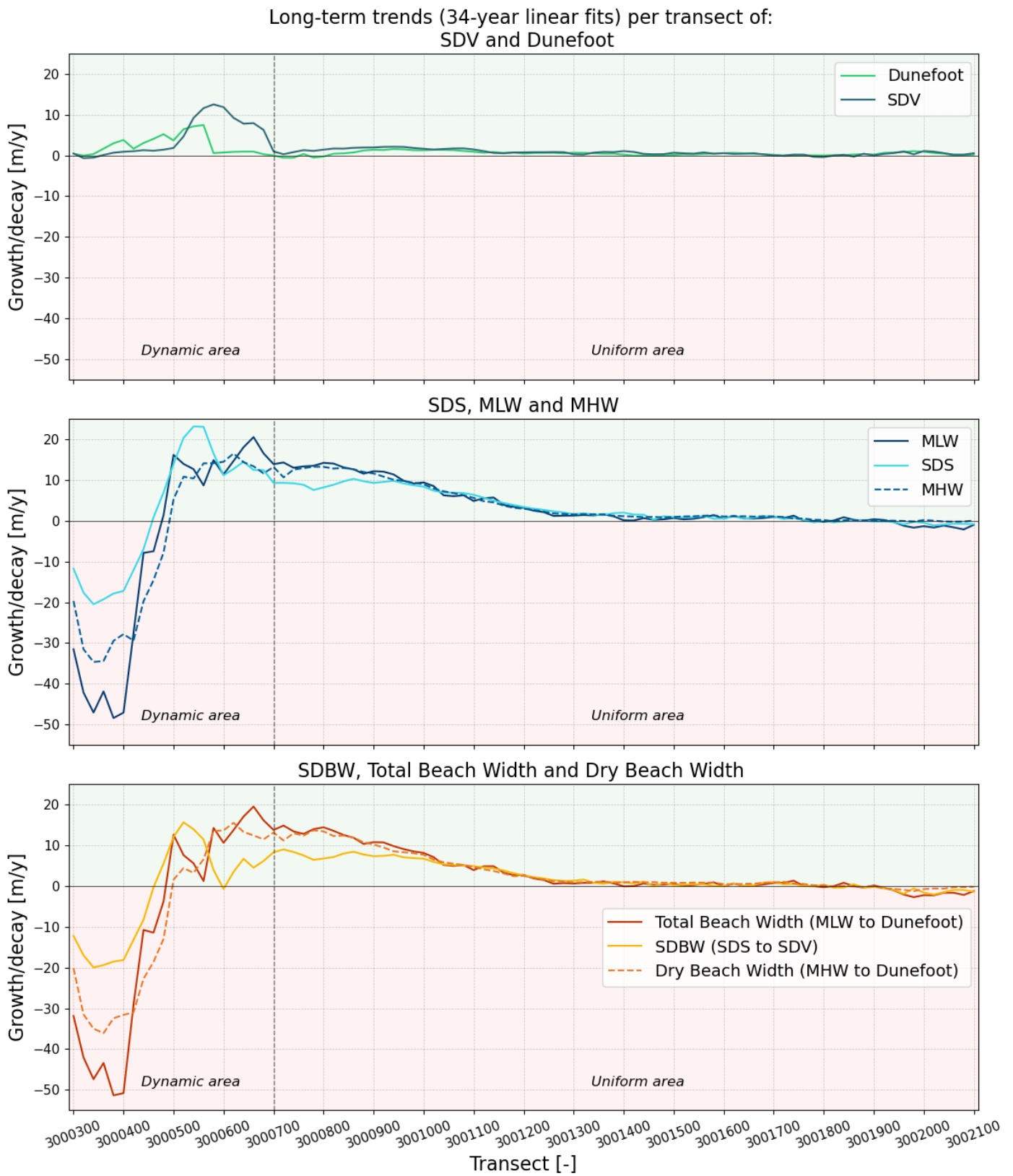
Figure 34 Long-term trends (34-year linear fits) per transect of the SDV and Dunefoot (panel a), SDS, MLW, MHW (panel b) and SDBW Total Beach Width and Dry Beach Width (panel c). Derived from the dataset of Landsat 5 and Landsat 8 composite images between 1984 and 2018 and 1984 to 2018 JARKUS surveys.

Figure 35 displays the time series of Transect 960 with the SDS, MLW, MHW, SDV and Dunefoot positions in the upper panel and the SDBW, Total and Dry beach width sizes in the lower panel. The annual data points of the JARKUS CSI's are connected through lines to give a (fictive) impression of their intra-annual development relative to (the multitude of) the satellite-derived CSI's. The data in the figure gives an overview of the results from composite images up to now: (1) the SDV has a consistent offset with the Dunefoot and is positioned landward of the Dunefoot, (2) the SDS is on average positioned close to the MHW with a seaward bias, (3) the SDBW size lies between the Total Beach Width and the Dry Beach Width with a bias towards the Dry Beach Width, (4) the spread of the Landsat 8 data (2013-2018) is more narrow (accurate) than the Landsat 5 data (1984-2011). The extreme outliers of the SDS and (related) SDBW positions noticeable in the graph are assigned to low-quality Landsat images. On those images, clouds or other errors likely caused the computation of unrealistic SDS vectors that were not omitted by the data filter set as max. ±3σ deviation of the temporal mean position. Since the standard deviation of the SDS position is relatively high for the transects at the dynamic area, the ±3σ margin can be pretty wide, which sometimes causes these extreme outliers to remain unfiltered.

Looking at the time series of the other transects along the study reach, we primarily observe the same traits, with a few exceptions for the transects along the dynamic area (e.g., the development of "Het Groene strand"). Analysing the time series of each transect gives much insight into the (morpho-)dynamics of the CSI's along the northern coast of Ameland. For example, the landing of the Bornrif sandbank and its subsequent eastward migration along the Ameland shoreline is easily recognizable from the time series; see the bulge in the shoreline and beach width parameters on the right side of the time series of Figure 35.
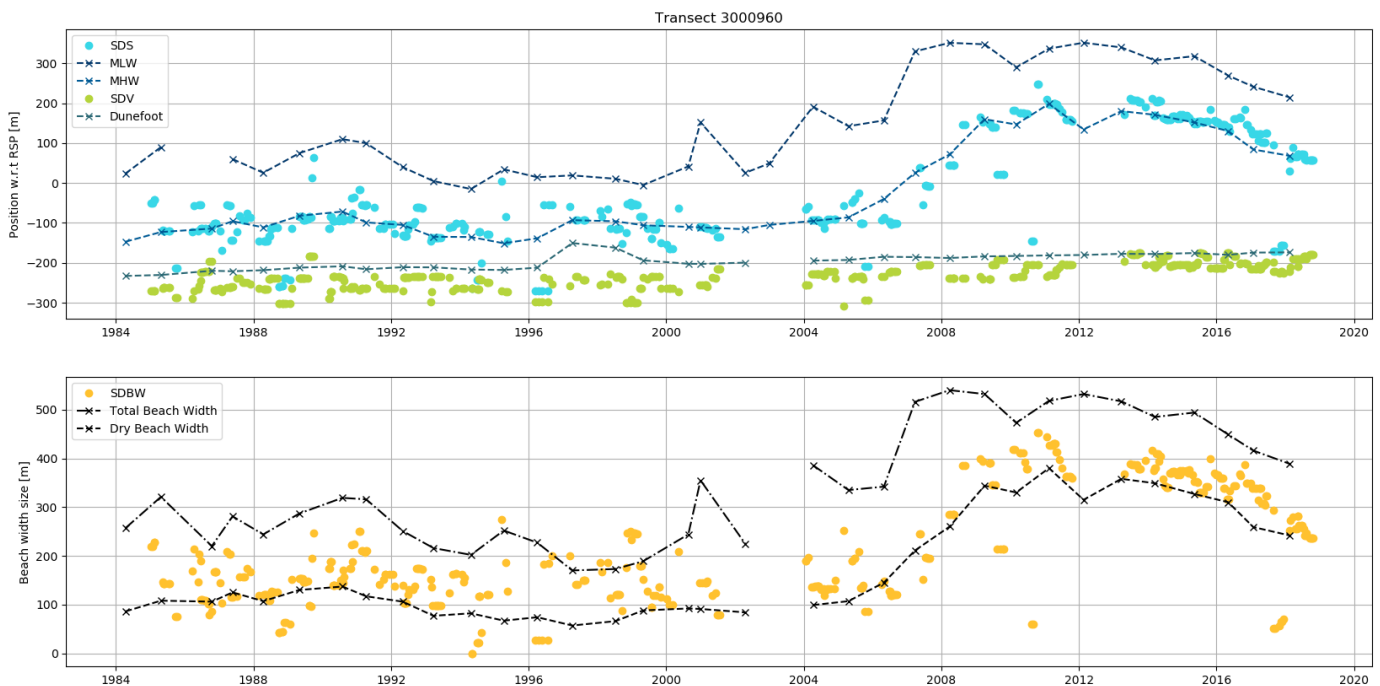
Figure 35. Time series of the positions of SDS, SDV, MLW, MHW and Dunefoot (upper panel) and the sizes of the SDBW, Dry Beach Width and Total Beach Width (lower panel) along Transect 960.

4.2 SDBW derived from individual Sentinel-2 images

In this section, we present the results from the analyses of the SDBW from individual Sentinel-2 images acquired between 2015 and 2019. Section 4.2.1 elaborates on the offset between the SDV and the JARKUS Dunefoot and analyses the intra-annual (seasonal) differences of the SDV detection. Subsequently, Section 4.2.2 looks at the offset between the SDS, MLW and MHW and gives special attention to the positional spreading of the SDS relative to MLW and MHW. Section 4.2.3 analyses the difference in size between the SDBW and JARKUS beach widths and looks at the SDBW and JARKUS Beach Width trends.

4.2.1 Analysis of SDV detection and comparison with Dunefoot position

In this section, we look at the intra-annual variation of the SDV by looking at SDVs detected from individual Sentinel-2 images and comparing them with the Dunefoot. Figure 36 and Figure 37 show the offset's temporal mean and standard deviation between the SDV and Dunefoot per transect, based on the dataset of individual Sentinel-2 images and JARKUS surveys between July 2015 and April 2019. Both figures display the longshore averages for the total reach and the two distinct areas. A positive offset value in Figure 36 corresponds to an SDV that lies landward of the Dunefoot, and a negative value corresponds to an SDV that lies seaward of the Dunefoot. We find a longshore average of the temporal mean offset and standard deviation of 39 ± 24 m for the total reach. For the dynamic and uniform area, we find a mean offset and standard deviation of 8 ± 52 m and 48 ± 16 m, respectively. As for the composites, we again observe a clear distinction between the dynamic and uniform areas. The dynamic area shows large (positive and negative) mean offset and standard deviation values per transect, whereas the uniform area shows a stable pattern of consistent offset values and relatively low standard deviations. Along the uniform area, we only find some outliers relative to the adjacent transects for transects where beach inlets are present, similar to the findings we presented in Section 4.1.1.
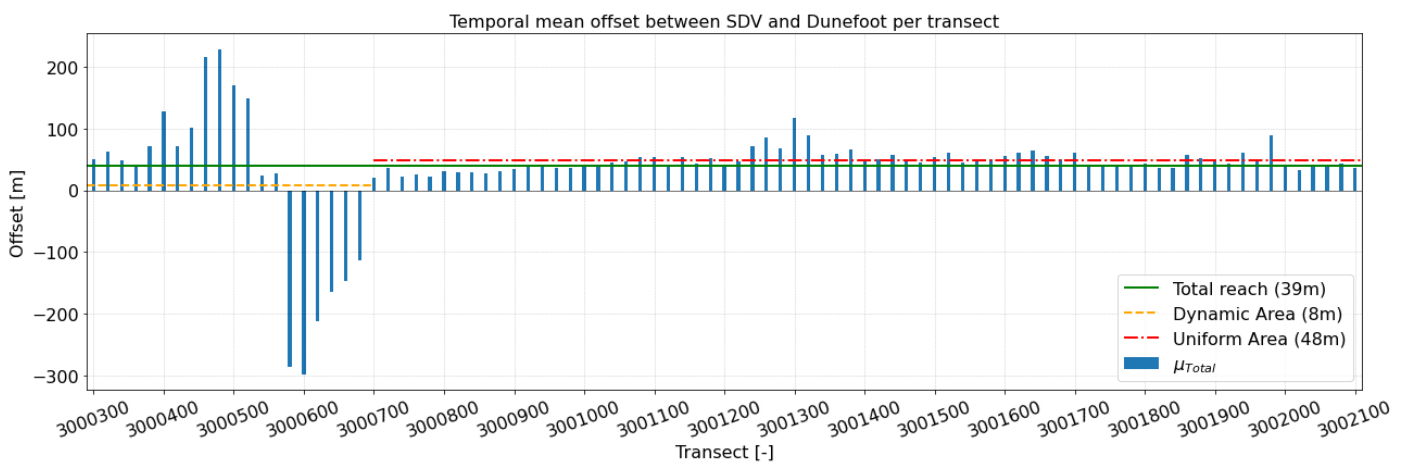
Figure 36 The blue bars show the temporal mean of the offset between the SDV and Dunefoot positions, per transect. The green line shows the longshore average of the temporal means for the total reach, the yellow dashed line for the dynamic area and the red dash-dotted line for the uniform area. Derived from the dataset of individual Sentinel-2 images between July 2015 and April 2019.

The longshore average of the temporal mean offsets derived from the individual Sentinel-2 images (μ=39m) is in the same order as the 180-day Landsat composite images (μ=40m). The longshore average offset at the uniform area is larger for the individual Sentinel-2 images (μ=48m) than for the composite Landsat images (μ=40m), where you might have expected it to be the other way around. We do not pinpoint this difference to one particular reason. However, likely explanations are related to (1) the Dunefoot and SDV simply being further apart physically in the period from 2015 to 2019 relative to the period from 1984 to 2019, (2) the higher standard deviation and lesser quality of the measurement data derived from the composites resulting in a less accurate offset value, or (3) the seasonal variability of the SDV position being averaged out by the composite technique. The longshore average of the standard deviations is considerably lower for the Sentinel-2 data (σ=24m) than the Landsat data (σ=50m). The latter is in line with expectation because of the difference

in the pixel resolution of both satellite missions (Sentinel-2 = 10m, Landsat 5 & 8 = 30m). The longshore average of the standard deviations along the uniform area (16m) is in the order of one and a half times the pixel resolution.

For the remainder of this section, we analyse the seasonal variation of the SDV position. In this analysis, we focus on the uniform area; we exclude the dynamic part of the reach because the data is less stable there.
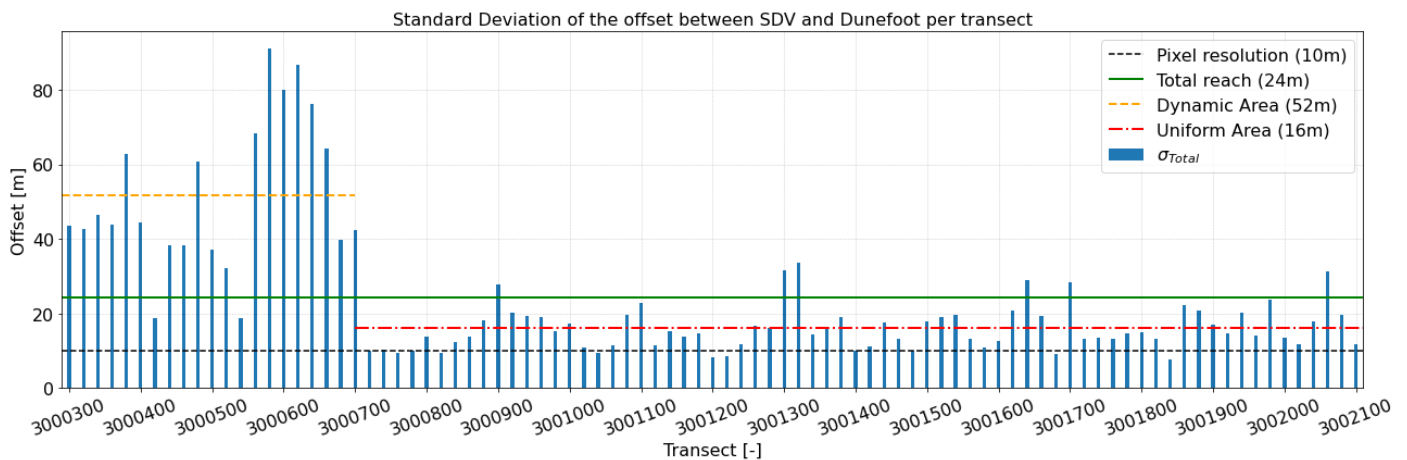
Figure 37 The blue bars show the standard deviation of the offset between the SDV and Dunefoot positions, per transect. The green line shows the longshore average of the standard deviations for the total reach, the yellow dashed line for the dynamic area and the red dash-dotted line for the uniform area. Derived from the dataset of individual Sentinel-2 images between July 2015 and April 2019. The pixel resolution of the Landsat imagery is plotted as the black dashed line for reference.

Section 4.1 showed that the SDV position varies over the year. We assume that this is caused by the seasonal variation of the vegetation greenness related to, among others, photosynthesis and rainfall, causing a variation of the NDVI pixel values throughout a year (Yang et al., 2017). We find a maximum, most seaward, position of the SDV in summer and a minimum, most landward, position of the SDV in winter. When taking the temporal average of the offset between the SDV and the Dunefoot, the seasonal variation of the SDV position is averaged out. For the following analysis, we focus on the area between transects 720 and 2100. We exclude the area between transects 300 and 700 because the positional data is less stable there, as we found in Section 4.1.

Table 5 shows the longshore averages of the temporal mean offsets and standard deviations of the transects along the uniform area for each astronomical season and the total dataset. For the uniform area, the SDV is always located landward of the Dunefoot. Therefore, a smaller offset means a more seaward positioned SDV relative to the Dunefoot. The longshore average of the temporal mean offsets along the uniform area is 48m. The average offset is the smallest in summer (39m) and largest in winter (63m). As we hypothesised earlier, this confirms that the SDV is located most seaward in summer and most landward in winter. Furthermore, the standard deviations per season show that the standard deviation is largest (15m) in spring and lowest in the other three seasons (12m). The fact that we find the most significant standard deviation in spring is due to the relatively long transition phase (in spring) from the SDV's "winter" position to the "summer" position. For the total dataset (e.g., all images through the seasons combined), the standard deviation is the largest overall (16m). The latter is due to the seasonal variability of the SDV position throughout the year, which is explained by the relatively large difference (Δ=24m) between the average winter and summer positions of the SDV.

Table 5 This table shows the spatial averages of the temporal mean offset between the SDV and the Dunefoot and of the related standard deviation for the uniform area of the Ameland study reach. The SDVs are derived from a collection of Sentinel-2 images between 2015-07-01 and 2019-04-11. The statistics are determined for the total collection and per season. The SDVs are compared with the Dunefoot of the most recent JARKUS survey relative to the acquisition time of the used satellite images.

SDV Selection	Mean offset $\mu(m)$	Standard deviation $\sigma(m)$	Sample Size (-)
Spring	50	15	33
Summer	39	12	28
Autumn	43	12	13
Winter	63	12	15
Total Dataset	48	16	89

Figure 39 shows the time series of the SDV and Dunefoot in the considered period (July 2015- April 2019) except for the 2019 JARKUS survey. Figure 38 shows the same data but then accumulated over one year to highlight the differences in the SDV detection throughout the annual seasons. Analyses of time-series of the positional SDV data, for example, the time series in Figure 39, help to further understand the behaviour of the SDV variation throughout the seasons. Along multiple transects, we see that the seasonal variation of the SDV position (due to the vegetation greenness) shows a somewhat skewed pattern. In spring, the vegetation starts blooming and gradually becomes greener, which is found in the gradient of the SDV position between the more landward positions in winter towards the more seaward positions in summer. In early summer, the vegetation seems to attain a maximum value of greenness. From that moment onward, the detection of the SDV becomes stable. The SDV remains relatively long on the "summer position". From October to December, the vegetation gradually becomes less green, and the SDV position moves to the more landward "winter position". The migration of the SDV position from summer to winter position (highest to lowest greenness value), and vice versa, seems more gradual, or slow, from winter to summer than from summer to winter. However, since there are fewer data in autumn due to lesser weather conditions, the seasonal evolution of the positional data could also be less recognisable (for this dataset of only four years).
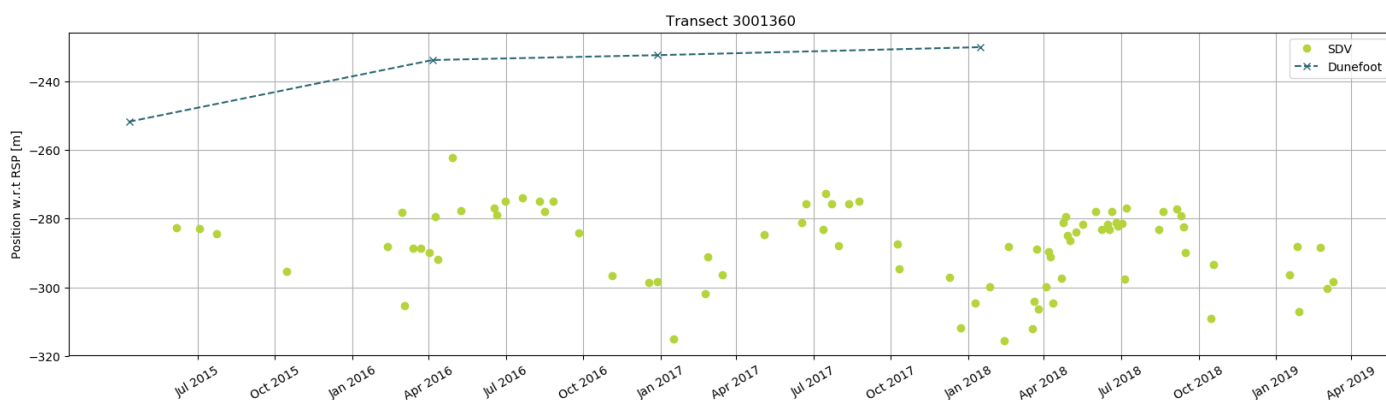
Figure 39. Time series of SDV and Dunefoot positions with respect to RSP on Transect 1360. The SDV data is derived from individual Sentinel-2 images between 01-07-2015 and 11-04-2019. The Dunefoot data comes from the JARKUS surveys of 2015 to 2018.
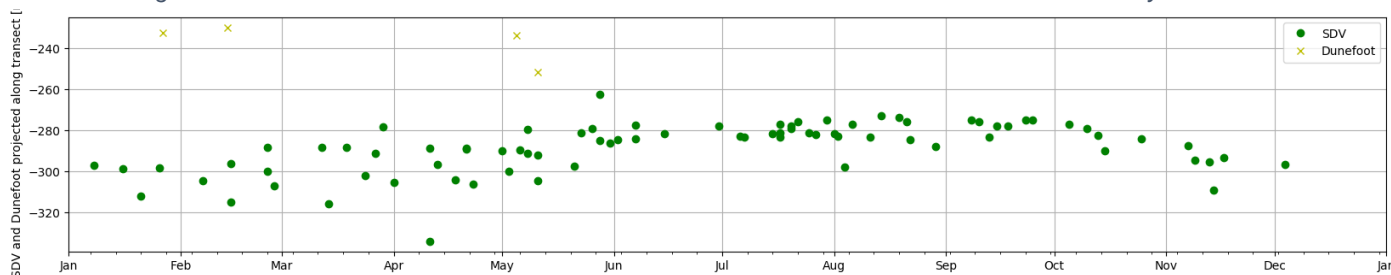
Figure 38. SDV and Dunefoot positions relative to RSP accumulated over one year for Transect 1360 to emphasize seasonal variation. The SDV data is derived from individual Sentinel-2 images between 01-07-2015 and 11-04-2019. The Dunefoot data comes from the JARKUS surveys of 2015 to 2018

4.2.2 Analysis of SDS detection and comparison with MLW and MHW positions

This subsection elaborates on the detection of the SDS from individual Sentinel-2 images and compares it with MLW and MHW data. Figure 40 and Figure 41 show the temporal means and standard deviations per transect of the offsets between the SDS and MLW (panel a) and between the SDS and MHW (panel b). The green lines depict the longshore averages of the temporal means and standard deviations for the total reach. Looking at the longshore averages of the SDS-MLW offset, we find a mean offset and standard deviation of 145 ± 71 m for the total reach, 236 ± 104 m for the dynamic area and 120 ± 61 m for the uniform area. For the SDS-MHW offset data, we find a longshore average of the temporal mean offset and standard deviation of -37 ± 60 m for the total reach, -36 ± 72 m for the dynamic area and -37 ± 56 m for the uniform area. As with the composite images, we see that the offsets between SDS and MHW are significantly smaller than those between SDS and MLW. Furthermore, we see that the SDS is, on average, located seaward of the MHW (negative offset) and landward of the MLW (positive offset); hence, the SDS lies between MLW and MHW. The standard deviations for both offsets are in the same order size, 71m versus 60m, and relatively large compared to the pixel resolution (10m). Since we look at individual images, we mainly relate those relatively large standard deviations to the hydrodynamic (e.g., mainly tidal) conditions, varying per satellite image.
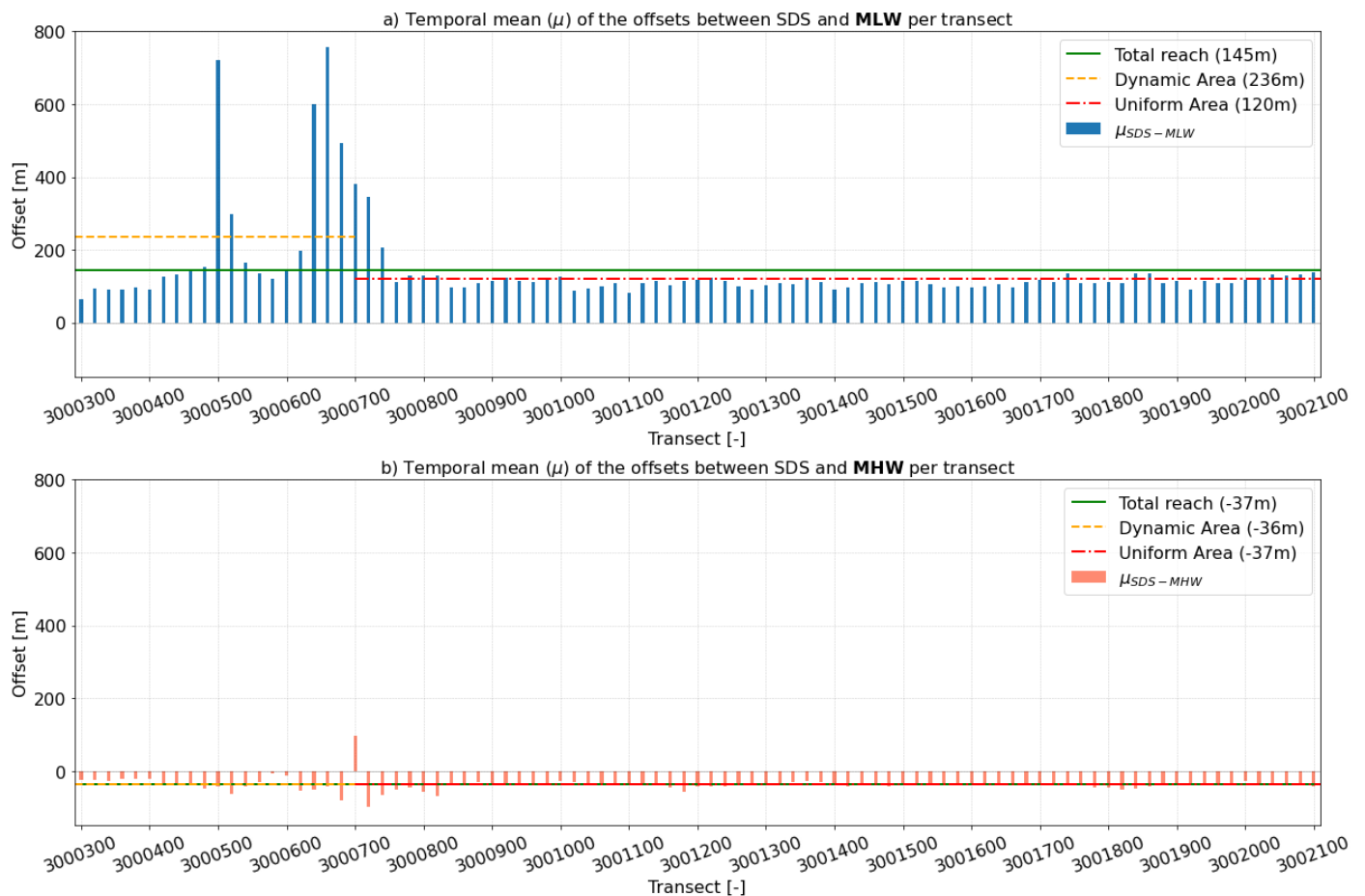
Figure 40 The blue bars in panel a) show the temporal mean of the offset between the SDS and MLW positions, per transect. The orange bars in panel b) show the temporal mean of the offset between the SDS and MHW positions, per transect. The green line shows the longshore average of the temporal means for the total reach. Derived from the dataset of individual Sentinel-2 images between July 2015 and April 2019.
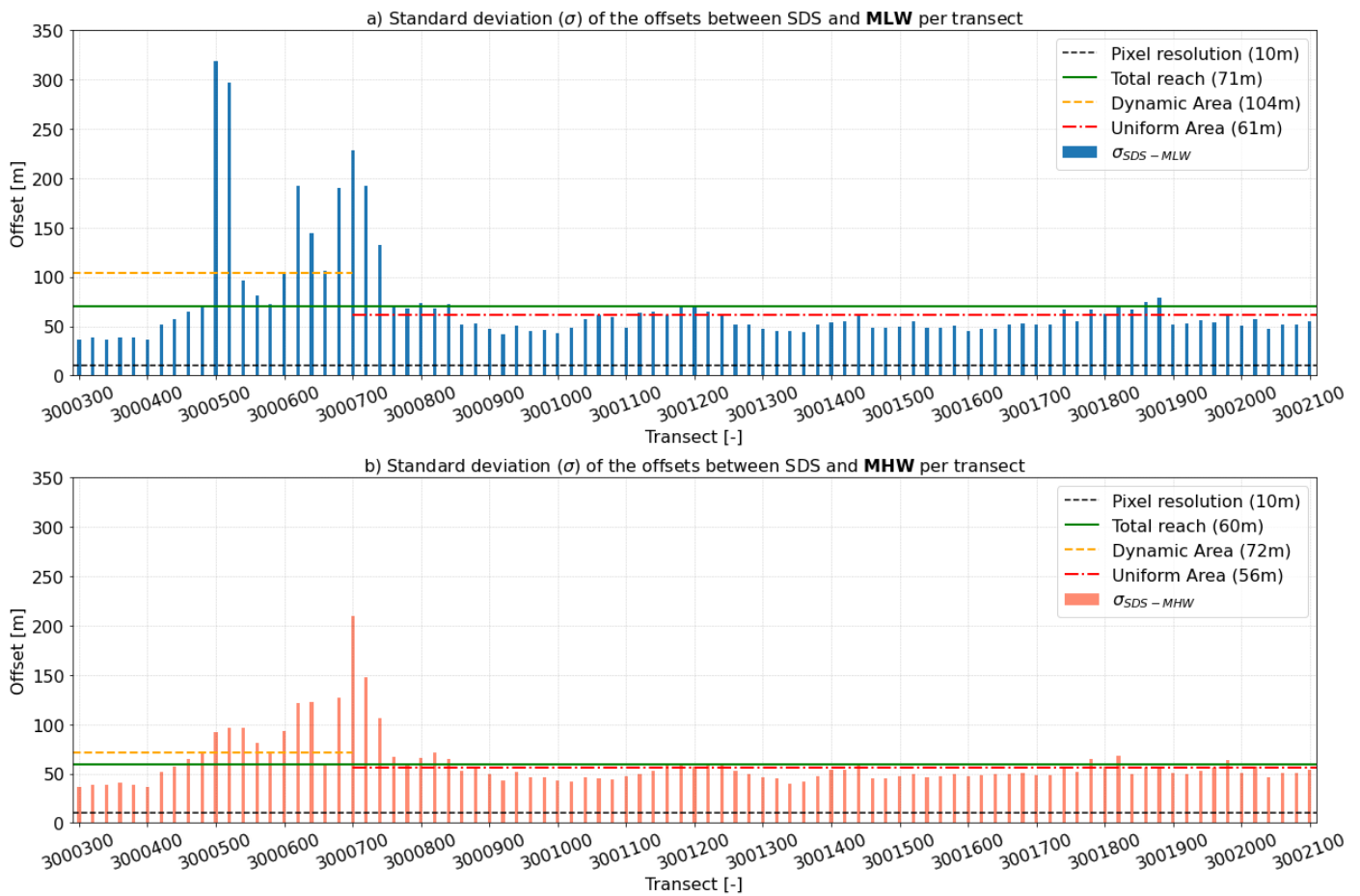
Figure 41 The blue bars in panel a) show the standard deviation of the offset between the SDS and MLW positions, per transect. The orange bars in panel b) show the standard deviation of the offset between the SDS and MHW positions, per transect. The green line shows the longshore average of the temporal means for the total reach. Derived from the dataset of individual Sentinel-2 images between July 2015 and April 2019.

The three panels in Figure 42 show the average position per transect of the SDS derived within a 360-day window (±180 days) around the JARKUS survey dates of 2016, 2017 and 2018, accompanied by the MLW and MHW of the corresponding survey dataset. The turquoise envelope represents the SDS spreading, equal to two standard deviations (2σ) seaward and landward of the temporal mean SDS position. We observe that the mean SDS position, together with the ±2σ bandwidth, is located between MLW and MHW for most transects and, in that sense, gives a fair representation of the intertidal area (e.g., the Wet Beach Width). We see that the SDS line follows the contours of the MLW and especially the MHW quite sharply. Thus, looking at the annual data collections, we find the SDS biased towards MHW with a spread of the SDS position representative of the intertidal area.
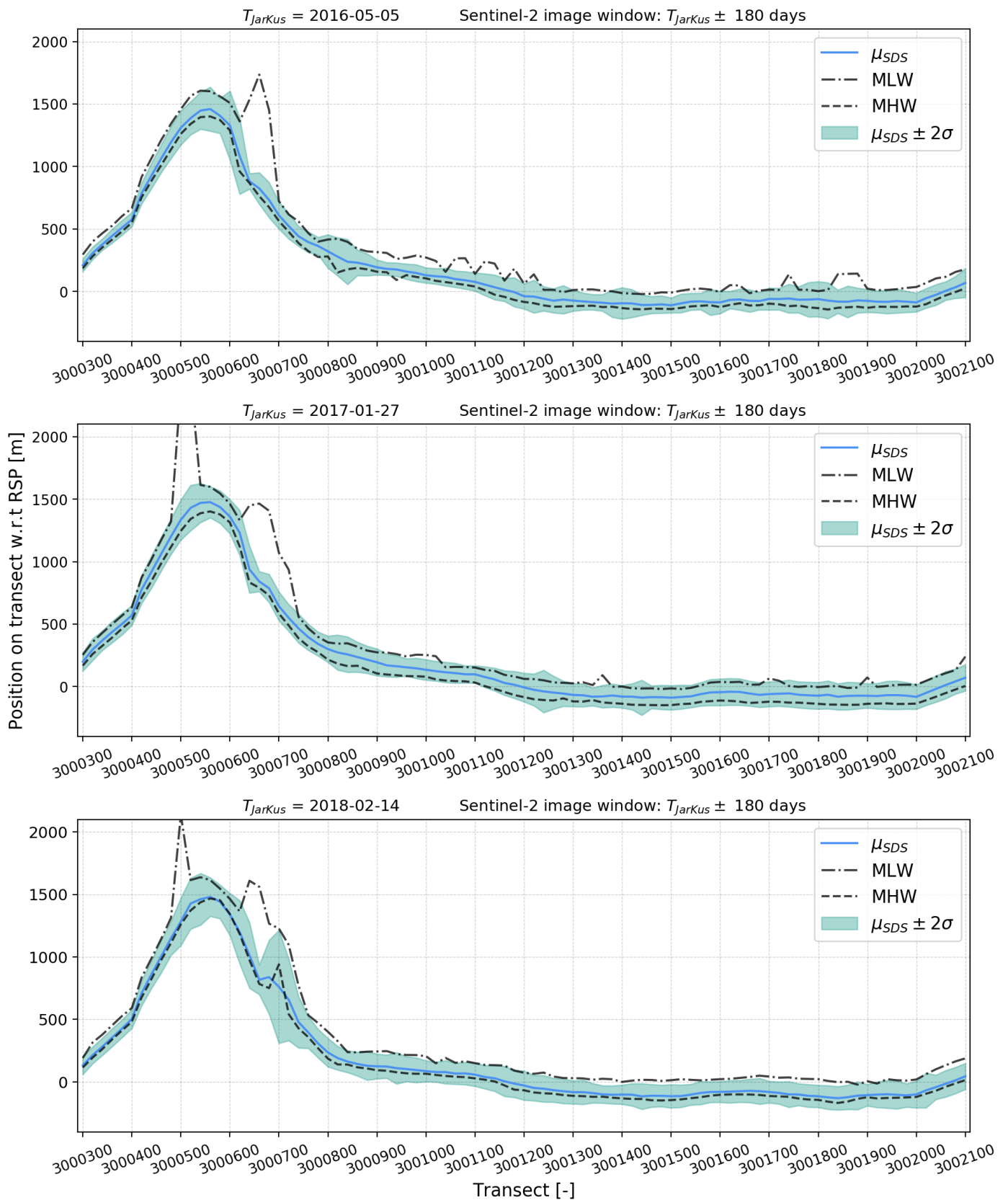
Figure 42 In each graph the blue line represents the average SDS position per transect derived from all individual Sentinel-2 images found within a window of 180 days before and after the JARKUS surveys of 2016, 2017 and 2018. The turquoise area shows the bandwidth of two standard deviations of the SDS positional data w.r.t to the average SDS position, corresponding to approximately 95% of the positional SDS data. The SDS data is plotted against the Mean-Low Water (MLW) line (dash-dotted) and the Mean-High Water (MHW) line (dashed) from the JARKUS measurement surveys.

4.2.3 Analysis of SDBW size and dynamics and comparison with JARKUS beach widths

Now that we know what the SDV and SDS detected from individual Sentinel-2 images represent in terms of position and trends, we will look at the derivation of the two parameters, the size and trends of the SDBW.

SDBW size compared to JARKUS beach widths

Figure 43 shows the temporal means per transect of the difference between the SDBW and Total Beach Width (panel a) and between the SDBW and Dry Beach Width (panel b). Note: a positive (negative) value equals an SDBW larger (smaller) than the Total or Dry Beach Width. The figure depicts the longshore averages of the temporal means for the total reach, the dynamic and the uniform area. The differences between the SDBW and Total Beach Width and between the SDBW and Dry Beach Width are -106m versus -76m for the total reach. The graphs do not show such an evident similarity of the SDBW to one of the JARKUS beach widths as for the SDBW from composite images. The SDBW size is, on average, somewhere between the sizes of the Dry and Total Beach Width.
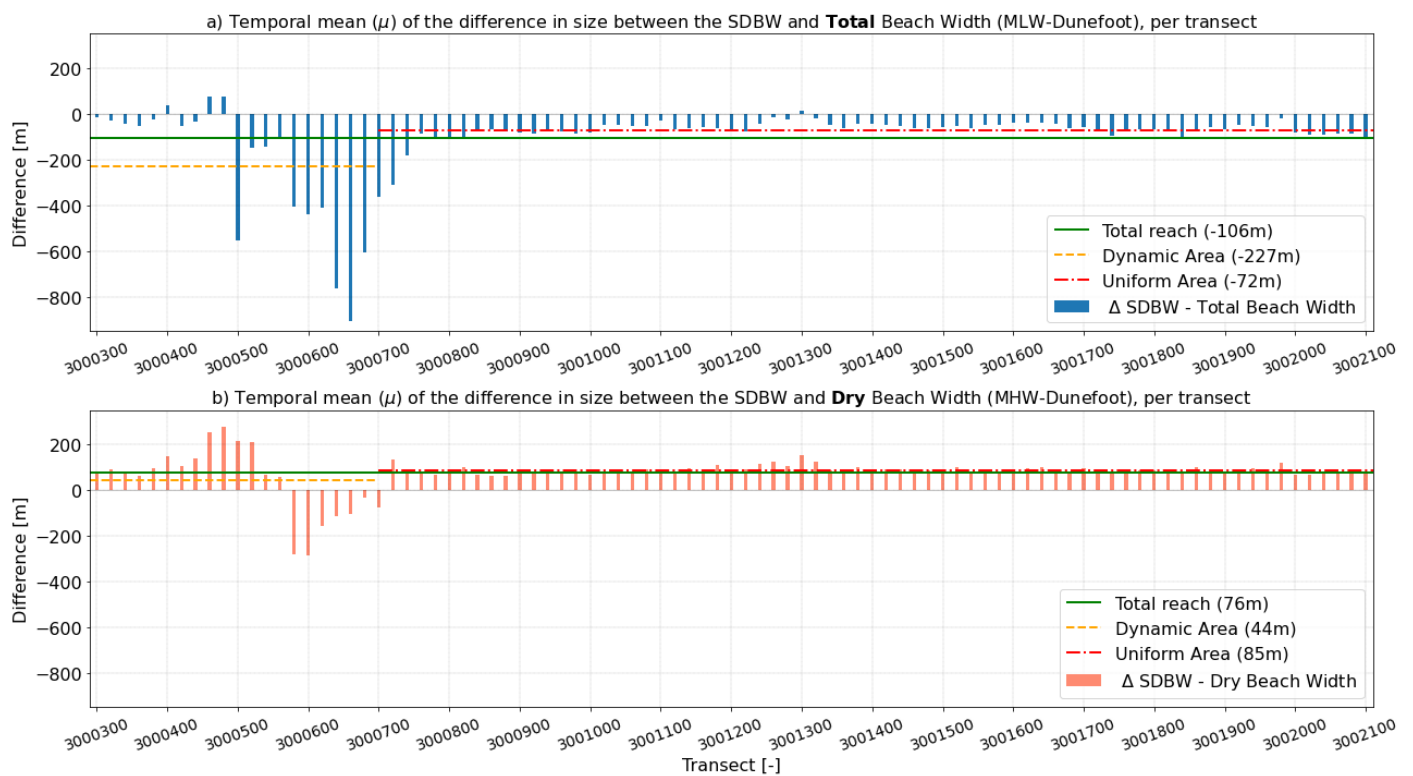
Figure 43 The panels in this figure show the temporal means of the difference between the size of the SDBW and Total Beach Width (blue bars in panel a)), and the size of the SDBW and Dry Beach Width (orange bars in panel b)), per transect. The green line shows the longshore average of the temporal means for the total reach, the yellow dashed line for the dynamic area and the red dash-dotted line for the uniform area. Derived from the dataset of individual Sentinel-2 images between July 2015 and 2019.

SDBW dynamics compared to JARKUS beach widths

Figure 44 displays the short-/middle-term trends of the SDBW and JARKUS data between 2015 and 2019. Important note: the JARKUS trends are derived from (only) four surveys between 2015 and 2018. The three panels display the trends [m/y] of the SDV with Dunefoot, SDS with MHW and SDBW with the Dry beach widths. In this figure, the MLW and Total Beach Width trends are left out of the graphs since they were statistically insignificant and of such a large magnitude (±300 m/y) so that the other parameters' trends were hardly visible due to the vast difference in scale. Leaving out the MLW and Total Beach Width is a minor issue for analysing the trends from individual Sentinel-2 images, whereas the SDS and SDBW trends show significantly more resemblance to the MHW and Dry Beach Width trends. The lower two panels of the figure clearly show the resemblance in direction and magnitude between the SDS and MHW trends and the SDBW and Dry Beach Width trends. Another thing to note is the enormous magnitude of the shoreline and beach width trends relative to the 34-year trends that we derived in Section 4.1. About the upper panel with the SDV

and Dunefoot trends, we note that the beforementioned embryo dune development explains the significant Dunefoot trends between transects 420 to 520. Furthermore, the SDV and Dunefoot trends along the uniform area are in opposite directions but of similar magnitude. The following paragraph gives a possible explanation for the latter observation.
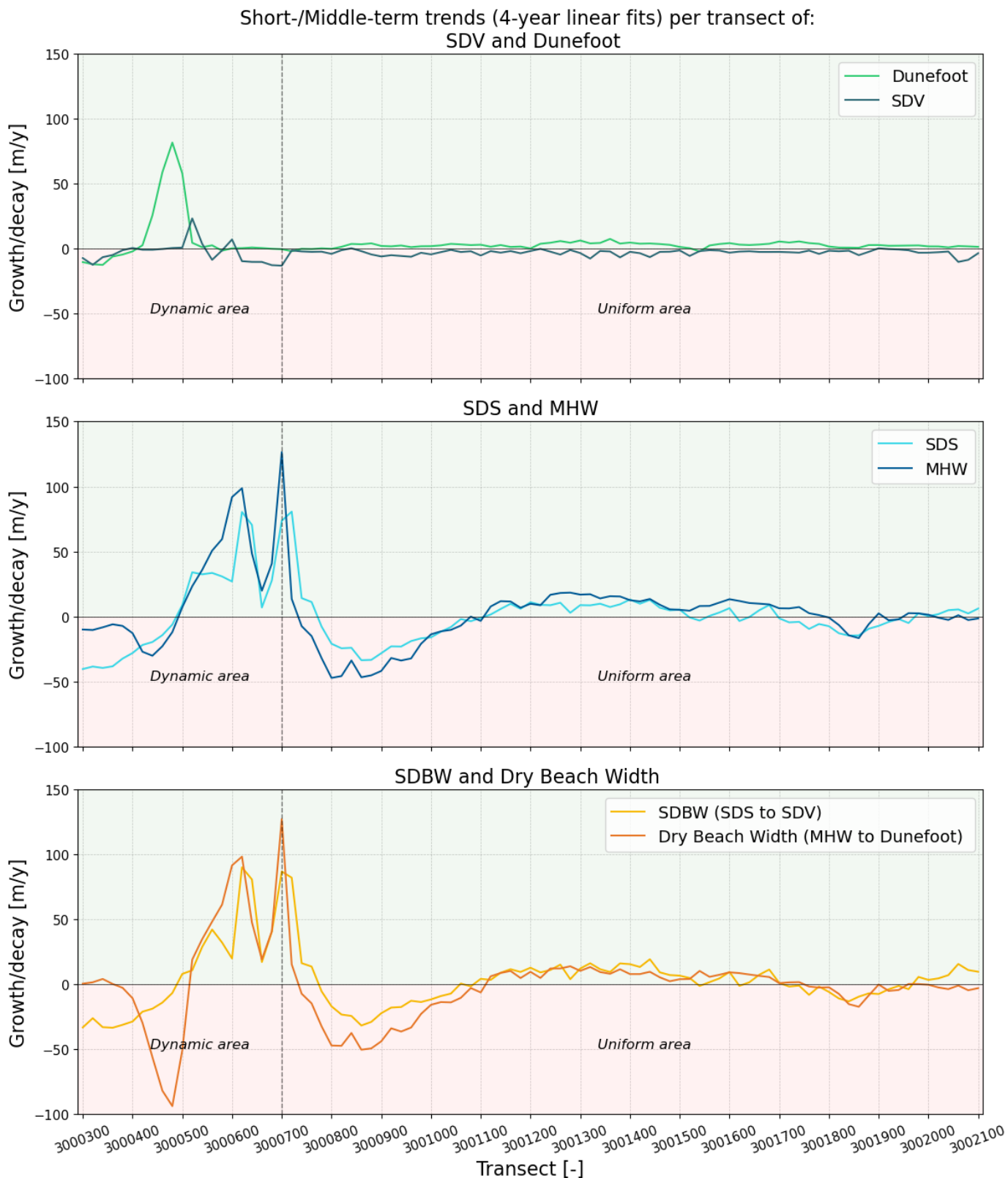
Figure 44 Short-/Middle-term trends (4-year linear fits) per transect of the SDV and Dunefoot (panel a), SDS and MHW (panel b) and SDBW and Dry Beach Width (panel c). Derived from the datasets of individual Sentinel-2 images between July 2015 and May 2019 and 2015 to 2018 JARKUS surveys. Note: the MLW and Total Beach Width trends are left out of the figure because they were statistically not significant.

Single transect analysis of the development of the SDBW and subcomponents compared to JARKUS beach widths

As for the composites, it is again very insightful to look at the time series of every individual transect. Figure 45 displays the time series of Transect 1000 with the SDS, MLW, MHW, SDV and Dunefoot positions in the upper panel and the SDBW, Total and Dry beach width sizes in the lower panel. Again, the JARKUS parameters' annual data points are connected through lines to give a (fictive) impression of their intra-annual development. The time series shows how the SDS position varies approximately between the MLW and MHW positions (the intertidal area) and is slightly biased to the MHW. Also, we see how the SDV has an annual skewness, with a dominant most seaward position in summer. Foremost, the time series provides insight into the development of the shoreline and vegetation line beyond the date of the latest JARKUS survey (at the time of simulating the results in May 2019). For example, we observe signs of erosion for the SDS and SDV data after the 2018 JARKUS survey. The erosion of the SDS seems to follow a structural shoreline trend and the erosion of the SDV is likely related to a storm event in January 2019. The Dunefoot, however, shows a minor growing trend, which is the case for most transects along the uniform area. The latter explains why the SDV and Dunefoot trends are in opposite directions along the uniform area in Figure 44.
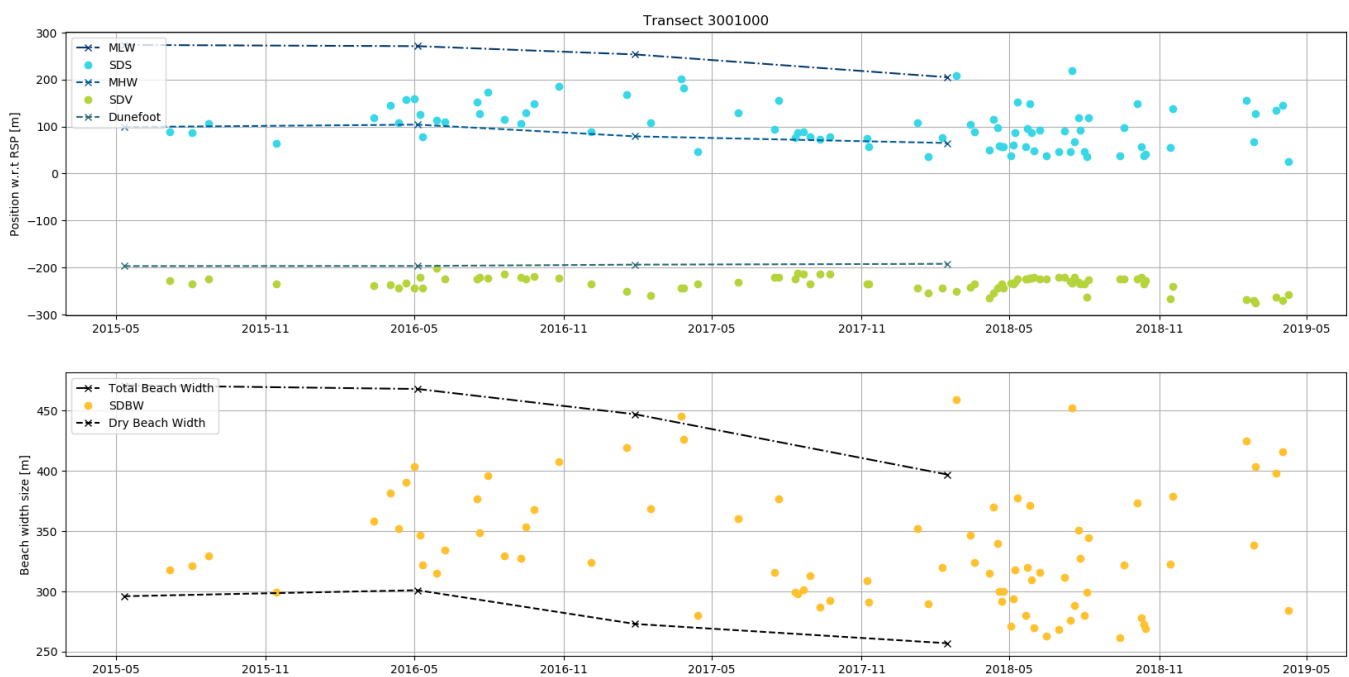
Figure 45 Time series of the positions of SDS, SDV, MLW, MHW and Dunefoot (upper panel) and the sizes of the SDBW, Dry Beach Width and Total Beach Width (lower panel) along Transect 1000. The SDS data is derived from individual Sentinel-2 images between 01-07-2015 and 11-04-2019. The MLW and MHW data is from the JARKUS surveys of 2015 to 2018.

4.3 Summarising remarks

The results in this chapter show that the SDBW, derived from the SDV and SDS, is a good proxy to measure beach width and beach width dynamics. We compared the SDBW with beach width data from JARKUS. We first looked at the SDBW detected from composite Landsat images (between 1984 and 2018) and then from individual Sentinel-2 images (between 2015 and 2019). We found that drivers of inaccuracy frequently hamper the quality of composite Landsat images and are not adequately filtered out by the composite technique. Therefore, we screened the individual Sentinel-2 images with mathematical algorithms to ensure that only proper images were used in the analyses from individual images.

The long-shore averages of the offsets (± standard deviations) between the SDV and Dunefoot, SDS and MLW/MHW, and differences between the SDBW and JARKUS beach widths are summarized in Table 6. The data of the different parameters are allocated according to the composite and individual image datasets and the different areas of the studied reach. Below, we elaborate on some highlights observed from Table 6 concerning differences found between the data from the different image types, the areas, and parameters. A table with an overview of the SDBW and JARKUS dynamics is not provided since long-shore averages of those parameters' dynamics (trends) are considered trivial.

Table 6 Overview of the longshore averages of the temporal mean offsets (including Standard Deviations (SD)) and temporal mean differences between the SDV, SDS & SDBW, and JARKUS data per transect averaged over the 91 transects of the Ameland study reach. A positive (negative) offset value corresponds to a landward (seaward) positioned SDS or SDV relative to the compared JARKUS parameter. A positive (negative) difference value corresponds to a larger (smaller) SDBW than the JARKUS Beach Widths. The standard deviations of the beach width differences are not included because they are deemed insignificant.

Dataset	Area	Offset (± SD) (m)			Difference (m)	
		SDV - Dunefoot	SDS - MLW	SDS - MHW	SDBW - Total BW	SDBW - Dry BW
Composite Landsat Images	*Total reach*	38 (± 50)	253 (± 165)	57 (± 132)	- 216	- 19
	Dynamic area	29 (± 114)	519 (± 446)	216 (± 345)	- 491	- 185
	Uniform area	40 (± 32)	178 (± 85)	12 (± 72)	- 138	28
Individual Sentinel-2 Images	*Total reach*	39 (± 24)	145 (± 71)	- 37 (± 60)	- 106	76
	Dynamic area	8 (± 52)	235 (± 104)	- 36 (± 72)	- 227	44
	Uniform area	48 (± 16)	120 (± 61)	- 37 (± 56)	- 72	85

Based on the initial analyses on the offset between the Dunefoot and SDV measured from composites (see Figure 23 and Figure 24), we determined the demarcation of two characteristic areas; the dynamic area between transects 300 to 700 and the uniform area between transects 700 to 2100. The SDBW detection method proved able to measure relatively subtle changes of the shoreline, vegetation line and beach width at the uniform area and highly dynamic changes of the same parameters at the dynamic area. However, at dynamic beaches, the beach width definition is less obvious and, thus, at the dynamic area, large offsets and differences were measured between the Satellite-Derived Parameters and JARKUS parameters. The latter is not necessarily related to the accuracy of the SDBW detection method.

Overall, we found that the SDBW size and dynamics are (much) more similar to the Dry Beach Width (MHW-Dunefoot) than to the Total Beach Width (MLW-Dunefoot). We relate this to the bias of the SDS towards MHW. From Table 6, one can read that the SDS position is, on average, located much closer to the MHW position than to the MLW position (see also Figure 30 and Figure 40). We assume this bias to be related to (a combination of) wave run-up, soil moisture on the beach and the local beach profile (slope). The SDS is, on average, located in the Tidal area (e.g., between MLW and MHW); hence, the SDS is mainly located landward of MLW and seaward of MHW.

The offset between the SDV and Dunefoot influences the difference between the SDBW and the two JARKUS beach widths equally since the Dunefoot is a common denominator being the landward boundary of both beach widths. At the transects where there exists a typical beach dune profile (the uniform area), there is a consistent offset of around 40-50 meters between the SDV and Dunefoot, with the SDV located landward of the Dunefoot. The SDV position varies with the annual seasons (Δ = 23m at the uniform area) and has a most seaward (and truest) position in summer. Substantial positive and negative offsets were measured at the dynamic area between the SDV and Dunefoot (see Figure 23 and Figure 36). These large values vary between -100 and +100 meters for the composites and -300 and +200 meters for the individual image. The longshore averages in Table 6 (29m and 8m) give a slightly distorted image of the actual situation since they average out the large opposite offset values. The large offsets are related to the formation of a saltmarsh called "Het Groene strand" in 2000 and the establishment of embryo dunes next to the saltmarsh a few years later. For which we saw delays between the seaward development of the SDV and Dunefoot at both locations, and hence the large offsets.

The measured trends of the SDV and Dunefoot are similar in size and direction along the uniform area. Along the dynamic area, they are less similar. There, the SDV and Dunefoot alternatively act as a predictor for each other. E.g., at some locations, the most seaward vegetation limit (measured by the SDV) significantly expanded in seaward direction several years before the position of the +3m elevation contour (the Dunefoot) caught up with this seaward shift, and vice versa. The latter is related to the saltmarsh development mentioned above.

The SDS, MLW and MHW trends have similar directions (e.g., growth or decay) along the whole study reach. The SDS trends are most similar to the MHW trends (see Figure 32 and Figure 44). The trend magnitudes deviate significantly along the western transects but gradually become more similar towards the transects on the east. As for the shoreline parameters, the SDBW trend directions are similar to those of the JARKUS beach widths' trends. Also, the magnitudes of the SDBW and JARKUS beach widths' trends are less similar along the dynamic area but gradually become more similar towards the transects on the east. The size but mainly the dynamics of the beach widths are predominantly determined by the (developments of the) positions and trends of the shoreline parameters because (in this case study) the shorelines are generally more dynamic parameters than the SDV and Dunefoot.

Analysis of single transects' time-series provides valuable insight on developments of coastal parameters locally. Regarding data of recent satellite images, the positional data (and derived trends) of the SDS and SDV present insight into developments of the shoreline and vegetation line months in advance compared to the latest JARKUS measurement survey.

Comparing the results from the composite Landsat images and individual Sentinel-2 images
When comparing the data from the Landsat composites with the Sentinel-2 individual images, we see that the more refined pixel resolution of Sentinel-2 (10m compared to Landsat's 30m) results in smaller standard deviations of the offsets, but not in smaller offsets. We found that the measured offsets are primarily related to actual physical offsets between the parameters regardless of accuracy. Irrespective of the actual change of the parameters' positions, the detection of the SDPs is influenced by several variable natural processes, such as seasonal variation of the vegetation greenness, tidal variation, and hydrodynamics.

At the dynamic area, the SDS-MHW and (especially) SDS-MLW offsets are much larger for composites than for individual images. This is because the studied period for the composite images (1984-2018) is different (and longer) than for the individual images (2015-2019). During the period used for the composite Landsat images, significant morphodynamics occurred at the dynamic area caused by the landing of the offshore sandbank Bornrif between 1980 and 1985 and its subsequent eastward spreading in the years after. Resulting in very large offsets between the SDS, MLW and MHW, sometimes up to and over 1000 meters, related to differences in definition/measurement of the SDS and MLW/MHW. The analysis of the individual image data

shows that the offsets between SDS and MLW and (especially) between SDS and MHW become much more stable and uniform for the whole reach (see Figure 40 and Figure 41) when most significant dynamics related to the Bornrif landing have long passed.

The longshore averages of the SDS-MHW offsets are positive for the composite images (57, 216 and 12m) and negative for the individual images (-37, -36, and -37m). For the longshore averages of the composite images, this is a somewhat distorted image of the actual situation, which is related to the demarcation of the dynamic and uniform areas. Looking at Figure 30 and the longshore averages of the SDS-MLW and SDS-MHW offsets for the composites, one could argue that a different definition of the dynamic and uniform area (with the border at transect 900, for example) would have been more appropriate to represent the longshore averages of both the SDS and SDV for the two characteristic areas. As you can see in Figure 29, the SDS-MHW offsets for transects 900 to 2100 are negative, indicating an SDS positioned seaward relative to MHW, more in line with the overall SDS-MHW offsets for the individual images, see Figure 40.

The SDV-Dunefoot offset is higher at the uniform area for the individual images (48m) than the composite images (40m), where one might expect differently because of the more refined pixel resolution of Sentinel-2 images compared to Landsat images. This is most likely explained by the dunefoot and vegetation line simply lying further apart physically in the period 2015-2019 compared to the period 1984-2019. Alternatively, it might be related to the less refined pixel resolution and lesser quality of the Landsat images (caused by, for example, satellite sensor errors that do not occur as frequently for the Sentinel-2 images), resulting in less accurate SDV positions and offset values. The standard deviations found for the individual images are about half the size of the standard deviations found for the composite images, indicating the higher accuracy of the Sentinel-2 images compared to the Landsat images.

5 Discussion

This chapter discusses the results and insights obtained from this study. The results demonstrate that the Satellite-Derived Beach Width, defined as the cross-shore distance between the Satellite-Derived Shoreline and Satellite-Derived Vegetation line positions, is a suitable option for beach width detection from optical satellite imagery. This study showed that the SDBW can be used to analyse the beach width dynamics on different time scales: interannual (longer term) and intra-annual (seasonal or short-term) trends. We sometimes refer to the separate parameters comprehensively as the Satellite-Derived Parameters (SDPs).

The discussion is subdivided into three parts. First, in Section 5.1, the applicability and future potential of the SDBW are discussed. Subsequently, considerations and limitations of the method are discussed in Section 5.2 and Section 5.3.

5.1 Applicability and future potential of the SDBW method

This section discusses the applicability and future potential of the SDBW method. In potential, the SDBW provides insight into (the development of) positional data and dynamics of the beach width, shoreline, and vegetation line with *one press of the button* at any location in the world where there is a sandy beach with vegetated dunes. The SDBW method can provide a valuable first impression of the state of a coast (regarding coastal safety, recreational potential, and ecosystem services) at sandy beaches worldwide, which can prove especially valuable where there are little to no data available.

5.1.1 Worldwide applicability for SDBW detection

This study analysed the beach width by assessing the dynamics of the sandy shoreline and the vegetation line. The results show that (semi-)automated detection methods based on optical satellite imagery are promising for sandy beaches with vegetated dunes, such as a large part of the Dutch coast. Similar environments can also be found in Australia, Canada, France, and so forth (Montaño et al., 2021; Moulton et al., 2021; Walker et al., 2017).

In sandy beach environments without vegetated dunes, the SDV cannot be used as the landward boundary. Still, our method may be useful if the landward boundary is determined by a fixed line, such as buildings or (road) infrastructure. In those cases, the beach width dynamics are solely determined by the shoreline dynamics. Alternatively, the SDV can also be used as an alternative to the SDS at beaches where the vegetation line is used as a shoreline indicator (Boak & Turner, 2005).

In their aim to classify the world's sandy coasts by applying pixel-based supervised classification of optical satellite imagery, Luijendijk et al. (2018) conclude that 31% of all ice-free shorelines worldwide are sandy (including gravel beaches). Hence, depending on the type of landward boundary, the SDBW method can potentially be applied to up to 31% of the world's ice-free shorelines.

In her research on classifying the world's muddy coasts, Hulskamp (2021) states with an 85% certainty that 12% of the world's coasts are muddy. In muddy environments, the SDBW method is, however, less suitable since most muddy coasts do not have typical beach widths as defined in this research, and detecting shoreline and shoreline dynamics from muddy coasts can be complex due to large horizontal tidal excursions and high water content (Luijendijk et al., 2018). Then again, in the muddy environments where it is impossible to extract a sandy shoreline, the local shoreline is likely represented by the most seaward vegetation contour. Hence, the SDV could be used there as a stand-alone metric for the shoreline. For example, in their study on the coastal evolution of a muddy coast in French Guiana, Orseau et al. (2020) extracted the shoreline from satellite images, processed with a soil-adjusted vegetation index, as the delineation between water and mangrove areas.

5.1.2 Measuring coastal dynamics at data-scarce environments or with higher spatiotemporal resolutions than existing measurement campaigns

The SDBW method enables the measurement of coastal dynamics at data-scarce environments and provides additional measurement data in a spatial and temporal sense compared to existing in-situ measurement data collections limited by spatiotemporal confinements.

For example, the most acute effects of nourishments on the beach occur in the first six months after implementation (de Schipper et al., 2016). In theory, from publicly available satellite imagery, the SDBW method is able to measure those effects on a temporal scale of 5 to 16 days and a spatial scale of 10 to 30 meters in cross-shore and alongshore directions. Most existing in-situ measurement campaigns are unable to measure those nourishment effects due to their temporal constraints. The JARKUS measurement survey, for example, is only measured annually. Furthermore, not to forget the vast majority of coastal zones where no measurement campaigns are carried out at all.

5.1.3 Emerging optical satellites and remote sensing techniques

The database of satellite images currently available to the public is ever-expanding and increasing the amount of coastal measurement data by the day. Currently, the highest spatial and temporal resolution of the publicly available satellite images is limited to ESA's Sentinel-2 10-meter pixel resolution and 5-day return period. The range of spatial and temporal resolution of advanced commercial satellites varies from 10 to 0,31-meter pixel resolutions and from 6 days to sub-daily return periods (Turner et al., 2021). It is a matter of time before satellites are launched that provide publicly available images with similar pixel resolutions and return periods. These improvements would not only enhance the spatiotemporal resolution of the measurement data but also provide additional measurement techniques.

One of those techniques is the creation of high-resolution Digital Elevation Models (DEM) based on stereoscopic images created by combining two (high spatiotemporal resolution) optical satellite images that cover the same (coastal) area with a different angle and a short-time-interval between both consecutive images (Almeida et al., 2019; Bergsma et al., 2021). Another technique is the creation of detailed near-shore bathymetry derived from waves that are measured from sequences of 12 high-resolution satellite images with 0,5-meter resolution and taken 8 seconds apart (Almar et al., 2019). Turner et al. (2021) even demonstrate the combination of the two abovementioned measurement techniques by generating a highly detailed topo-bathymetry derived for the Collaroy-Narrabeen beach in Australia from tri-stereo high-resolution optical satellite imagery.

5.1.4 Constantly developing and increasing numbers of image processing and feature detection algorithms

As we will discuss in Section 5.2, several limitations of the SDBW method hamper the detection process. New and improved algorithms could potentially mitigate the influence of some of those limitations. The review of potentially beneficial algorithms is outside the scope of this research, but exciting developments take place in neighbouring fields.

5.2 Limitations of the SDBW detection method and analyses in this research

This section discusses four key limitations of the SDBW detection method or of this research.

5.2.1 Lack of extensive SDV validation

One limitation of this research is the absence of a thorough validation of the method to derive the SDV, since we lacked sufficient validation data for different environments. The accuracy of the method to derive the SDS was assessed by García-Rubio et al. (2015), Hagenaars et al. (2018) and Luijendijk et al. (2018). Since the case study of Ameland has similar geographic characteristics compared to the case studies in these studies, we are confident about the validity and accuracy of the detected SDS in this research as well.

The SDV, however, is a newly introduced parameter and, although there are similarities in the detection method, the detection of the SDV is subject to different sensitivities than the SDS. Hence, the accuracy of the

SDS cannot be adopted blindly for the SDV. The data of Keijsers et al. (2015) on vegetation cover along Ameland's northern coast facilitated a first glance on the performance of the SDV detection, but the dataset was not extensive enough to make an elaborate validation (see Appendix C). Extensive accuracy assessments of the SDV with detailed in-situ vegetation data would support the validity of the SDV detection and, thus, of the SDBW method.

5.2.2 Limitations regarding NDVI threshold selection in the context of SDV detection

This research found that a supervised NDVI threshold value of 0.15 resulted in more realistic SDVs than the automated threshold selection. To detect the SDS, we used Otsu's method for automated threshold selection for separating land and water pixels in the NDWI histogram. However, for detecting the SDV, Otsu's method did not work as well for automatically selecting a threshold to separate sand from vegetation pixels in the NDVI histogram. The latter has to do with the fact that for Otsu's method to work correctly, the area of interest (e.g., a polygon of the studied coastal zone) needs to be selected in such a way that the image has an approximately equal share of pixels of two contrasting land cover types (e.g., land and water, or sand and vegetation). In the SDBW detection method, first, the SDS is derived, hence, an area of interest is selected with approximately equal parts of land and water pixels. The latter is shown in Figure 16 and Figure 17. Then, after the water pixels are masked from the original image, the SDV is derived from the contour between sand and vegetation areas of the remaining land pixels. However, in many cases (e.g., that of the Ameland case study), the share of the sand and vegetation pixels of those remaining land pixels is not equally divided. Typically, the remaining land pixels contain much more vegetation than sand pixels; this can also be seen in Figure 16. The threshold computed with Otsu's method is therefore inconveniently biased towards the vegetation pixel mass, resulting in an SDV located land-inward with respect to the actual vegetation line (see the green vector in Figure 52).

The supervised NDVI threshold value determined in this research is applicable to Ameland and likely to beaches with similar geographic characteristics. We expect that other threshold values will be more suitable for separating the sand (or sediment) and vegetation pixels at locations with different sediment and vegetation characteristics. In order to optimize the SDV detection process and prevent having to determine new supervised NDVI threshold values for every other studied coastal zone, an automated threshold selection method is preferable for separating the sand and vegetation pixels.

When looking at the NDWI histogram in Figure 16, one can imagine the potential significance of an automated *multi*-threshold selection algorithm that can adequately separate the three distinguishable pixel masses, representing water, sand, and vegetation. The implementation of such an algorithm could benefit the optimization of the detection process.

5.2.3 Composite images including corrupted images for sequences of composites

Based on the research of Donchyts et al. (2016) and Hagenaars et al. (2018), which showed promising results for the use of composite satellite images for the study of (long-term) shoreline dynamics, we started the analyses of the SDBW method with composite images (see Section 4.1). We experienced a significant flaw in the composite image technique when using the 34-year dataset of Landsat 5 and Landsat 8 images available above the Ameland area. Composite satellite images frequently included at least one image that had a certain amount of (undetected) cloud cover or was corrupted by satellite-instrument errors, reducing the quality of a sequence of composite images that all included that particular false image and were, therefore (partially) unusable (see Figure 46). These errors frequently hampered the quality of the measurement data. If the images used for composites are screened and filtered before composition, this would prevent the significant quality loss of these sequences of composite images and improve the measurement data.
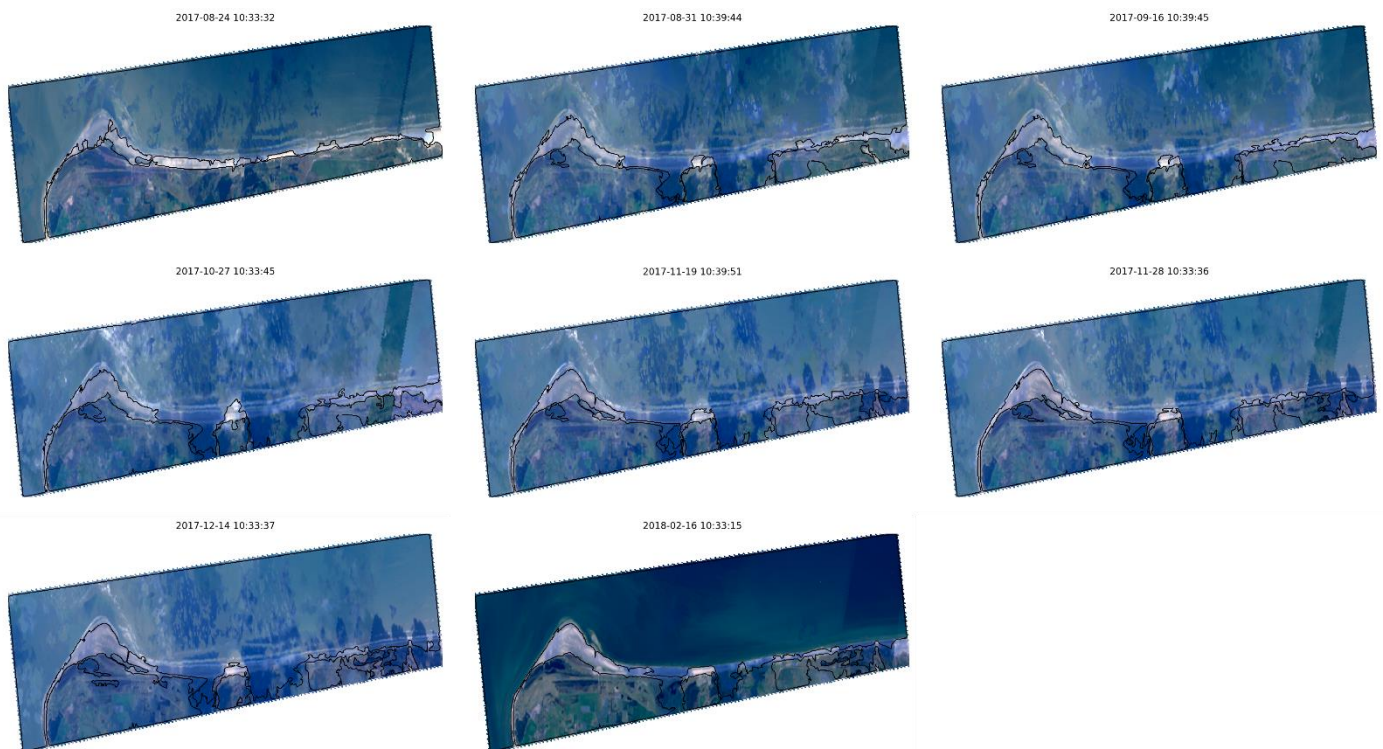
Figure 46 Sequence of eight composite Landsat 8 images extracted between 2017-08-24 and 2018-02-16 with possibly one singular image with cloud cover adversely influencing the quality of the other seven composite images.

5.2.4 Quality control of satellite images

In the previous subsection, it was mentioned that cloud cover strongly influences the usability of satellite images for detecting the SDS and SDV. In this research, two image filtering methods were applied to filter images from the individual image dataset of which the quality was too badly influenced by cloud cover or other drivers of inaccuracy.

When extracting satellite images from the Google Earth Engine™, a maximum cloud cover percentage can be selected for the images to extract. A studied area of interest is often smaller than the complete satellite image (part of the satellite "swath") to which the cloud cover percentage is assigned. Hence, an image can sometimes be assigned only 10% cloud cover percentage, but the cloud cover appears to be precisely above the area of interest. Alternatively, a satellite image can be assigned 90% cloud cover, but the area of interest lies precisely in the 10% cloud-free area. Therefore, when selecting a maximum cloud cover percentage of, say, 60% for your satellite images, useable images can be wrongfully omitted, and non-useable images can be wrongfully included.

In the analysis of the SDBW from individual images, we decided to use satellite images with up to a 100% cloud cover and screen them afterwards on usability with two algorithms based on image similarity (see Appendix B) to filter all images to ensure that we include all usable images and exclude all non-usable images. The image filtering starts with the selection of a clear cloud-free satellite image that is used as a baseline. Other satellite images are subsequently compared to this image through both similarity algorithms. When the differences exceed a certain threshold, the satellite images are removed from the analysis. This algorithm was applied to satellite images that were already fixed on the area of interest. Therefore, this algorithm did not suffer from the limitations described in the previous paragraph.

However, even with the application of these algorithms, useful data points can be excluded from the analysis since some parts of the omitted satellite images may not be entirely covered by clouds (or other drivers of inaccuracy). Figure 47 depicts an example of a satellite image that was excluded from the analysis after

applying the image similarity algorithms (with an SSIM score of 0.79 being smaller than the 0.80 threshold value). The cloud-covered area of this image is indeed not usable for analysis because they locally hamper a correct SDS and SDV detection. However, the majority of this image's SDS and SDV data could easily be included but was removed from the analysis.

2017-08-09 10:55:46

CC: 40,27%   SSIM: 0,79   Diff: 7,13%
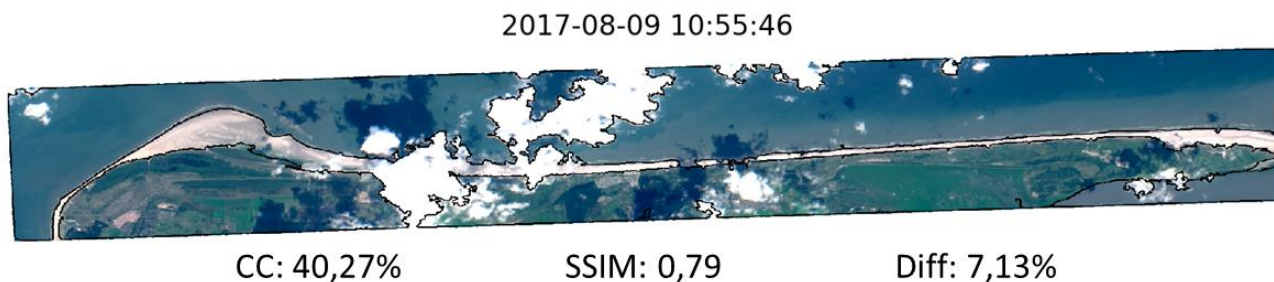
Figure 47 Sentinel-2 image of 2017-08-09 with a 40,27% Cloud Cover (in the Metadata) filtered from the analysis because SSIM score was below threshold value 0,80

A possible solution to the above-described limitations could be to apply a comparable quality screening per individual transect after the SDS and SDV vectors have been generated from a satellite image (individual or composite). For example, when part of the area of interest is covered with clouds but the rest is not, data points on those transects not covered by clouds can be included for further analyses.

This concept could lead one to think about optimizing the method used for selecting the correct positions from the SDS and SDV intersections along a transect. The selection method used in this research (also discussed in Section 5.3.3) makes use of certain thresholds to exclude unrealistic positions. Much thought was already put into configuring this method for selecting the right SDS and SDV positions. However, since the SDS and SDV data at Ameland sometimes showed large actual change values (of over 1000m), it appeared very difficult to configure thresholds to exclude faulty positions caused by clouds or other drivers of inaccuracy (that were located closer to the SDS or SDV than the selected threshold of 1500-2000m). We deem it worthwhile to look deeper into optimizing this selection method and investigate the possibilities of solving this complex issue.

In theory, with a transect quality screening method and an improved data selection method, part-faulty images would not need to be omitted when one can just use the SDS and SDV data overlying the transects in the non-spoiled areas.

5.3 Considerations of the SDBW detection method and analyses in this research

In this section, we discuss four key considerations about the outcome of this research and the SDBW detection method, which are important to note but are not considered limitations of this research nor the detection method.

5.3.1 Comparison of different physical parameters

The comparison of the SDBW to the JARKUS beach widths (Total and Dry Beach Width) is restricted to comparing the SDS to the MLW and MHW and the SDV to the Dunefoot, which represent different geophysical features. The satellite-derived features are based on optimal-discernible features, and the JARKUS features are elevation-based. Hence, although these comparisons provide valuable insight into the performance of the SDBW detection and the behaviour of the separate SDPs, they do not provide a detailed accuracy assessment of the SDBW data. In conclusion, it is important to note that offsets between the analysed parameters can be related to the actual physical distance between the compared parameters or the accuracy of the detection method. The physical differences make that the SDBW and JARKUS beach widths will deviate from each other regardless of the accuracy of the detection method.

The SDS is mostly located between MLW and MHW (e.g., within the intertidal area) and biased towards MHW. This bias of the SDS towards MHW is likely related to (a combination of) wave run-up, soil moisture of the beach and the local beach profile (slope).

Regardless of detection from individual or composite images, for the Ameland case study, we found an average offset of 40 to 50 meters between the SDV and the Dunefoot, with the SDV lying landward of the Dunefoot. The offset between the Dunefoot and SDV is expected to vary for other beaches with similar characteristics. Based on the offset data measured at the relatively static (*uniform*) part of the Ameland case study, we expect to see a higher correlation between the Dunefoot and SDV, and thus smaller offsets, at other sandy beach-dune systems in the Netherlands, most likely at the Holland Coast.

Regardless of the physical difference (and offset), the SDV and Dunefoot certainly show a degree of correspondence to each other, depending on the local geographic situation. We found the trends of the Dunefoot and SDV to be very similar at the uniform area, where we found slow but measurable changes in time. At the more dynamic area, the trends of the parameters were less similar but nevertheless showed a relationship in the sense that one parameter is "predicting" the future position of the other, and vice versa. Which is in line with the following relationship described in literature; the development of dunes (sedimentation) on a beach is, among others, controlled by vegetation on the beach; alternatively, vegetation may establish due to accumulating sediment (Keijsers et al., 2015).

5.3.2 Importance of independently studying SDS and SDV dynamics when analysing SDBW dynamics

The results of Chapter 4 showed that the measured SDS, SDV and SDBW give a sound impression of the dynamics of their respective physical parameters. The change of the SDS or SDV positions with respect to each other can vary significantly in magnitude and in a spatial and temporal sense. When studying the SDBW data, it is therefore always necessary to investigate the dynamics of its subcomponents. The signal of the SDBW can be dominated by the dynamics of either one of SDS or SDV. For example, at the western part of Ameland, the beach width dynamics were sometimes dominated by very large shoreline dynamics. If any interesting (small-scale) SDV dynamics had co-occurred, they would be difficult to remark when only looking at the SDBW.

Hence, apart from providing insight into the development of the SDBW, separate analyses of the SDS and SDV (as a proxy for the shoreline) can mutually reinforce each other and contribute to the understanding of sandy coasts, such as for example done by Pollard et al. (2020) who use five shoreline proxies to study spatiotemporal barrier island dynamics.

5.3.3 Multiple intersections (measurement data points) along transects

Multiple SDS or SDV vectors can be detected from satellite imagery, e.g., when a (temporarily submerged) sandbank or spit is located seaward of the shoreline or when a vegetated area (such as embryo dunes or other kinds of vegetation) is located seaward of the vegetation line (at the foredunes). When more than one vector intersects with a transect, only one position for either parameter is used as measurement data for that specific transect. The preference of selection is different for both parameters: for the SDS, the most landward intersection is selected, and for the SDV, the most seaward intersection is selected. These selection choices do not always result in the best option for the SDS or SDV but, based on the results, we believe that, on average, they provide the best representation of either parameter. We encountered several noteworthy circumstances that debate the selection choices, and there will likely exist more. For example, along the Ameland coast, a spit formed at the western island head in an eastward direction after the landing of the Bornrif sandbank (see, for instance, the 1995 and 2000 panels in Figure 13). Subsequently, the spit developed into an intertidal area and created a small "inland" lake. During these morphological processes, for each image instance, the most landward SDS intersection was selected as the measurement data for further analysis, which at some transects in the dynamic area diverged up to around a thousand meters from the MHW and MLW. One can strongly argue whether the selected SDS positions, in that case, are the right choice

under those circumstances. Then again, the relevance of the selected SDS intersection might also vary with the considered purpose of the beach width. In terms of coastal safety, when selecting the most seaward SDS intersection in case of a spit bordering the beach, the selected SDS might give the best representation of the beach its capacity to reduce wave impact, but it might give a less proper representation of the beach its recreational carrying capacity.

For the SDV, comparable circumstances can be present along a transect. When a beach width is large enough, embryo dunes can develop at a sizeable distance from the primary foredunes. Dependent on the density, and to a lesser extent the greenness, of this vegetated area, the detection method will detect an SDV intersection at the border of this area. This intersection is selected as the SDV measurement data since it lies most seaward at the local transects. In the case of the "Groene strand" at Ameland, a vegetated area (significant in size) even grew several hundred meters seaward of the primary dune's vegetation (and Dunefoot position), resulting in an SDV intersection at the border of this Groene strand. As is the case for the SDS, the relevance of the selected SDV varies for its purpose; the SDV positioned at the primary foredune (near the Dunefoot) might fit better as an indicator for coastal safety, whereas the SDV positioned at the seaward border of the external vegetated area might fit better as an indicator for the recreational capacity of the beach.

5.3.4 Deriving and analysing signals from optical satellite data
In this research, we analysed the dynamics of the studied coastal parameters by looking at trends in the data of the measured parameters. We computed these trends per transect by deriving linear fits from the parameters' positions measured in a certain period. We interpreted these linear fits as an indication of the dynamics of the parameters. The representation of the trend logically depends on the selected period of time. When selecting more extended periods, the chance increases that a trend break will be present in the data. For several transects along the Ameland coast, trend breaks were found in both SDS and SDV trend data (see Figure 29 and Figure 35), resulting in trend breaks in the SDBW data since the SDBW is a product of the two. Depending on the period selected for the trend derivation and the geographic circumstances of the location in question, the outcome of a computed trend can vary significantly for just one transect. For example, the landing of the Bornrif sandbank on the western island head results in accreting SDS trends for multiple transects in the area when using an extended period (30+ years) to compute the linear fit, whereas when computing a linear fit from the last ten years of data, the results show eroding SDS trends for (the majority of) those transects. The eroding SDS trends correspond to the erosion (or lateral spread) of the previously landed sandbank. Hence, when analysing trends derived from the SDS, SDV or SDBW, attention should be paid to the development of the parameter's data points in space and time for the considered trend period to see whether trend breaks occur for the studied parameter during that period. This extra step in the data analysis is necessary for correct interpretation of the dynamics and might lead to selecting different periods from which the trends are computed.

A simple regression line equation was used as a default to determine the SDBW dynamics/trends. The use of, for example, the Weighted Regression Line (WRL) or another more advanced technology might improve the accuracy or value of derived trends.

6 Conclusions and recommendations

This research investigated the possibilities of deriving beach width dynamics from optical satellite imagery in a semi-automated way and compared the results to existing in-situ measurement data. This chapter presents the conclusions of the research results and provides recommendations for optimising the detection method and suggestions for future research.

6.1 Conclusions

The beach width is used to quantify the capacity of a beach section to provide for safety, recreation, and ecology. Using optical satellite imagery to derive the beach width has potential added value in terms of lower costs and increased temporal and spatial resolution of measurements compared to traditional in-situ survey methods. The main goal of this study was to examine the possibilities of detecting beach width from optical satellite imagery to expand the existing (in-situ) options for measuring beach width and beach width dynamics. We explored these possibilities by analysing the case study of Ameland in the Netherlands. This is a dynamic beach for which a substantial amount of in-situ beach profile measurements (i.e., JARKUS) are available to verify the method presented in this research.

We form the conclusions of this thesis by answering the main research question:

How can beach width (dynamics) be derived from optical satellite imagery along sandy coasts, and how do the results contribute to the current options for measuring and analysing beach width (dynamics)?

The answer to the main research question is formed by answering the sub-questions below.

1. What are commonly used definitions for the beach width, and which are suitable for detection from optical satellite imagery?

In its simplest form, a beach width is defined as the cross-shore distance between the beach's seaward and landward border. Along sandy coasts, the seaward border can be a type of shoreline determined as a certain water level (e.g., MLW, MSL or MHW) intersecting with the cross-shore elevation profile of the beach or an optically discernible shoreline. The landward border can consist of (vegetated) dunes or man-made structures, such as built environment or dikes and revetments. In this study, we consider beaches that are bordered by vegetated dunes. This border is commonly defined as the dune foot, of which the physical definition is the break in slope between the relatively flat beach and the steep foredunes. In the Netherlands, this parameter is considered to be located at the most seaward crossing of the NAP +3m elevation contour with the cross-shore beach profile, which we refer to as the Dunefoot in this report. An alternative measure for the landward border is the optically discernible vegetation line, defined as the most seaward contour of dune vegetation. Hence, several methods exist to measure beach widths and their subcomponents based on different measurement techniques (i.e., elevation-based or optically discernible features), and thus beach widths derived with different measurement methods will likely have different physical dimensions.

To detect the beach width's subcomponents from optical satellite imagery, we use Normalized Difference Indices, and therefore we look at strongly contrasting land cover types that are optically discernible. Hence, we looked at the border between water and land, the shoreline, and the border between sand and vegetation, the vegetation line. The Satellite-Derived Beach Width (SDBW) is defined as the cross-shore distance between the Satellite-Derived Shoreline (SDS) and the Satellite-Derived Vegetation Line (SDV). We sometimes refer to these parameters comprehensively as the Satellite-Derived Parameters (SDPs).

2. How can beach width and beach width dynamics be derived from optical satellite imagery in a semi-automated way?

We derived a method for detecting beach width from optical satellite imagery based on the Normalized Difference Indices, such as the NDVI and NDWI. With these indices, the pixels of an optical satellite image are partitioned into two (or more) contrasting land cover types. After several image pre-processing steps, the SDBW method produces a binary image of the land and water pixels derived from a satellite image with the NDWI. The border between those two land cover clusters is contoured, smoothened, and subsequently made into a vector representing the SDS. In a simultaneous process, the water pixels of the NDWI image are masked, and the NDVI is applied to the remaining land pixels. In this way, the sand and vegetation pixels can be partitioned from the water-masked image. Then the SDV can be derived from the border between the sand and vegetation pixel clusters, in the same way as for the SDS. Subsequently, the SDBW is computed by taking the cross-shore distance between the SDS and the SDV along (predefined) cross-shore transects.

The SDBW method can generate short- and long-term beach width variations per transect by computing a linear regression line of the SDBW sizes derived over a certain period. Separate analyses of the SDS and SDV dynamics are essential for interpreting the SDBW dynamics.

The SDBW detection method is semi-automated. After selecting an area of interest, the preferred satellite data, a time window, cloud cover percentage, and some simulation settings, the computation of the SDS and SDV runs independently, and the data is contained in geographic datafiles. When the SDS and SDV vectors are derived from the satellite data, the data is post-processed to derive the SDS and SDV positions, and so the SDBW size for each predefined transect along the studied coastal area. Subsequently, the dynamics can be derived from the acquired data.

3. How does the Satellite-Derived Beach Width (SDBW) compare to beach widths from in-situ measurement surveys (such as JARKUS)?

We compared the SDBW with the Total Beach Width (MLW to Dunefoot) and Dry Beach Width (MHW to Dunefoot) from JARKUS. To help interpret the outcome of those comparisons, we first compared and analysed the beach width's subcomponents: the SDV with the Dunefoot, the SDS with the MLW and MHW and afterwards, the SDBW with the Dry and Total Beach Width. The results are summarized in Table 6 by presenting the longshore averages of the offsets (+ standard deviations) and differences measured between the SDP's and JARKUS parameters.

The comparison of the SDBW with JARKUS showed that the SDBW is an excellent proxy to measure beach width and beach width dynamics. However, to compare these different measurement methods is to compare coastal parameters based on elevation levels (JARKUS) with coastal parameters based on optically discernible vectors (SDBW), e.g., borders separating different land cover types. The preceding means that the parameters differ in their positional data regardless of the accuracy of the measurement method. For example, at Ameland, there simply exists an actual physical distance between the +3m elevation contour and the most seaward vegetation contour. The measurement data showed that the SDV has a pretty consistent offset of 40 to 50 meters landward of the Dunefoot position, which, confirmed by visual observations of the data, is mainly related to the mentioned physical distance between the two parameters. The SDS lies, on average, between the MLW and MHW (the intertidal area) and has a strong bias towards the MHW position. Regardless of the differences between the two measurement types, and the resulting indicators for the seaward and landward borders of the beach, the compared beach widths show many similarities. We found that the SDBW shows the most similarities to the Dry Beach Width in terms of beach width size (see Table 6), trend magnitude, and direction (e.g., growth or decay). This can be explained by the relative bias of the SDS toward the MHW.

For a large part of the studied reach, the evolution of the size and especially the dynamics of the SDBW (and JARKUS beach widths) are dominated heavily by the evolution of the SDS (or JARKUS shoreline

parameters). Long-shore averages of the dynamics (trends) are regarded insignificant; hence, no overview is presented in a Table.

The trends measured from the SDP's and JARKUS parameters are most similar to each other at the so-called *uniform area* (transects 700 to 2100), which is a relatively static area in terms of dynamics compared to the so-called *dynamic area (*transects 300 to 700). At the dynamic area, where a lot happens in a geographical and morphological sense, the SDPs show less correspondence to the JARKUS parameters but still resemble pretty well in terms of trend direction (see Figure 34 and Figure 44). The SDV and Dunefoot seem to act as predictors in relation to each other at the dynamic area. In other words, at some locations, the most seaward vegetation limit (measured by the SDV) significantly expanded in seaward direction several years before the position of the +3m elevation contour (the Dunefoot) caught up with this seaward shift. This can be explained by the natural relationship between sedimentation and vegetation; when (embryonal) dune vegetation gets the chance to develop in a seaward direction, sedimentation accumulates between the young dune vegetation, reinforcing the development of both sedimentation and vegetation. This process works both ways, be it with a certain delay of the other parameter.

In conclusion, the comparison of the SDBW with JARKUS data provided a decent first impression of the performance and accuracy of the SDBW detection method and its capability to measure beach width and beach width dynamics.

4. How does the increased spatial and temporal resolution of the SDBW contribute to the existing (in-situ) possibilities for measuring and analysing beach width dynamics?

The SDBW contributes to existing options for measuring and analysing beach width dynamics in several ways. This research shows that with the developed SDV detection method, it is possible to obtain an accurate position of the vegetation line from both composite and individual images, given that the images are of good enough quality. From the Ameland case study, it can be concluded that the SDBW, derived from the SDV and SDS, is a good proxy to measure beach width and beach width dynamics. In this sense, the SDBW method can contribute to existing studies of beach width dynamics since the satellite data is free-of-cost, whereas the JARKUS survey (or other in-situ measurement campaigns) is very costly.

Furthermore, from the publicly available optical satellite imagery, SDBW data can be derived on a (bi-)weekly basis, provided that the satellite images are of good quality. Compared to the JARKUS measurement surveys, this provides high-resolution data available between the annually measured JARKUS surveys and up to a year after the most recently executed JARKUS survey. Furthermore, with those satellites, the SDBW can be measured every 10 to 30 meters in between the cross-shore JARKUS transects that are alongshore-spaced every 200 to 250 meters, be it with a lesser cross-shore resolution.

The high-resolution of the SDV enables measurement of short-term (intra-annual) dynamics of the in-situ vegetation contour, such as dune erosion due to storm events or gradual expansion of vegetated dunes. Furthermore, at a location with unique geographic characteristics, the SDV could predict, on an intra-annual scale, where the Dunefoot position (defined at +3m NAP) might develop towards months in advance of the following JARKUS survey. Also, the SDV might, in some situations, be better suited for measuring dynamics of the landward border of the beach since they are optically measured and unrelated to the (sometimes limited) elevation-based definition of the Dunefoot fixed at +3 m NAP.

5. How do (local) geographic conditions and algorithm settings influence the detection process of the SDBW?

Geographic conditions and algorithm settings influence the quality of SDBW detection in several ways. We learned that the following factors influence the SDV and SDS detection and, therefore, the SDBW detection.

Supervised NDVI threshold value for SDV detection
The detection of the SDV position depends on the selection of a threshold value for separating the pixel masses in the NDVI histogram corresponding to sand and vegetation land cover areas. A supervised threshold value (0.15) was determined for detecting the SDV from Ameland's sandy beach with vegetated dunes. This value is expected to be applicable for SDV detection at other beaches with vegetated dunes, with similar characteristics such as sediment and vegetation types. Additional case studies have to assess whether we can use the same or need a different threshold value at beaches with other sediment or vegetation characteristics.

SDV seasonal variation is related to the variability of vegetation greenness
The detection of the SDV position is influenced by the seasonal variability of vegetation greenness. During the year, reflection values of vegetation pixels vary in strength due to natural processes (e.g., photosynthesis and rainfall). This seasonal variability of the SDV position is unrelated to actual movement of the (most-seaward) vegetation contour. Based on analyses from individual images, this seasonal fluctuation is 23 meters within one year. The SDV position in summer is most representative of the actual most seaward vegetation contour. It could be worthwhile to investigate whether there is a way to filter this variation in the detection process or from the data by post-processing.

SDS variation related to tidal and hydrodynamic variability
The detection of the SDS position is influenced by the tidal and hydrodynamic variability of the shoreline, which is not related to the actual shoreline and, therefore, beach width change. This is already extensively discussed in previous work of, among others, Hagenaars (2017) and Hagenaars et al. (2018).

Availability of usable images during the year
In line with expectation, we found that there were more usable images available (approximately twice as much) in Spring and Summer than in Autumn and Winter, based on four years of Sentinel-2 data. Hence, analysis of SDBW data is of higher temporal resolution in Spring and Summer. When using composite images or when looking at, for example, (multi-annual) temporal averages of the offset between SDS, SDV and JARKUS parameters, the SDS and SDV data might be biased towards a Spring/Summer position due to the higher density of usable images in those seasons.

Quality of composite images
The use of composite images over single images is suggested in literature to reduce the negative influence of optical satellite-related drivers of inaccuracy, such as clouds (and cloud shadows), hydrodynamic conditions, and technical errors at the cost of temporal resolution of the measurement data. However, for the composite image data used for the Ameland case study, it frequently occurred that single erroneous or faulty images negatively influenced a sequence of composite images. Hence, the quality of the composite images influences the detection process of the SDBW.

6.2 Recommendations
This research provided a first impression of the possibilities and limitations of the SDBW detection method. In this section, we give recommendations towards utilizing the potential of the detection method, which in our opinion could optimize the detection process of the SDBW and its subcomponents, give a better estimation of the accuracy of the detected SDBWs and increase our insight into the dynamics and variability of beach widths along sandy beaches around the world.

It is just a matter of time before publicly available satellite missions will be launched with finer pixel resolutions (< 1m) and shorter revisit times (<1 day) compared to the current Landsat and Sentinel 2 satellite missions. Higher-resolution satellite imagery will naturally improve the spatiotemporal accuracy of the satellite-derived measurement data. However, the development of satellite sensors is out of the coastal researcher its control.

In the meantime, we present seven recommendations here that we deem relevant for further validation of the SDBW method, optimization of the SDBW detection process, expanding the method's applicability (worldwide), and improving analyses of the measurement data.

1. Perform a direct comparison between SDBW data derived from composite and individual images with exactly the same research periods, algorithm settings and satellite data source. The analyses done in this research with composite and individual images have, besides the used image types, two significant diverging factors that influence the validity of the comparison. These factors are (1) the satellite type (Landsat 5 & 8 vs Sentinel-2) and hence the pixel resolution, and (2) the studied period (1984-2018 vs 2015-2019), and thus strongly diverging (morpho-)dynamics. Hence, it is recommended to derive SDBW data from composite and individual images of the same satellite type and the same period, in particular from Sentinel-2 images between 2015 and 2022 and make a similar comparison of the SDBW and JARKUS data as was done in this study. This direct comparison should give a better impression of the performance of composite and individual images for measuring SDBW (and SDS and SDV) and also of the preferred cloud cover and algorithm settings.

2. Perform extra case studies to validate the SDBW method for other beaches in the Netherlands (or elsewhere) with geographic characteristics similar to the uniform area at Ameland's northern coast. Thus, focussing on sandy beaches bordered by vegetated dunes. Regarding dynamics, it is preferred to look at a more static beach, since the large offsets and high change rates of the coastal parameters measured at the dynamic area complicated a decent accuracy assessment. By first studying beaches comparable to Ameland's uniform area, we aim to establish confidence in the performance of the SDBW method and increase insight into the dynamic behaviour of the SDBW, SDS and SDV, and the relationship between those parameters. For example, one could assess if there is a comparable relationship between the SDV and Dunefoot (e.g., the consistent offset) or that the SDS also displays a bias towards the MHW at other locations with similar geographic characteristics. Additionally, it should be assessed whether the supervised NDVI threshold value of 0.15 determined in this study is also suited for SDV detection at other locations or whether other values might fit better.

3. Execute a thorough accuracy assessment of the SDV detection, preferably with high-resolution in-situ vegetation cover data. In this research, we assumed the detection accuracy of the newly introduced SDV to be in the order of the SDS's accuracy mentioned by other researchers in recent studies. For the SDBW method to be broadly adopted, a better valuation of the SDV's accuracy is necessary. This might appear contradictory because of the large offsets found between the SDS and the MLW and MHW (especially at the dynamic area), but since the SDS has been validated sufficiently in other studies, we believe that those offsets are more related to physical differences between the compared parameters (SDBW vs JARKUS) or the hydrodynamic conditions.

4. After the SDBW method is sufficiently validated at beaches similar to Ameland's uniform area, the method should be tested at beaches with different types of sediment and vegetation (and potentially other beach characteristics) to see how the SDS and SDV detection perform under alternative circumstances. This would expand the measurement possibilities of the SDBW detection method to other geographically characterized beaches.

5. The pre-processing steps could be optimized by, for example, pre-screening the satellite images used to construct a composite image on their quality. This would prevent sequences of composite images from being compromised by one faulty image occurring in the composite window (e.g., 180 to 360 days) of multiple composite images. The exclusion of those faulty images would significantly increase the quality of composite measurement data. In composing composite satellite images, filter the Cloud Cover data of the satellite images

for the Area of Interest instead of the complete swath of the satellite images. After implementing these improvements, the optimum settings for composing composite images should be reassessed.

6. Optimize the detection method by implementing more advanced image-processing algorithms or other relevant mathematical algorithms to reduce computation time in the detection process. For example, one option could be applying a method for automated (instead of supervised) NDVI threshold selection that correctly separates sand and vegetation pixels for SDV computation. Better yet, if possible, a multi-threshold selection method for separating water, sand, and vegetation pixels masses from one single Normalized Difference Index would enable detection of the SDS and SDV in one single process instead of two parallel processes which would substantially reduce computation time.

7. Optimize the post-processing steps presented in this research by looking for more innovative methods to improve usability and get the most out of the measurement data. This could, for example, be done by focusing specifically on image quality (usability) above individual transects. Hence, a filter could be created to screen images in the post-processing phase only to include measurement data from the transects that are unhampered by clouds or other drivers of inaccuracy. In that way, all individual satellite images (with any amount of cloud cover) in a studied period can be included in the analyses, and no valid data is lost. For example, if you have five completely visible transects on an image almost entirely covered with clouds, the measurement data from those particular transects will not be omitted.

8. A different approach, but in the same line of thought as recommendation 7, could be creating time-stacks of satellite snapshots of polygons fixed specifically on single transects. E.g., by creating a polygon that covers the complete length of a transect and is, for example, 10 meters wide, a time-stack of very narrow transect satellite images can be generated. From those time-stacks, the faulty images can very easily be filtered on a local (transect) scale. In theory, if sensible measurement data can be extracted from these narrow polygons, this would result in the cleanest data per single transect. Logically, long-shore analyses require time-stacks of a multitude of adjacent transects. The generation, post-processing, and analyses of these sequences of transect time-stacks might require increased computation time, but the extraction of the data could, on the other hand, reduce computation time since satellite images of (a limited number) of very small polygons (transect size) need to be extracted from the GEE's servers. Those transect size polygons are tremendously smaller than the area of interest of a whole coastline, such as, for example, the area selected for the Ameland case study.

9. Regarding the analyses in this research about the trends measured from the SDBW, SDS and SDV, several ideas or improvements can be thought of for additional or more sophisticated research. Applying a more advanced method than the linear regression line might improve the accuracy of the measured coastal trends, such as the Weighted Regression Line (WRL). In this research, we restricted to measuring SDBW data along the 200 to 250m alongshore-spaced (RSP) transects used in the JARKUS survey. Whereas with the SDBW method, we can measure in between those transects, providing higher spatial resolution measurement data that enables more sophisticated analyses in the spatial sense.

Bibliography

Adnan, F. A. F., Hamylton, S. M., & Woodroffe, C. D. (2016). A Comparison of Shoreline Changes Estimated Using the Base of Beach and Edge of Vegetation Line at North Keeling Island. *Journal of Coastal Research*, *75*(sp1), 967–971. https://doi.org/10.2112/SI75-194.1

Almar, R., Bergsma, E. W. J., Maisongrande, P., & de Almeida, L. P. M. (2019). Wave-derived coastal bathymetry from satellite video imagery: A showcase with Pleiades persistent mode. *Remote Sensing of Environment*, *231*(December 2018), 111263. https://doi.org/10.1016/j.rse.2019.111263

Almeida, L. P., Almar, R., Bergsma, E. W. J., Berthier, E., Baptista, P., Garel, E., Dada, O. A., & Alves, B. (2019). Deriving high spatial-resolution coastal topography from sub-meter satellite stereo imagery. *Remote Sensing*, *11*(5). https://doi.org/10.3390/rs11050590

Battiau-queney, Y., Franc, J., Chaverot, S., & Lanoy-ratel, P. (2003). Recent shoreline mobility and geomorphologic evolution of macrotidal sandy beaches in the north of France. *Marine Geology*, *194*, 31–45. https://doi.org/10.1016/S0025-3227(02)00697-7

Bauer, B. O., & Davidson-Arnott, R. G. D. (2003). A general framework for modeling sediment supply to coastal dunes including wind angle, beach geometry, and fetch effects. *Geomorphology*, *49*(1), 89–108. https://doi.org/10.1016/S0169-555X(02)00165-4

Bergsma, E. W. J., Almar, R., Rolland, A., Binet, R., Brodie, K. L., & Bak, A. S. (2021). Coastal morphology from space: A showcase of monitoring the topography-bathymetry continuum. *Remote Sensing of Environment*, *261*, 112469. https://doi.org/10.1016/j.rse.2021.112469

Boak, E. H., & Turner, I. L. (2005). Shoreline Definition and Detection: A Review. *Journal of Coastal Research*, *214*, 688–703. https://doi.org/10.2112/03-0071.1

Cohn, N., Ruggiero, P., García-Medina, G., Anderson, D., Serafin, K. A., & Biel, R. (2019). Environmental and morphologic controls on wave-induced dune response. *Geomorphology*, *329*, 108–128. https://doi.org/10.1016/j.geomorph.2018.12.023

Damsma, T. (2009). *Dune growth on natural and nourished beaches: 'A new perspective.'*

Davidson, M., Van Koningsveld, M., de Kruif, A., Rawson, J., Holman, R., Lamberti, A., Medina, R., Kroon, A., & Aarninkhof, S. (2007). The CoastView project: Developing video-derived Coastal State Indicators in support of coastal zone management. *Coastal Engineering*, *54*(6–7), 463–475. https://doi.org/10.1016/j.coastaleng.2007.01.007

de Groot, A. V., de Vries, S., Keijsers, J. G. S., Riksen, M. J. P. M., van Ye, Q., Poortinga, A., Arens, S. M., Bochev-Van der Burgh, L. M., Wijnberg, K. M., Schretlen, J. L., & van Thiel de Vries, J. S. M. (2012). Measuring and modeling coastal dune development in the Netherlands. *NCK-Days 2012 : Crossing Borders in Coastal Research : Jubilee Conference Proceedings*, *January*. https://doi.org/10.3990/2.178

de Schipper, M. A., de Vries, S., Ruessink, G., de Zeeuw, R. C., Rutten, J., van Gelder-Maas, C., & Stive, M. J. F. (2016). Initial spreading of a mega feeder nourishment: Observations of the Sand Engine pilot project. *Coastal Engineering*, *111*, 23–38. https://doi.org/10.1016/j.coastaleng.2015.10.011

de Vries, S., Arens, S. M., de Schipper, M. A., & Ranasinghe, R. (2014). Aeolian sediment transport on a beach with a varying sediment supply. *Aeolian Research*, *15*, 235–244. https://doi.org/10.1016/j.aeolia.2014.08.001

de Vries, S., Southgate, H. N., Kanning, W., & Ranasinghe, R. (2012). Dune behavior and aeolian transport on decadal timescales. *Coastal Engineering*, *67*, 41–53. https://doi.org/10.1016/j.coastaleng.2012.04.002

de Vries, Sierd, Arens, S., Stive, M., & Ranasinghe, R. (2011). Dune growth trends and the effects of beach width on annual timescales. *Coastal Sediments '11*, 1867–1876. https://doi.org/10.1142/9789814355537

Decisio. (2011). *Ruimte voor recreatie op het strand - Onderzoek naar een "recreatiebasiskustlijn."*

DHV. (2005). *Beleidsevaluatie "Dynamisch handhaven."* https://zoek.officielebekendmakingen.nl/kst-27625-58-b1

Donchyts, G., Baart, F., Winsemius, H., Gorelick, N., Kwadijk, J., & Van De Giesen, N. (2016). Earth's surface water change over the past 30 years. *Nature Climate Change*, *6*(9), 810–813. https://doi.org/10.1038/nclimate3111

Dugan, J. E., Hubbard, D. M., & Quigley, B. J. (2013). Beyond beach width: Steps toward identifying and integrating ecological envelopes with geomorphic features and datums for sandy beach ecosystems. *Geomorphology*, *199*, 95–105. https://doi.org/10.1016/j.geomorph.2013.04.043

Durán, R., Guillén, J., Ruiz, A., Jiménez, J. A., & Sagristà, E. (2016). Morphological changes, beach inundation and overwash caused by an extreme storm on a low-lying embayed beach bounded by a dune system (NW Mediterranean). *Geomorphology*, *274*, 129–142. https://doi.org/10.1016/j.geomorph.2016.09.012

ESA. (n.d.). *Sentinel 2: The Operational Copernicus Optical High Resolution Land Mission*. Retrieved July 2, 2018, from www.esa.int/copernicus

García-Rubio, G., Huntley, D., & Russell, P. (2015). Evaluating shoreline identification using optical satellite images. *Marine Geology, 359*, 96–105. https://doi.org/10.1016/j.margeo.2014.11.002

Gens, R. (2010). Remote sensing of coastlines: Detection, extraction and monitoring. *International Journal of Remote Sensing*, *31*(7), 1819–1836. https://doi.org/10.1080/01431160902926673

Giardino, A., Santinelli, G., & Vuik, V. (2014). Coastal state indicators to assess the morphological development of the Holland coast due to natural and anthropogenic pressure factors. *Ocean and Coastal Management*, *87*, 93–101. https://doi.org/10.1016/j.ocecoaman.2013.09.015

Gómez, C., White, J. C., & Wulder, M. A. (2016). Optical remotely sensed time series data for land cover classification: A review. *ISPRS Journal of Photogrammetry and Remote Sensing*, *116*, 55–72. https://doi.org/10.1016/j.isprsjprs.2016.03.008

Guillén, J., Stive, M. J. F., & Capobianco, M. (1999). Shoreline evolution of the Holland coast on a decadal scale. *Earth Surface Processes and Landforms*, *24*(6), 517–536. https://doi.org/10.1002/(SICI)1096-9837(199906)24:6<517::AID-ESP974>3.0.CO;2-A

Hagenaars, G., de Vries, S., Luijendijk, A. P., de Boer, W. P., & Reniers, A. J. H. M. (2018). On the accuracy of automated shoreline detection derived from satellite imagery: A case study of the sand motor mega-scale nourishment. *Coastal Engineering*, *133*, 113–125. https://doi.org/10.1016/j.coastaleng.2017.12.011

Hagenaars, G. S. (2017). *Accuracy assessment of coastline dynamics based on satellite images*. TU Delft.

Harley, M. D., Turner, I. L., Short, A. D., & Ranasinghe, R. (2009). An empirical model of beach response to storms-SE Australia. *19th Australasian Coastal and Ocean Engineering Conference 2009 and the 12th Australasian Port and Harbour Conference 2009, COASTS and PORTS 2009*, *June*, 589–595.

Himmelstoss, E. A., Henderson, R. E., Kratzmann, M. G., & Farris, A. S. (2021). Digital Shoreline Analysis System (DSAS) Version 5.1 User Guide: U.S. Geological Survey Open-File Report 2021–1091. In *U.S. Geological Survey*.

Hulskamp, R. (2021). *Global distribution of muddy coasts using a hybrid classification model: An automated method that employs multispectral satellite imagery and globally available coastal datasets* [Delft University of Technology]. https://repository.tudelft.nl/islandora/object/uuid%3A3739a746-7d25-4d46-9870-9090ce0d5057

Jiménez, J. A., Osorio, A., Marino-Tapia, I., Davidson, M., Medina, R., Kroon, A., Archetti, R., Ciavola, P., & Aarninkhof, S. G. J. (2007). Beach recreation planning using video-derived coastal state indicators. *Coastal Engineering*, *54*(6–7), 507–521. https://doi.org/10.1016/j.coastaleng.2007.01.012

Jiménez, José A., Valdemoro, H. I., Bosom, E., Sánchez-Arcilla, A., & Nicholls, R. J. (2017). Impacts of sea-level rise-induced erosion on the Catalan coast. *Regional Environmental Change*, *17*(2), 593–603. https://doi.org/10.1007/s10113-016-1052-x

Keijsers, J.G.S., De Groot, A. V., & Riksen, M. J. P. M. (2015). Vegetation and sedimentation on coastal foredunes. *Geomorphology*, *228*, 723–734. https://doi.org/10.1016/j.geomorph.2014.10.027

Keijsers, Joep G.S., Poortinga, A., Riksen, M. J. P. M., & Maroulis, J. (2014). Spatio-temporal variability in accretion and erosion of coastal foredunes in the Netherlands: Regional climate and local topography. *PLoS ONE*, *9*(3). https://doi.org/10.1371/journal.pone.0091115

Krol, J. (2019). *Vegetatieontwikkeling op het Groene strand bij Ballum op Ameland.* https://basismonitoringwadden.waddenzee.nl/fileadmin/inhoud/pdf/verslag_groene_strand_2019.pdf

Kuleli, T., Guneroglu, A., Karsli, F., & Dihkan, M. (2011). Automatic detection of shoreline change on coastal Ramsar wetlands of Turkey. *Ocean Engineering*, *38*(10), 1141–1149. https://doi.org/10.1016/j.oceaneng.2011.05.006

Luijendijk, A., Hagenaars, G., Ranasinghe, R., Baart, F., Donchyts, G., & Aarninkhof, S. (2018). The State of the World's Beaches. *Nature*, 1–11. https://doi.org/10.1038/s41598-018-24630-6

Mahabot, M. M., Jaud, M., Pennober, G., Le Dantec, N., Troadec, R., Suanez, S., & Delacourt, C. (2017). The basics for a permanent observatory of shoreline evolution in tropical environments; lessons from back-reef beaches in La Reunion Island. *Comptes Rendus - Geoscience*, *349*(6–7), 330–340. https://doi.org/10.1016/j.crte.2017.09.010

Mastbergen, D., Nederhoff, K., van der Valk, B., & Maarse, M. (2018). *Beheerbibliotheek Ameland - Beschrijvingen van het kustvak ter ondersteuning van het beheer en onderhoud van de kust* (2018th ed.).

Montaño, J., Coco, G., Chataigner, T., Yates, M., Le Dantec, N., Suanez, S., Cagigal, L., Floc'h, F., & Townend, I. (2021). Time-Scales of a Dune-Beach System and Implications for Shoreline Modeling. *Journal of Geophysical Research: Earth Surface*, *126*(11), 1–24. https://doi.org/10.1029/2021JF006169

Moulton, M. A. B., Hesp, P. A., Miot da Silva, G., Keane, R., & Fernandez, G. B. (2021). Surfzone-beach-dune interactions along a variable low wave energy dissipative beach. *Marine Geology*, *435*(May 2020), 106438. https://doi.org/10.1016/j.margeo.2021.106438

Nolet, C., & Riksen, M. J. P. M. (2018). Accommodation space indicates dune development potential along an urbanized and frequently nourished coastline. *Earth Surface Dynamics Discussions*, *May*. https://doi.org/https://doi.org/10.5194/esurf-2018-37

Orseau, S., Abascal Zorrilla, N., Huybrechts, N., Lesourd, S., & Gardel, A. (2020). Decadal-scale morphological evolution of a muddy open coast. *Marine Geology*, *420*(August 2019), 106048. https://doi.org/10.1016/j.margeo.2019.106048

Otsu, N. (1979). A Threshold Selection Method from Gray-Level Histograms. *IEEE Transactions on Systems, Man, and Cybernetics*, *9*(1), 62–66. https://doi.org/10.1109/TSMC.1979.4310076

Percentage difference between images - Rosetta Code. (n.d.). Retrieved December 21, 2021, from https://rosettacode.org/wiki/Percentage_difference_between_images

Pollard, J. A., Spencer, T., Brooks, S. M., Christie, E. K., & Möller, I. (2020). Understanding spatio-temporal barrier dynamics through the use of multiple shoreline proxies. *Geomorphology*, *354*, 107058. https://doi.org/10.1016/j.geomorph.2020.107058

Rader, A. M., Pickart, A. J., Walker, I. J., Hesp, P. A., & Bauer, B. O. (2018). Foredune morphodynamics and sediment budgets at seasonal to decadal scales: Humboldt Bay National Wildlife Refuge, California, USA. *Geomorphology*, *318*, 69–87. https://doi.org/10.1016/j.geomorph.2018.06.003

Rijkswaterstaat. (2017). *Kustlijnkaarten 2018.* http://publicaties.minienm.nl/download-bijlage/90006/kustlijnkaarten-2018.pdf

Roelse, P. (2002). *Water en zand in balans.*

Ruessink, B. G., & Jeuken, M. C. J. L. (2002). Dunefoot dynamics along the Dutch coast. *Earth Surface Processes and Landforms*, *27*(10), 1043–1056. https://doi.org/10.1002/esp.391

Stive, M. J. F., Aarninkhof, S. G. J., Hamm, L., Hanson, H., Larson, M., Wijnberg, K. M., Nicholls, R. J., & Capobianco, M. (2002). Variability of shore and shoreline evolution. *Coastal Engineering*, *47*(2), 211–235. https://doi.org/10.1016/S0378-3839(02)00126-6

The European Space Agency (ESA). (n.d.). *User Guides - Sentinel-2 MSI - Sentinel Online - Sentinel Online.* Retrieved January 14, 2022, from https://sentinels.copernicus.eu/web/sentinel/user-guides/sentinel-2-msi

Turner, I. L., Harley, M. D., Almar, R., & Bergsma, E. W. J. (2021). Satellite optical imagery in Coastal Engineering. *Coastal Engineering*, *167*, 103919. https://doi.org/10.1016/j.coastaleng.2021.103919

U.S. Geological Survey. (n.d.). *Landsat Satellite Missions | U.S. Geological Survey.* Retrieved January 14, 2022, from https://www.usgs.gov/landsat-missions/landsat-satellite-missions

U.S. Geological Survey. (2015). Landsat—Earth observation satellites. *Fact Sheet*, 1–4. https://doi.org/10.3133/fs20153081

van der Werff, H. M. A. (2019). Mapping shoreline indicators on a sandy beach with supervised edge detection of soil moisture differences. *International Journal of Applied Earth Observation and Geoinformation*, *74*(April 2018), 231–238. https://doi.org/10.1016/J.JAG.2018.09.007

van Koningsveld, M., & Mulder, J. P. M. (2004). Sustainable Coastal Policy Developments in The Netherlands. A Systematic Approach Revealed. *Journal of Coastal Research*, *202*, 375–385. https://doi.org/10.2112/1551-5036(2004)020[0375:SCPDIT]2.0.CO;2

van Puijenbroek, M. E. B., Limpens, J., de Groot, A. V., Riksen, M. J. P. M., Gleichman, M., Slim, P. A., van Dobben, H. F., & Berendse, F. (2017). Embryo dune development drivers: beach morphology, growing season precipitation, and storms. *Earth Surface Processes and Landforms*, *42*(11), 1733–1744. https://doi.org/10.1002/esp.4144

Vandebroek, E., Dan, S., Vanlede, J., Verwaest, T., & Mostaert, F. (2017). *Sediment budget for the Belgian coast: final report. Version 2.0. 12_155_1.* http://documentatiecentrum.watlab.be/owa/imis.php?module=ref&refid=286606

Walker, I. J., Davidson-Arnott, R. G. D., Bauer, B. O., Hesp, P. A., Delgado-Fernandez, I., Ollerhead, J., & Smyth, T. A. G. (2017). Scale-dependent perspectives on the geomorphology and evolution of beach-dune systems. *Earth-Science Reviews*, *171*(April), 220–253. https://doi.org/10.1016/j.earscirev.2017.04.011

Wang, Z., Bovik, A. C., Sheikh, H. R., & Simoncelli, E. P. (2004). Image quality assessment: From error visibility to structural similarity. *IEEE Transactions on Image Processing*, *13*(4), 600–612. https://doi.org/10.1109/TIP.2003.819861

Wernette, P., Thompson, S., Eyler, R., Taylor, H., Taube, C., Medlin, A., Decuir, C., & Houser, C. (2018). Defining Dunes: Evaluating How Dune Feature Definitions Affect Dune Interpretations from Remote Sensing. *Journal of Coastal Research*, *34*(6), 1460–1470. https://doi.org/10.2112/JCOASTRES-D-17-00082.1

Yang, H., Yang, X., Heskel, M., Sun, S., & Tang, J. (2017). Seasonal variations of leaf and canopy properties tracked by ground-based NDVI imagery in a temperate forest. *Scientific Reports*, *7*(1), 1–10. https://doi.org/10.1038/s41598-017-01260-y

Yousefi Lalimi, F., Silvestri, S., Moore, L. J., & Marani, M. (2017). Coupled topographic and vegetation patterns in coastal dunes: Remote sensing observations and ecomorphodynamic implications. *Journal of Geophysical Research: Biogeosciences*, *122*(1), 119–130. https://doi.org/10.1002/2016JG003540

List of figures

List of tables

List of abbreviations

CSI	Coastal State Indicator
ESA	European Space agency
GEE	Google Earth Engine
HBPZ	Hondsbossche and Pettemer Zeewering
JARKUS	JAaRlijkse KUStmetingen
LIDAR	Light Detection And Ranging
MHW	Mean High Water
MLW	Mean Low Water
MSL	Mean Sea Level
NAP	Normaal Amsterdams Peil (Dutch Ordnance Datum)
NASA	National Aeronautics and Space Administration
NDVI	Normalized Difference Vegetation Index
NDWI	Normalized Difference Water Index
NIR	Near Infra-Red
RADAR	Radio Detection and Ranging
RSP	Rijksstrandpaal/RijksStrandPalen
RWS	Rijkswaterstaat
SDBW	Satellite-Derived Beach Width
SDP	Satellite-Derived Parameter
SDS	Satellite-Derived Shoreline
SDV	Satellite-Derived Vegetation line
TOA	Top-Of-Atmosphere
USGS	U.S. Geological Survey

Appendix A − NDVI Threshold selection for SDV detection

This appendix presents the results of two assessments for the NDVI threshold selection in detecting the Satellite-Derived Vegetation line. In Section A.1, a comparison is made between SDV detected with an automated threshold value and SDV detected with a supervised threshold value. Section A.2 presents a sensitivity analysis of different values of the supervised threshold value, with the aim to find the most suited supervised threshold value. Both analyses are based on comparing the SDV position with the Dunefoot position on a number of transects. We expect the SDV not to correspond precisely to the Dunefoot. However, we expect that the offset between the two indicators might provide valuable insight into the performance of the SDV and the relationship between the two indicators.

Table 7 and Table 8 list the datasets we use for the analyses in this Appendix. The datasets differ in the manner of threshold value selection (Section A.1) and the variety of supervised threshold values (Section A.2). The other parameters in the datasets are the same for all datasets, e.g., we use Composite satellite images made from Landsat 5 & Landsat 8 images acquired between November 1984 and November 2018. We compose the composite images with satellite images acquired within a 180 window and less than 60% cloud cover. These datasets are focused on the case study of Ameland. More details of the datasets are given in the specific sections.

Table 7. Datasets used in Section A.1 for the performance analysis of SDV detection with different NDVI threshold value selection; Automated versus Supervised threshold selection.

Run	Satellite mission(s)	Temporal extent	Threshold selection	Threshold value	Composite window	Cloud cover
A1	Landsat 5 & 8	11-1984 – 11-2018	Automated	[-]	180 days	<60%
S1	Landsat 5 & 8	11-1984 – 11-2018	Supervised	0.15	180 days	<60%

Table 8. Datasets used in Section A.2 for the sensitivity analysis on the performance of SDV detection, with 5 different values of Supervised NDVI threshold values

Run	Satellite mission(s)	Temporal extent	Threshold selection	Threshold value	Composite window	Cloud cover
S1	Landsat 5 & 8	11-1984 – 11-2018	Supervised	0.15	180 days	<60%
S2	Landsat 5 & 8	11-1984 – 11-2018	Supervised	0.14	180 days	<60%
S3	Landsat 5 & 8	11-1984 – 11-2018	Supervised	0.13	180 days	<60%
S4	Landsat 5 & 8	11-1984 – 11-2018	Supervised	0.12	180 days	<60%
S5	Landsat 5 & 8	11-1984 – 11-2018	Supervised	0.11	180 days	<60%

For the analyses in this Appendix, we use the satellite composite images of which their acquisition date is closest to the measurement dates of the JARKUS survey. Figure 48 presents the JARKUS survey dates, together with the acquisition dates of all available composite satellite images between 1984 and 2018 and the images selected for comparison. The 2003 JARKUS survey is excluded from the assessment because it misses most of the measurement data. Hence, we compare 33 years of JARKUS data with measurements of 33 composite images. The temporal gap between the JARKUS measurement dates and satellite image acquisition dates varies between 0 and 35 days, with one exception of 122 days for the year 2012. The number of satellite images used for the composite images varies between 3 and 12, with an average of 8 images per composite.
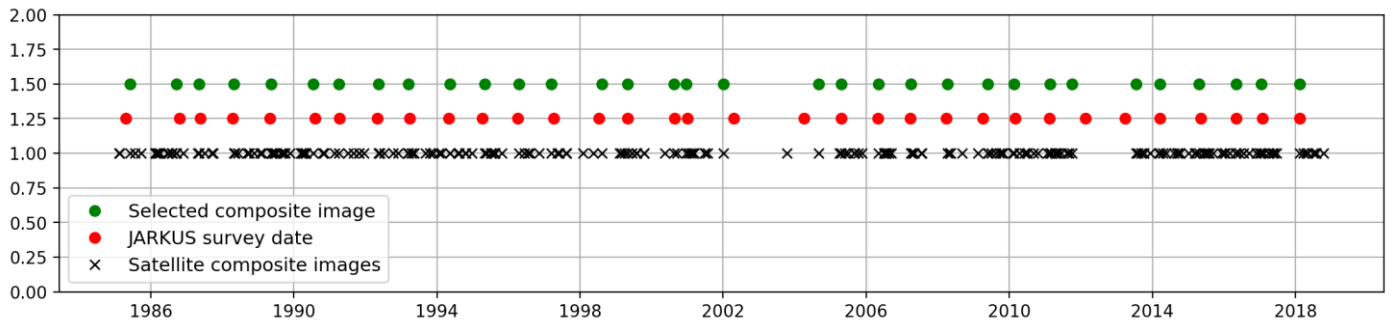
Figure 48 This figure shows the dates from all the JARKUS measurement surveys done between 1984 and 2018. The figure also shows the satellite composite images (180-day window) and a selection of those images acquired closest in time to the JARKUS dates.

A.1 Comparison of Automated versus Supervised threshold selection

We assess the performance difference between the SDV detected with an Automated and a Supervised NDVI threshold value. We assess the latter by comparing the SDV-Dunefoot offset data of both methods and visually inspecting the SDVs plotted on the satellite images relative to the coastal features.

Table 9 shows the mean and the standard deviation of the SDV-Dunefoot offset for the A1 and S1 datasets. The datasets comprise the Dunefoot and vegetation line positions relative to the RSP line for all transects and all years combined, thus averaged in space and time. For example, with 33 years and 91 transects, the datasets would ideally comprise a total of 3003 data points. However, due to corrupt satellite images, undetected cloud cover or other errors, it occasionally occurs that no SDV can be detected for specific Transects or even for the whole reach. Therefore, the resulting datasets comprise less than 3003 data points; 2566 data points for the A1 dataset and 2801 for the S1 dataset. Additionally, to exclude extreme residual values of SDV positions caused by any of the errors mentioned above, the data is filtered so that the remaining data lie within the absolute range of three standard deviations from the mean. The removed outliers account for 3.55 % of the total data points for the A1 dataset and 3.28% of the S1 dataset.

The removal of the outliers reduces both the mean and the standard deviation of the datasets. Especially the standard deviations are significantly reduced, approximately 40% for both the datasets. The threshold values that were automatically derived for the composite images of the A1 dataset vary between 0.195 and 0.352. With an average of 0.27 and a standard deviation of 0.042. The threshold values only vary in the temporal sense (per image) and not in the spatial sense (per transect) since we compute the threshold values per composite image. The threshold value statistics mentioned above apply to the dataset with the outliers removed. The remainder of the data analysis in this section focuses on the datasets from which we removed the outliers.

What stands out from the data are the significant differences between the mean offset (90 m versus 49 m) and standard deviation (60 m versus 35 m) of the A1 and S1 data sets (Table 9). The data shows that the SDVs detected with a supervised threshold value of 0.15 show a significantly smaller mean offset and standard deviation than the SDVs detected with an automatically derived threshold value ($\mu = 0.27$). Since all settings other than the threshold selection are equal for the A1 and S1 simulations, we attribute the differences between the mean and standard deviations to the difference in threshold values.

Table 9. Mean and standard deviation for the offset between the Dunefoot and SDV positions. The data is derived from Landsat 5 & 8 satellite images with a 30-meter pixel resolution.

Run	Threshold selection	Threshold value	Dataset	Data points	Mean offset μ (m)	Standard deviation σ (m)
A1	Automated	$\mu = 0.27$	Original	2566	102	98
A1	Automated	$\mu = 0.27$	Outliers removed	2475	90	60
S1	Supervised	0.15	Original	2801	56	60
S1	Supervised	0.15	Outliers removed	2709	49	35

The scatter plots depicted in Figure 49 present the positional spreading of the SDV and Dunefoot per transect and per year relative to the RSP line. It is apparent that the positional data of the SDV-S1 shows a stronger correlation with the Dunefoot and has a narrower spreading than the SDV-A1 data. Overall, the plots suggest that the SDV-S1 represents a more seaward positioned vegetation line closer to the Dunefoot than the SDV-A1. Due to the change in orientation of the positional data relative to the RSP line (x,y = 0), we identify the two distinct areas along the study reach. In either panel, the widespread (yellow) data points in the upper right section represent the dynamic hook-shaped area west of transect 700. The lower left section of densely positioned (green) data points represents the relatively stable and uniform area east of transect 700. We note that most SDVs are detected landward of the JARKUS Dunefoot position. The exceptions of the SDV positions located seaward of the Dunefoot, the data points above the 1-on-1 line, can mainly be attributed to the *out of bounds* area of vegetation that developed (somewhere in 2004) between transects 520 and 800. From those data points, one can recognize substantial dynamics of the vegetation line relative to a (near)-stationary Dunefoot, represented by the sets of vertically aligned data points above the 1-on-1 line in the right panel.
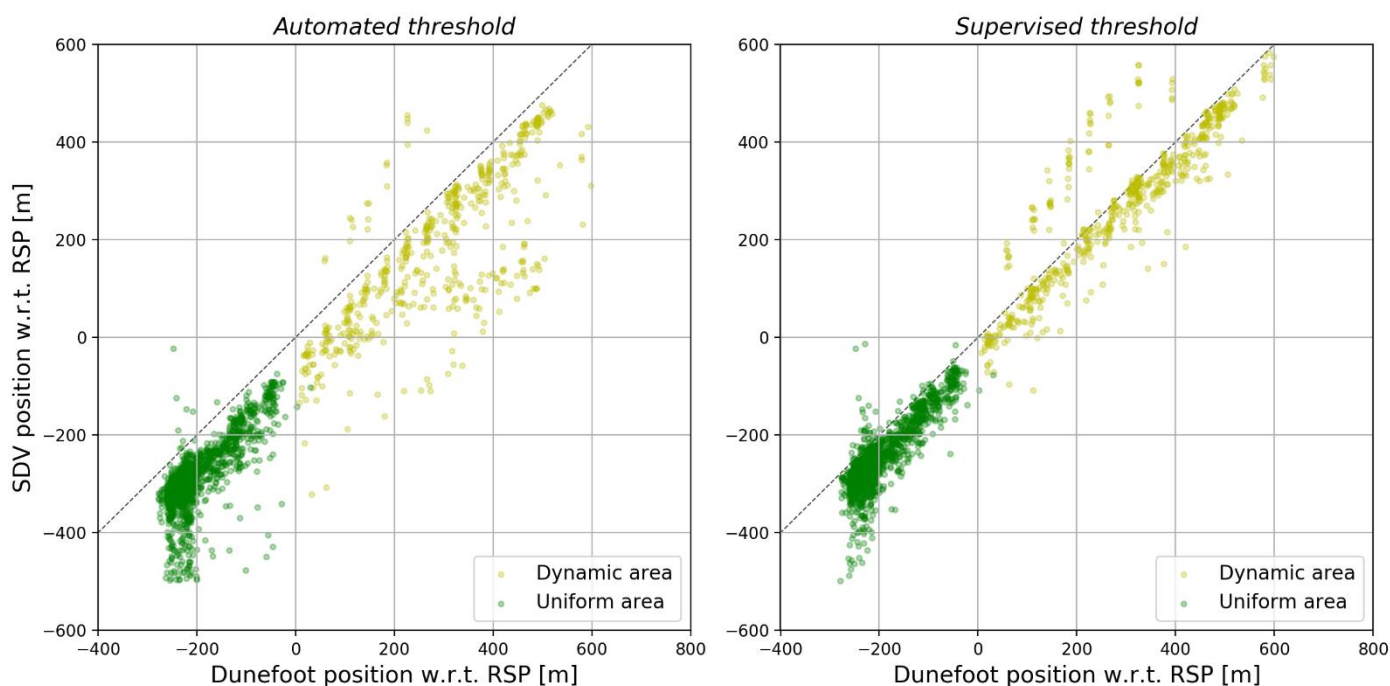

Figure 49 These graphs show the spatial spreading of the Dunefoot position versus the SDV position, relative to the RSP Line, for the SDV detected with an Automated threshold (left panel) and Supervised threshold (right panel).

Figure 50 and Figure 51 show the temporal mean offset and standard deviation per transect along the study site, from transect 300 to 2100 in a west-east direction.
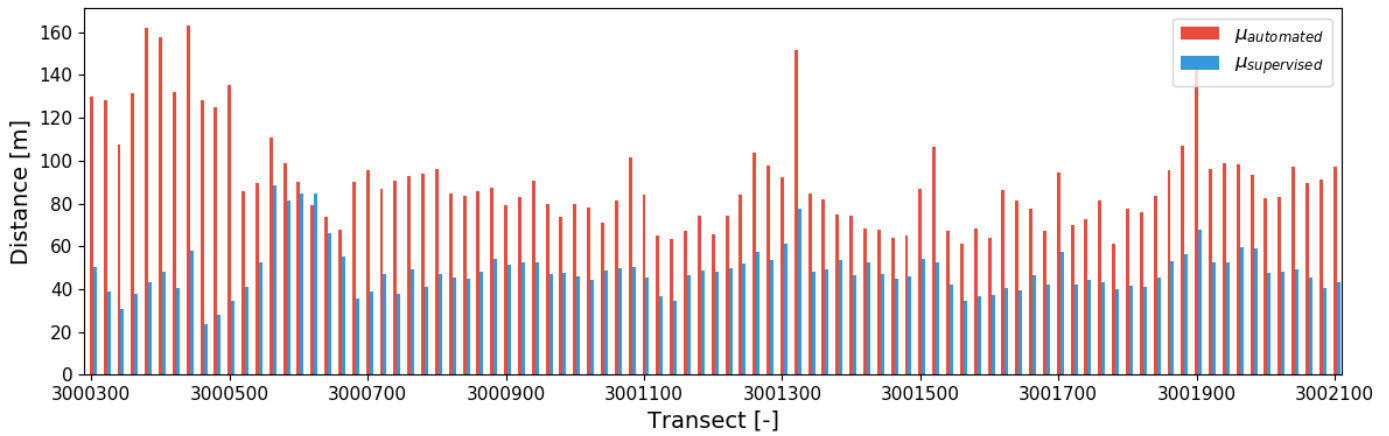
Figure 50 Temporal averages of the offset per transect between the SDV and Dunefoot positions The SDV is derived from Landsat images in the period 1985 to 2018.
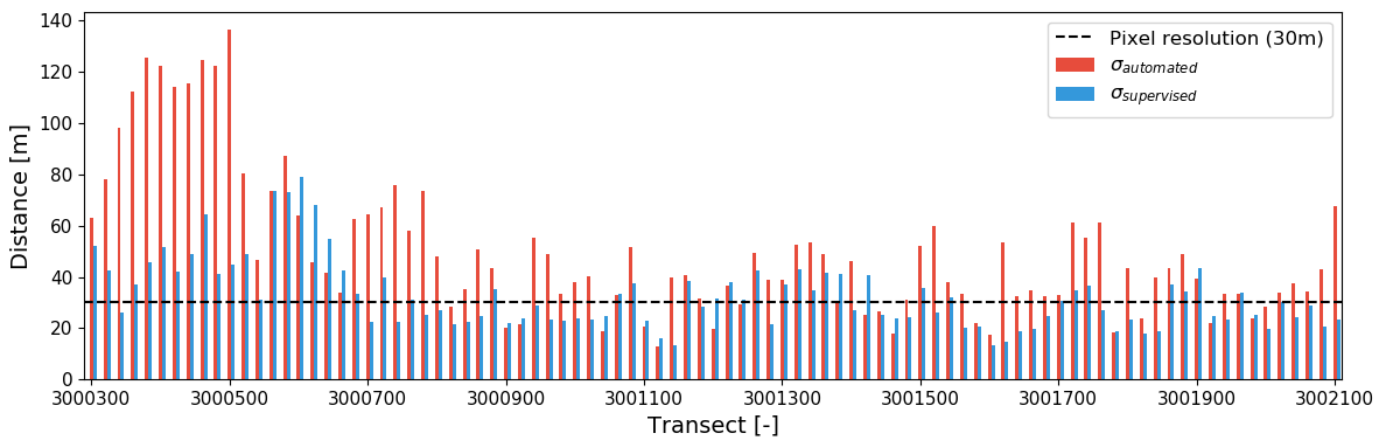

Figure 51 Standard deviation of the offset per transect between the SDV and Dunefoot positions. Relative to the satellite image pixel resolution of 30 meter. The SDV is derived from Landsat images in the period 1985 to 2018.

The most significant offsets and standard deviations are found in the dynamic area between transects 300 to 700. Interestingly enough, the data of the SDV-A1 and SDV-S1 show contrasting anomalies for the transects along the dynamic area. The SDV-A1 shows relatively large offsets and standard deviations for transects 300 to 520, the SDV-S1 shows larger offsets and standard deviations for transects 520 to 660. Figure 52 gives an example in which both distinct areas (that cause the anomalies in the data) were detected by the SDV-A1 (green) and SDV-S1 (yellow) vectors from the same composite image (Landsat 5, 2005). When we compare the SDVs with the 2005 JARKUS Dunefoot positions in the figure, one can see that the offsets can be several hundred meters wide. We further refer to the deviating area between Transects 300 and 520 as Zone-1 and the deviating area between transects 540 and 660 as Zone-2, as depicted in Figure 52.

From visual inspection of numerous SDVs, we conclude that Zone-1 is an area that varies in size and shape per composite image and has specific local characteristics which deviate from the norm, which look like alternating water bodies and darker vegetation. Furthermore, these characteristics have spectral reflectance values in a sensitive range of the NDVI pixel distribution. The latter makes that the SDV-A1, with on average higher threshold values, frequently detects Zone-1 where the SDV-S1 does not, or with less extreme deviation.

Zone-2 represents an *out of bounds* area of vegetation which was first detected by the SDV-S1 rather abruptly somewhere in 2004. Also, in the early stages of Zone-2's development, its corresponding pixels were in a sensitive range of the spectral reflection, which we noted from the 4-year delay in detection of the area by the

SDV-A1. However, since 2004 the detection of Zone-2 has been consistent, and it seems to be expanding slightly in the alongshore direction.

We find a strong contrast between the two zones; Zone-1 is somewhat arbitrarily detected over the years, Zone-2 is consistently detected in the years after its emergence in 2004, with a delay between the A1 and S1 SDVs. Furthermore, Zone-1 creates an undesirable SDV since it is a useless landward boundary of the beach. In comparison, Zone-2 creates a desirable SDV since it is a proper landward boundary of the beach, at least in terms of recreation. Also, compared with the JARKUS Dunefoot, Zone-1 does not show any relation with the Dunefoot dynamics. While the SDV detected for Zone-2 appears to be a predictor of the Dunefoot position. We also look into this latter observation in Section 4.1.2.
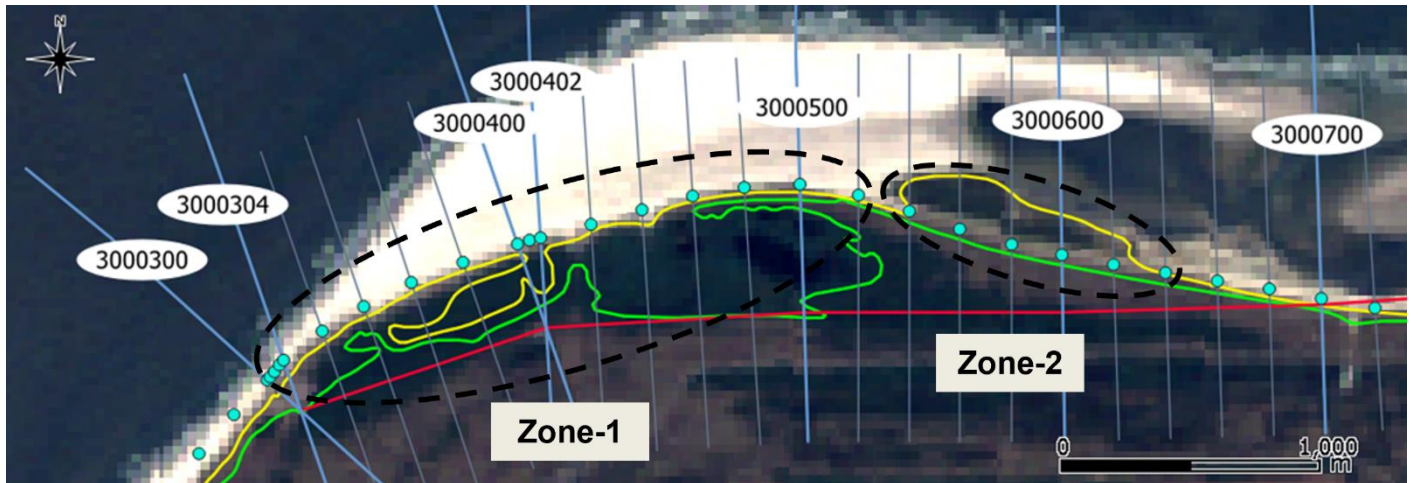

Figure 52 Close up of the dynamic area of the reach; Transects (3000)300 to (3000)700. From a 2005 Landsat 5 composite image, with the SDV-A1 in green (Threshold = 0.23) and the SDV-S1 (Threshold = 0.15) in yellow. The 2005 JARKUS Dunefoot is depicted by the turquoise circles and the RSP line in red. Zone-1 located between transects 300 and 520, and Zone-2 located between transects 540 and 640 are depicted by the black-striped ovals.

For the uniform area between transects 700 to 2100, the offsets and especially the standard deviations are smaller. When looking at the spatially averaged standard deviations for this particular area (see Table 10), we find a significant decrease for the standard deviations of both SDVs, relative to the total reach, from 60 to 35 m for the SDV-A1 and 35 to 24 m for the SDV-S1. On this part of the reach, outliers of the offset can be identified for transects 1320, 1520, 1700 and 1900 for both data sets (A1 and S1), be it with significant differences in magnitude (see Figure 50). These outliers are explained by the presence of beach inlets, which result in a landward deviation of the otherwise relatively straight SDV vectors. We expect that the Dunefoot position is not, or only slightly, affected by the presence of these inlets. Therefore, the offset between Dunefoot and SDV is more significant for those transects compared to neighbouring transects.

Table 10. Mean and standard deviation for the offset between the Dunefoot and SDV positions, between Transects 3000700 and 3002100, derived from Landsat 5 & 8 satellite images with a 30-meter pixel resolution.

Run	Threshold selection	Threshold value [-]	Section	Mean offset μ (m)	Standard deviation σ (m)
A1	Automated	$\mu = 0.27$	Total reach:	90	60
A1	Automated	$\mu = 0.27$	Uniform area:	79	34
S1	Supervised	0.15	Total reach:	49	35
S1	Supervised	0.15	Uniform area:	46	24

Based on the above findings, it is evident that the threshold value is an influential parameter in detecting the vegetation line. The results show that the SDVs from the A1 dataset with an average threshold value of 0.27

have a significantly larger average offset from the Dunefoot and a larger standard deviation than the SDVs from the S1 dataset with a fixed threshold value of 0.15. In addition, from visual inspection of SDVs of both data sets, it can be concluded that the SDV-S1 vectors not only have a smaller offset from the Dunefoot, but they are also a much better representation of the most seaward vegetation line compared to the SDV-A1 vectors. Finally, we confirm that, in general, there exists a natural offset between the Dunefoot and the vegetation line, which has to be taken in mind when looking at the offset data. In conclusion, for the remainder of this research, we detect SDVs with a supervised threshold value.

A.2 Sensitivity analysis of different supervised threshold values

Based on the results of test simulations in an early stage of this research, we selected the value 0.15 for the first supervised simulations (S1). Having examined multiple SDVs and their corresponding NDVI histograms, we formed the hypothesis that, within a specific range, lower threshold values could result in the detection of more seaward positioned SDV vectors. To assess whether those vectors are also more reliable or suitable representations of the vegetation line, we carried out a sensitivity analysis to assess the influence of small changes of the threshold value on detecting the SDV. Table 11 lists the additional simulations (S2-S5) that we do with supervised threshold values, varying from 0.14 to 0.11. For these simulations, all settings other than the threshold value are the same as simulations A1 and S1.

Table 11. Mean and standard deviation for the offset between the Dunefoot and SDV positions for different supervised threshold values for all transects of the Ameland study reach.

Run	Threshold value [-]	Mean offset μ (m)	Standard deviation σ (m)
S1	0.15	48.63	35.12
S2	0.14	45.11	31.95
S3	0.13	42.70	32.14
S4	0.12	39.20	29.65
S5	0.11	35.47	30.56

Table 11 shows the mean and standard deviation of the offset between the Dunefoot position and the SDVs detected with different threshold values. The data shows a gradual decline of the mean and standard deviation for smaller threshold values. However, visual inspection of the different SDVs shows mixed results. With lower threshold values, we detect the SDV vectors closer to the Dunefoot, but they become farther away from the 'true' vegetation line. This works well in a few cases, and wrongly detected gaps in the vegetation line become smoothened out when using lower threshold values. However, overall, the vegetation lines detected with lower threshold values represent a less realistic vegetation line and often show irregular protrusions somewhat seaward from the actual vegetation contour.

Figure 53 displays the S1 and S5 SDVs derived from August 2018 composite images, in yellow and pink, respectively, with the 2018 JARKUS Dunefoot as the turquoise dots for reference. The SDVs with the most significant difference in the threshold value, 0.15 vs 0.11, are selected to pronounce the spatial deviations between them. Figure 54 displays the NDVI histograms derived for both SDVs, from which one can notice the sensitivity of the threshold selection. Besides the remarkable protrusions, one can observe that the SDV-S5 vector, on average, shows a slightly better correspondence with the JARKUS Dunefoot but is located more seaward from the actual vegetation line than the SDV-S1 vector. The latter explains the decrease in the average offset of the SDVs with lower threshold values. However, it is certainly not an improvement for detecting the actual vegetation line. Furthermore, the difference between the standard deviations of S1 to S5 is already less prominent for lower threshold values, but when looking at the uniform area of the reach (Table 12), it becomes apparent that there is no notable difference between the standard deviations at all.
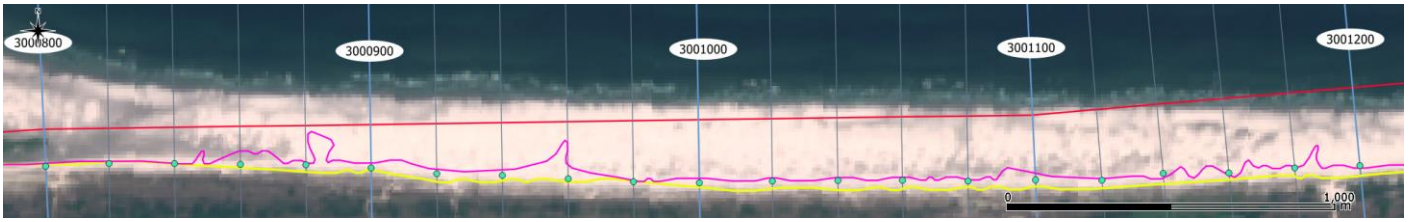
Figure 53 Example of SDVs with different threshold values; SDV-S1 (Th = 0.15) in yellow and SDV-S5 (Th = 0.11) in pink. The SDV vectors are derived from Landsat 8 composites of August 2018 and plotted on a Sentinel 2 image of August 2018 (for visibility). The 2018 dunefoot positions are displayed as the turquoise dots and the RSP line is displayed as the red line.
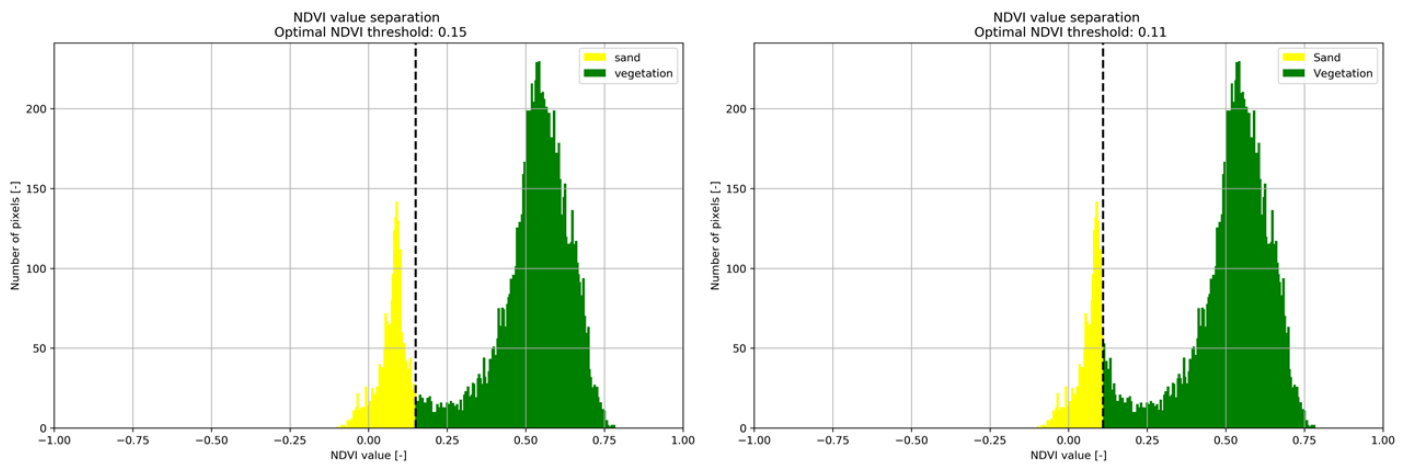

Figure 54 NDVI histograms corresponding to the SDV vectors displayed in Figure 53; SDV-S1 in the left panel and SDV-S5 in the right panel. Derived from Landsat 8 composites in the summer of 2018.

Table 12 Mean and standard deviation for the offset between the Dunefoot and SDV positions for different supervised threshold values, for transects 700 to 2100 of the Ameland study reach (The uniform area).

Run	Threshold value [-]	Mean offset μ (m)	Standard deviation σ (m)
S1	0.15	45.68	23.94
S2	0.14	43.21	23.41
S3	0.13	40.61	23.13
S4	0.12	37.70	22.75
S5	0.11	34.56	21.99

Based on the sensitivity analysis results and the visual inspection of the SDVs, we expect the optimum threshold value for detecting the most realistic vegetation line somewhere between 0.14 and 0.16. However, the differences between the corresponding SDV vectors are so minor that we can only make a sound conclusion from comparison with very accurate positional data of the vegetation. Therefore, for the time being, we consider the SDV-S1 with a threshold value of 0.15 to detect the most realistic vegetation line, be it with a larger offset from the JARKUS Dunefoot. In conclusion, we use a supervised threshold value of 0.15 for SDV detection in the rest of this report.

Appendix B − Relationship of SDV position with Vegetation cover

The data of the vegetation cover used in this analysis is provided by Dr. Ir. J.G.S. Keijsers, and was initially used for his research on the relationship between sedimentation and vegetation along the dunes of Ameland (Keijsers et al., 2015). This analysis aims to see what amount of vegetation cover corresponds with the positions of the detected SDVs and which type of NDVI threshold selection (Automated or Supervised) results in the detection of the most accurate (or realistic) SDV vectors. Based on the data used for the assessments in Appendix A, Table 13 shows the temporal data of the datasets on which the analysis in this section is focused. The vegetation cover data was extracted from 4 aerial photographs taken in either spring or summer of 2003, 2006, 2009 and 2011. In order to guarantee a clear distinction between soil and vegetation, the images were selected according to the following criteria: a suitable place in time (in the growing season), low amounts of shadow and relatively dry beach sediment (Keijsers et al., 2015). Per aerial image, elevation data from the JARKUS survey was used one year prior and two years post the capture date of each aerial image. Per transect, the percentage of vegetation cover is provided every five meters in cross-shore direction, within a range of 50 meters landward of the 2002 dune crest position and 50 meters seaward of the 2002 Dunefoot position as defined in the JARKUS survey. A notice has to be made about the shortcomings of the spatial coverage of the vegetation cover dataset. Since the spatial coverage of the data is fixed around the 2002 JARKUS Dunefoot position, the vegetation data does not adapt to substantial displacements of the Dunefoot or vegetation line position. This is unfortunate since the transects along the dynamic area of the reach show interesting dynamics for both the elevation profile and the vegetation that occur outside the spatial coverage of the data.

Table 13 Vegetation Cover data with selected satellite imagery data, time window of 90 days.

Dataset	Aerial image capture date	JARKUS Elevation data	Time window Satellite imagery	Available SDVs
2003	29 May 2003	2002-2005	14-04-2003 – 13-07-2003	1
2006	3 July 2006	2005-2008	19-05-2006 – 17-08-2006	5
2009	Summer 2009	2008-2011	17-06-2009 – 15-09-2009	4
2011	25 April 2011	2009-2012	11-03-2011 – 09-06-2011	7

In order to reduce uncertainty on the accuracy of the SDV positions and the corresponding vegetation cover values, for each transect, average positions are calculated out of all SDVs available within a window of 90 days around the capture date of the aerial images. These windows and the number of available SDVs found therein are depicted in the last two columns of Table 13 and visualized in Figure 55. For the remainder of this analysis, the 2003 dataset is excluded because of the low amount of available SDVs within the time frame. In case the position of a certain SDV is not located within the spatial range of the vegetation cover data (50 meters landward from the dune crest to 50 meters seaward from the dune foot), the value of the spatial boundary of the vegetation data closest to the SDV position is selected to accompany that SDV.
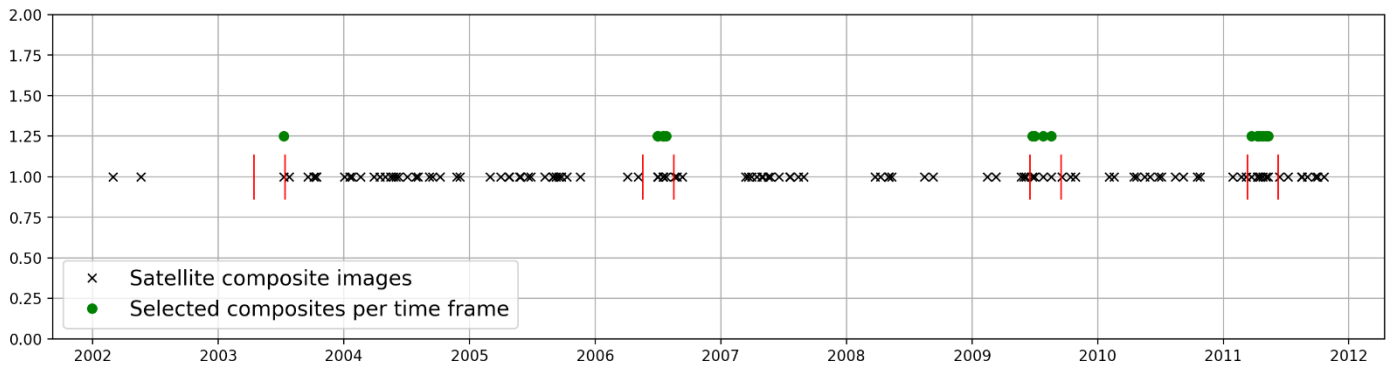
Figure 55 Available satellite composites within the selected time span of 90 days around the capture date of the aerial images

Figure 56 shows an example of the cross-shore profile of transect 920 in which the vegetation cover is plotted in green against the elevation profile for the years 2006, 2009 and 2011. Additionally, the corresponding Dunefoot position and the temporally averaged SDV positions (A1 & S1) are plotted in the figure. Although these profiles only display the data of one transect, they are exemplary for many transects along the test reach. It can be observed from the figure that the SDV-A1 is located several tens of meters landward from the natural dune foot and even further from the JARKUS Dunefoot. Those positions generally correspond to vegetation cover values of close to or exactly 100%. The vegetation cover for the positions of the SDV-S1 are characterized by lower values and a larger variability compared to the vegetation cover for the SDV-A1 positions. This can be explained by the fact that the SDV-S1 position, on average, is located closer to the Dunefoot and the most seaward vegetation line, as was demonstrated in Appendix A. In a spatial sense, this area of the beach profile is very sensitive in terms of vegetation cover. For example, within several meters on a beach profile, there can sometimes be hardly any vegetation cover around the (natural) dune foot, whereas the nearby dune front and crest are largely covered with high-density vegetation. Considering the used satellite missions have a pixel resolution of 30 meters, the detected SDVs fluctuate on a larger spatial scale than the vegetation cover data. For the SDV-S1, the overall standard deviation of the offset, $\sigma_{S1} = 35$ m, relates to the 5 m spatial resolution of the vegetation data. Figure 56 is an illustrative example of the variability of the vegetation cover data for the temporally varying SDV-S1 positions along transect 920, showing values of 40%, 20% and 80% for the subsequent years. Which displays the unfortunate drawback of the vegetation cover dataset in relation to the positional accuracy of the SDVs.
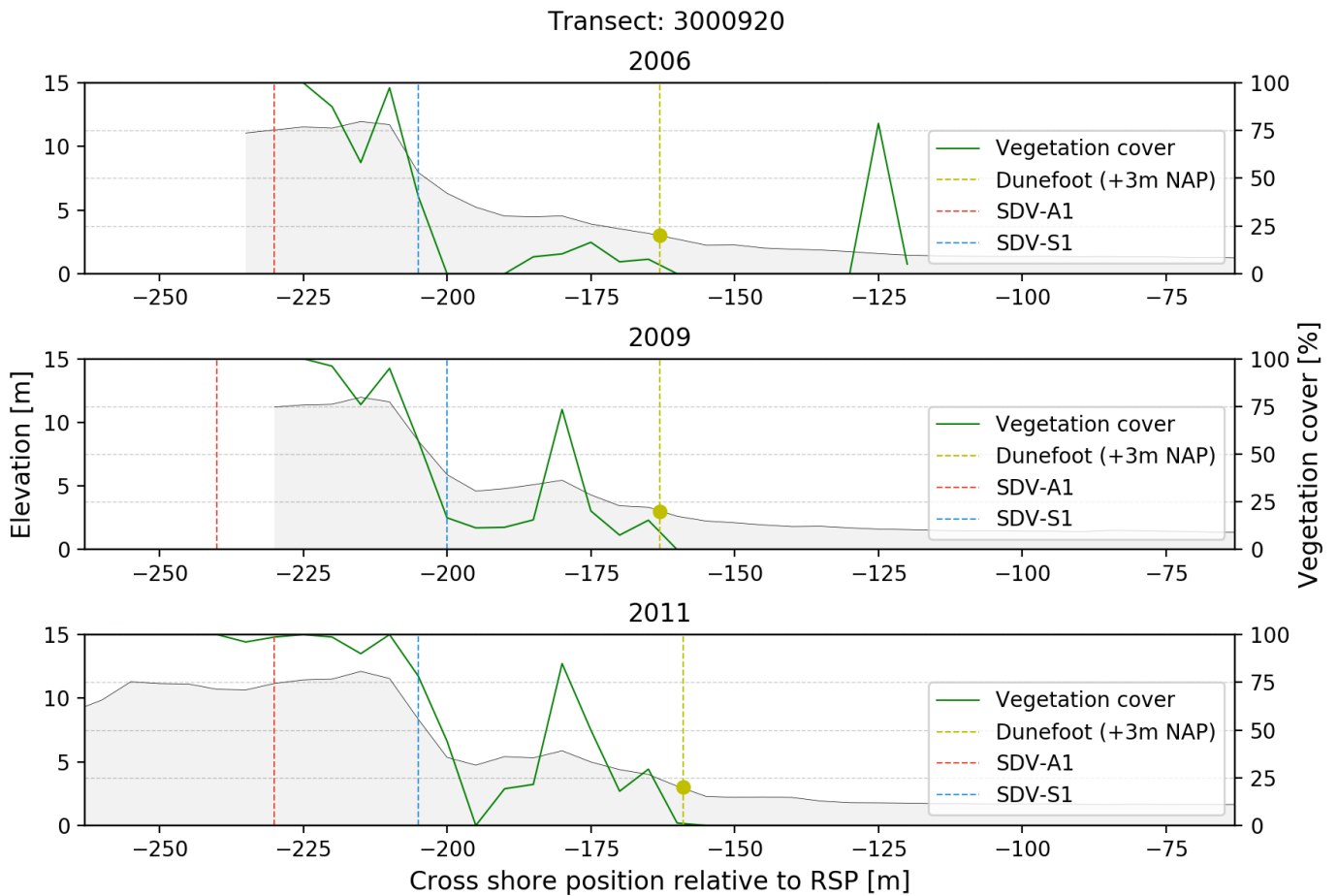
Figure 56 Vegetation cover on the cross-shore profile of Transect 920. Datasets from 2006, 2009 and 2011. Elevation relative to NAP.

The observations described above are recurring trends for both the SDV-A1 and SDV-S1, as can be observed from the overall data depicted in Figure 57. The figures display the vegetation cover data for 2006, 2009 and 2011 associated with the SDV positions (A1 & S1) on every transect on the study reach. The graphs show that the vegetation cover values related to the SDV-A1 positions, depicted as the red dots, generally show high values of vegetation cover with little variability. Contrary to the vegetation cover of the SDV-S1 positions, depicted as the blue dots, which show lower values and more variability. The graphs also display the spatial averages of the vegetation cover data for reference.
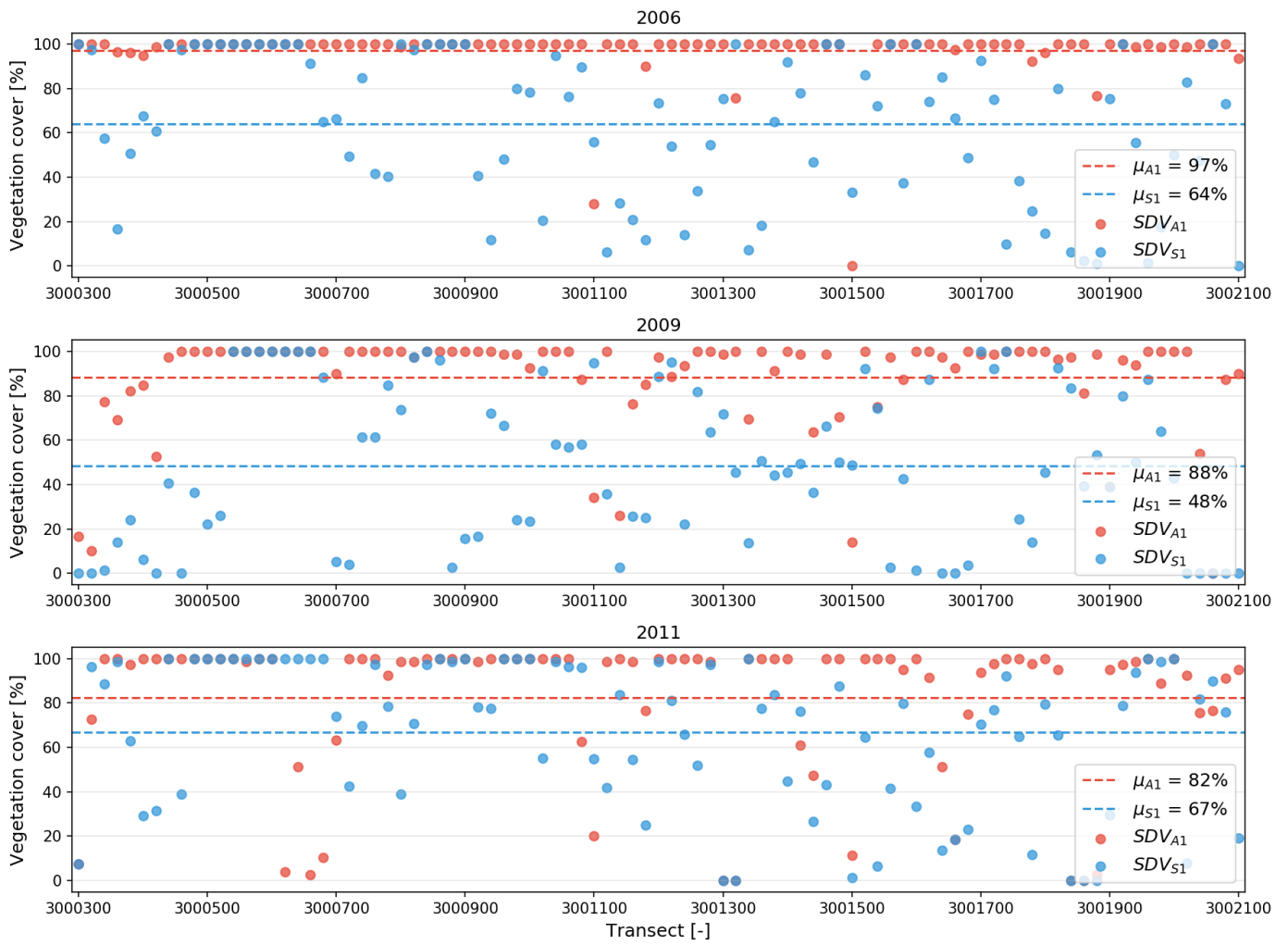
Figure 57 Vegetation cover per averaged SDV position per Transect. Datasets from 2006, 2009 and 2011

Appendix C − Image similarity algorithms

In this research, we use two algorithms to screen individual satellite images on their usability by comparing all images within a certain dataset with one "perfect" preselected image from the same dataset. These algorithms, The Structural SIMilarity Index (SSIM) measure and the Difference Percentage measure, work on the basis of similarity and can be used as an alternative to the well-known quality metric the Mean-Squared-Error (MSE) (*Percentage Difference between Images - Rosetta Code*, n.d.; Wang et al., 2004). The measures are commonly used in photography to compare a specific photograph with distorted or compressed versions of that same photograph to quantify the amount of quality loss of those alternate variants relative to the original photograph.

The degree of similarity relative to the preselected perfect image is computed for each image in a used dataset. The SSIM values range from 0 to 1.00, the higher the value, the more similar the image to the original, e.g., the "better" the quality; the Difference Percentage values range from 0% to 100%, for which a lower percentage value gives a better representation of the original. Figure 58 shows an example of three different versions of one photograph with corresponding MSE and SSIM index values. One could debate whether the image in the right panel, with the "high" SSIM index value, represents the original photo well, considering the significant difference between the background colours. Hence, we use the two metrics simultaneously to compare both outcomes and make sure an image is not falsely in- or excluded from the dataset. Images are deemed usable if the image has an SSIM score higher than 0,80 and a Difference Percentage lower than 10%. Images that satisfy neither of the two demands are directly deemed unusable and thus omitted. Images that satisfy either one of these two demands are manually inspected after the screening.
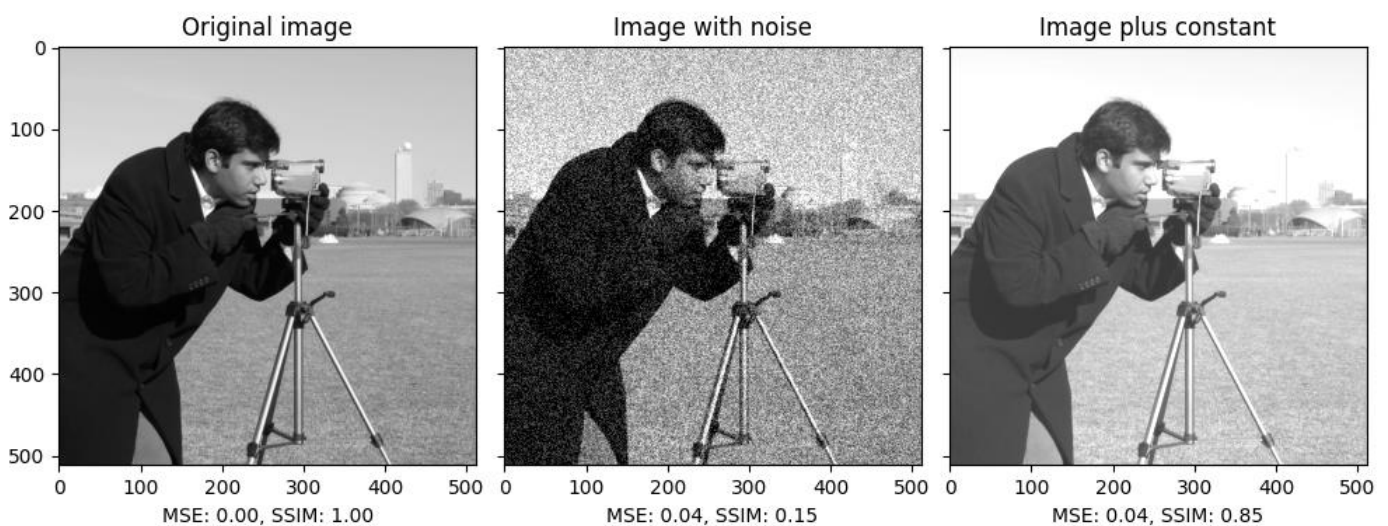
Figure 58. Example of three different versions of one photograph, with different SSIM index values. From "scikit-image", n.d. (https://scikit-image.org/docs/dev/_images/sphx_glr_plot_ssim_001.png) © Copyright by the scikit-image development team.

By using this qualitative screening, we filter out images corrupted by undetected or unfiltered cloud cover and satellite instrument errors. On the satellite images, these errors are primarily of a significantly larger scale relative to actual changes of, for example, the shoreline and vegetation line. Therefore, this screening method is not likely to filter out shoreline or vegetation line dynamics. The threshold values for omitting bad images are set so that morphological changes do not result in unnecessary omittance of good images.

Figure 59 shows the image we selected during the pre-screening of the satellite image dataset used for the analyses in Section 4.2. Figure 60 displays three examples of satellite images (including SDS and SDV) from

that dataset with a very low Cloud Cover percentage that we classified as unusable and were therefore omitted from the analyses. Figure 61 displays three examples of satellite images (including SDS and SDV) of the same dataset with a (very) high Cloud Cover percentage that we classified as usable and were therefore included in the analyses. When using composite images with a max Cloud Cover percentage of say 60%, the unusable images from Figure 60 would be included in the composites and would significantly reduce the quality of a sequence of composites, whereas the usable images of Figure 61 are excluded from the composites.

2016-03-12 10:50:37

CC: 20,68%   SSIM: 1,00   Diff: 0,0%

Figure 59 "Original" image that was selected as the base image for the screening of individual Sentinel-2 images in the analyses in Section 4.2

2018-12-04 10:46:02
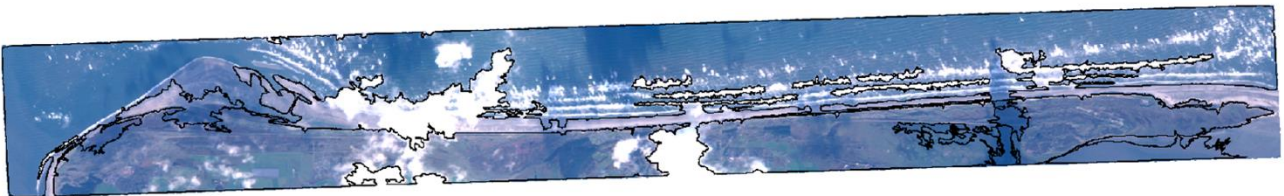
CC: 1,24%   SSIM: 0,71   Diff: 11,19%

2018-08-21 10:40:15
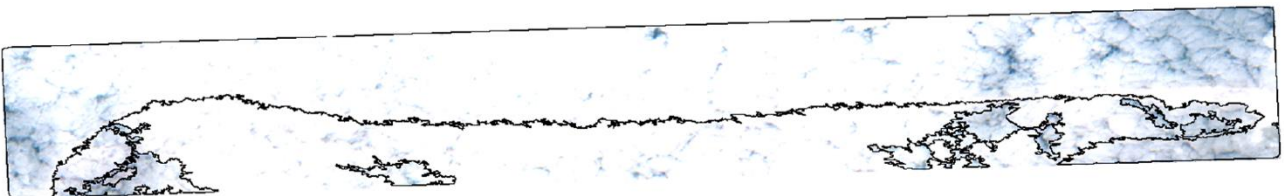
CC: 10,37%   SSIM: 0,65   Diff: 26,30%

2017-08-06 10:40:21
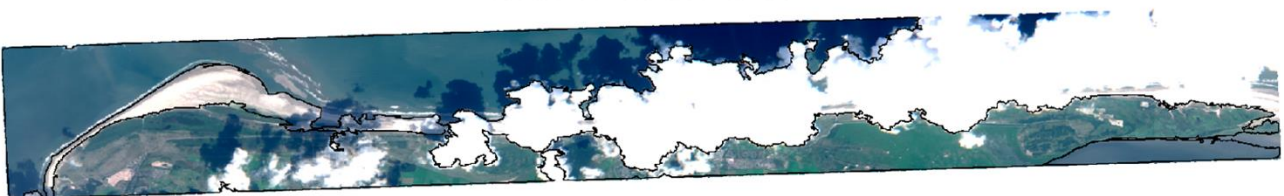
CC: 13,07%   SSIM: 0,75   Diff: 12,94%

Figure 60 Three Sentinel-2 images with very low Cloud Cover percentages that are classified as unusable. From the dataset used for the analyses in Section 4.2

2018-04-06 10:53:31

CC: 93,21%   SSIM: 0,83   Diff: 9,6%

2018-01-21 10:54:28

CC: 85,56%   SSIM: 0,86   Diff: 6,92%

2017-08-14 10:55:17

CC: 67,59%   SSIM: 0,89   Diff: 3,55%

Figure 61 Three Sentinel-2 images with (very) high Cloud Cover percentages that are classified as usable. From the dataset used for the analyses in Section 4.2

Appendix D − SDV-dynamics along the *dynamic* area

To help understand the explanation of the results below, a satellite image of the dynamic area from August 2018 is shown in Figure 62 with a high pixel resolution (4.8m). The figure includes the 2006 and 2018 JARKUS Dunefoot positions for reference. Figure 63 to Figure 77 show the time series of Transects 420 to 700 further below in this Appendix. We note several things about the long-term trends of the Dunefoot and SDVs on the dynamic area of the reach. We observe positive feedback between sedimentation and vegetation growth. The time series of transects 440 to 520 show the establishment of incipient dunes due to sedimentation, which at some point in time attain the +3-meter contour and are then recognised as the Dunefoot in the JARKUS data. These incipient dunes appear around 200 meters seaward from the preceding Dunefoot. From satellite images shortly after the August 2018 image (summer/fall 2018), we observe young sparsely spread vegetation patches landward from these incipient dunes and are not always detected by the SDV detection method.
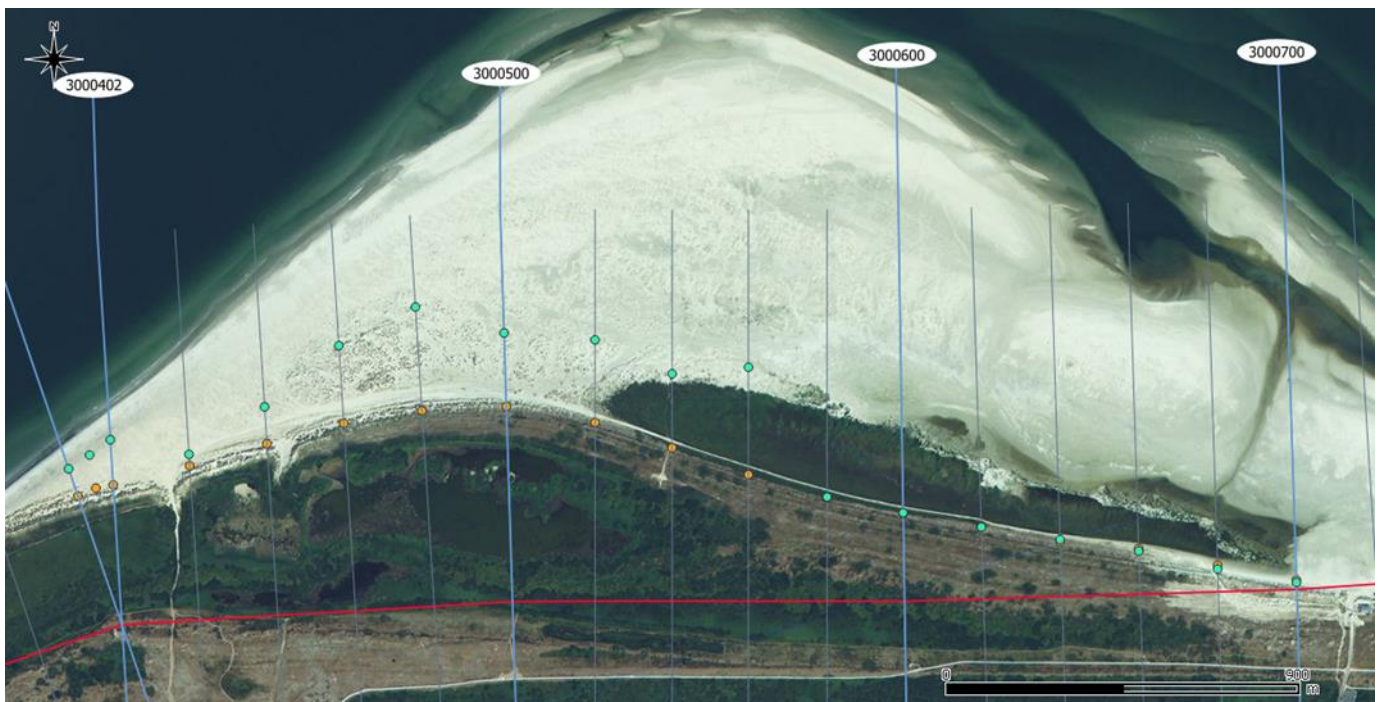
Figure 62 This image shows a close-up of the dynamic part of the study-site, between transects 3000400 and 3000700. With the RSP line in red and the transects in blue. The JARKUS Dunefoot positions are shown for the year 2006 in orange and for the year 2018 in turquoise. (TripleSat image, 80cm pixel resolution, August 2018, acquired from www.satellietdataportaal.nl).

Between transects 540 and 680, we observe a reverse process. From the corresponding time series, we observe a characteristic expansion of the vegetation (the salt marsh "Het Groene Strand") that appeared in 2004. The time series of the transects for this specific area all show an abrupt change of the SDV position in that year. In this case, the change of the vegetation line position precedes the sedimentation. For transects 540 and 560, the elevation profile, and the Dunefoot position, catches up with the vegetation between 2010 and 2012. Hence, after a few years, the +3-meter contour transverses towards the new seaward boundary of the vegetation. At the time the data was simulated and analysed, the elevation profile had not yet caught up with the vegetation cover for transects 580 to 680.

These findings show the significant differences between the long-term trends on the western end of the study site, depicted in Figure 28. The latter holds especially for the transects 580 to 680, where the Dunefoot has not yet caught up with the vegetation line. Furthermore, it also holds for transects 460 to 520 where (in recent years) sedimentation resulted in a seaward shift of the +3-meter contour that has not been caught up (yet) by a more seaward vegetation contour (SDV). These (natural) delays measured between the sedimentation and the vegetation growth, in either temporal direction, causing the differences between the long-term trends, are not necessarily a bad thing. An (abnormal) change in the elevation profile observed in the long-term trends of the Dunefoot could act as a predictor of vegetation growth (embryonal dunes) and vice-versa.
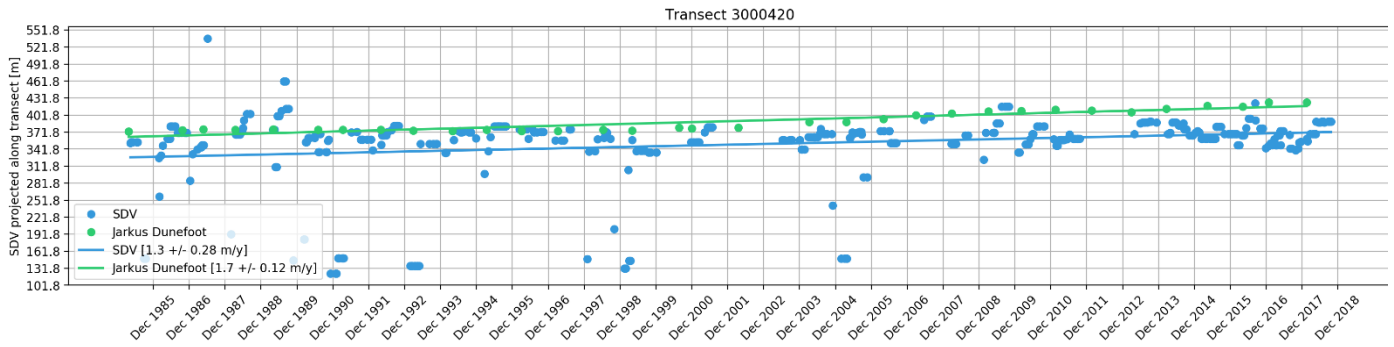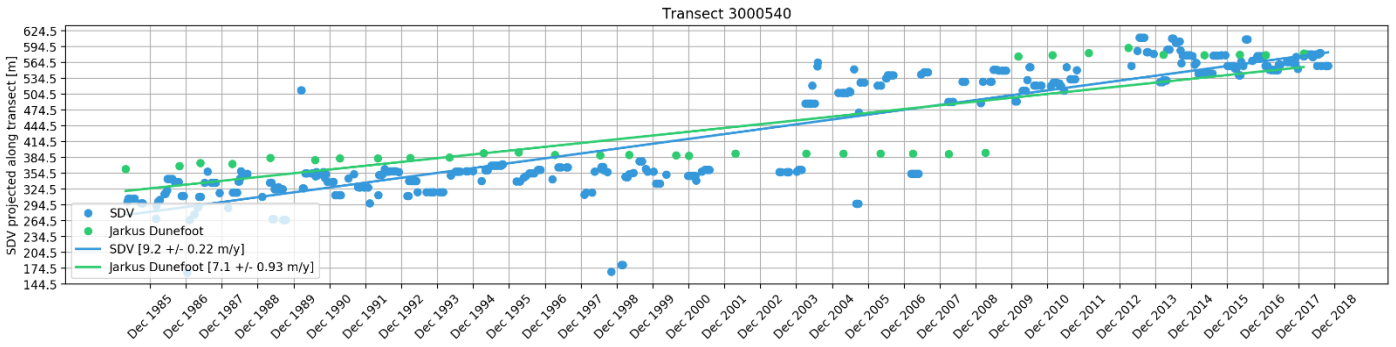

Figure 63 Position and Long-term trends of the Dunefoot and SDV along Transect 420
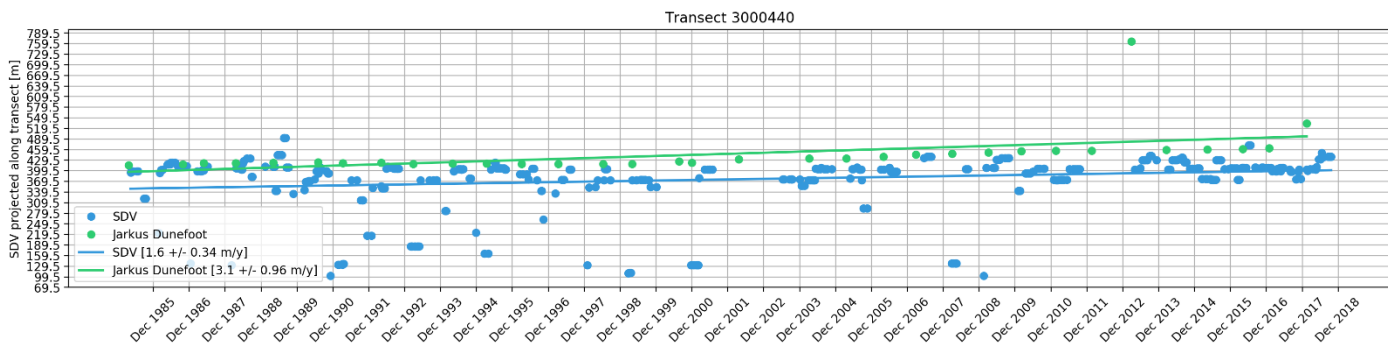
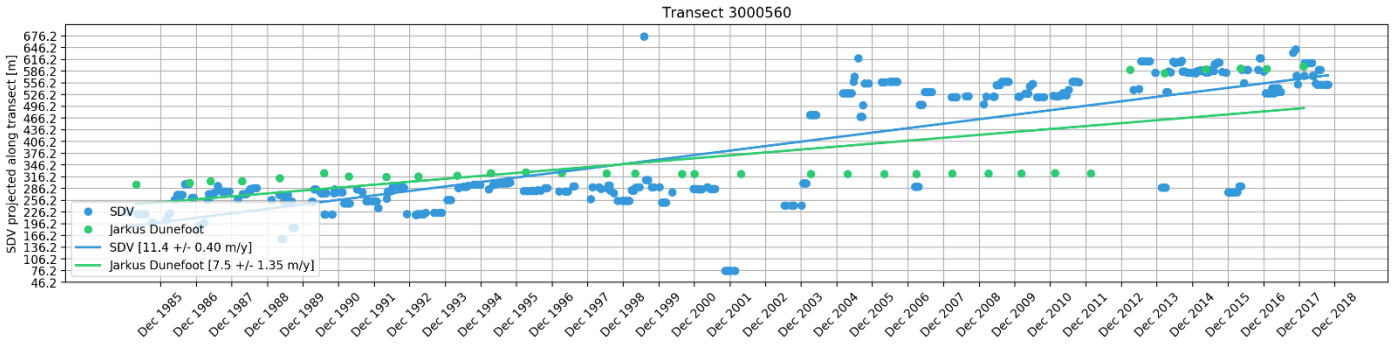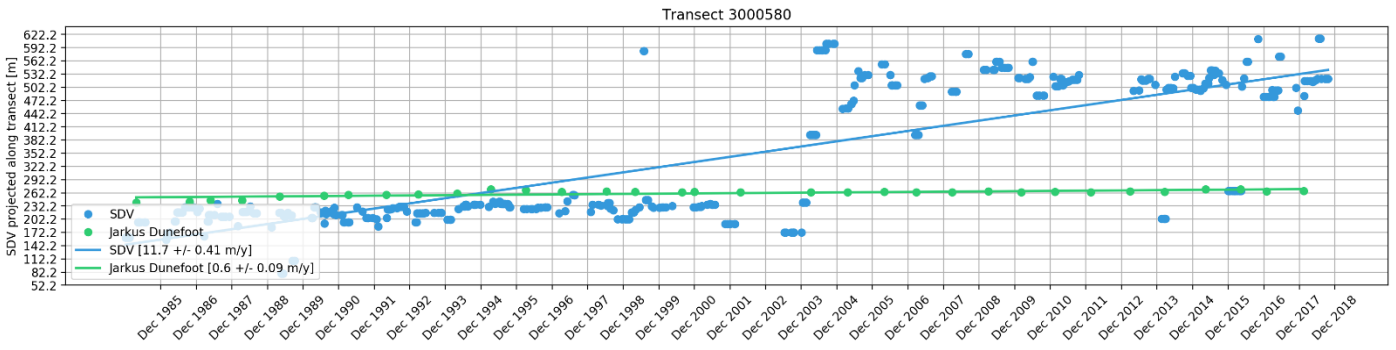*Figure 64 Position and Long-term trends of the Dunefoot and SDV along Transect 440*
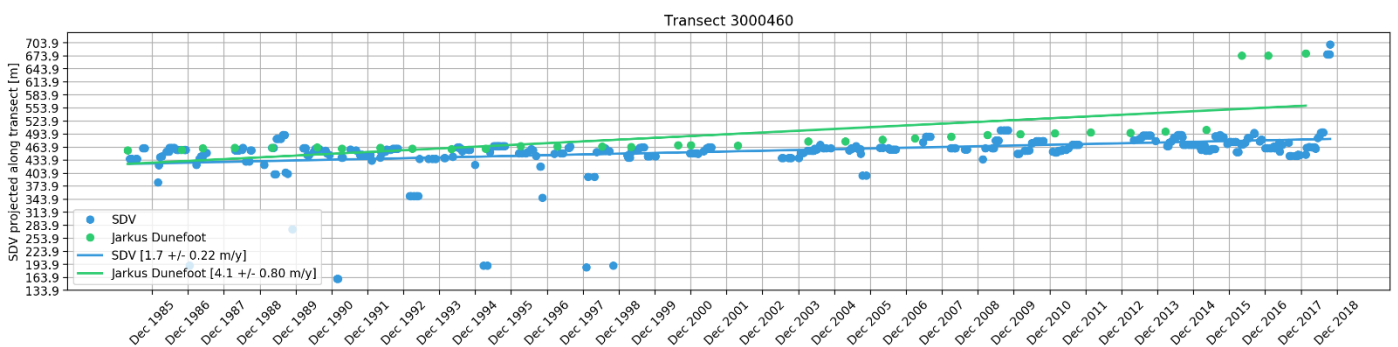
Figure 65 Position and Long-term trends of the Dunefoot and SDV along Transect 460
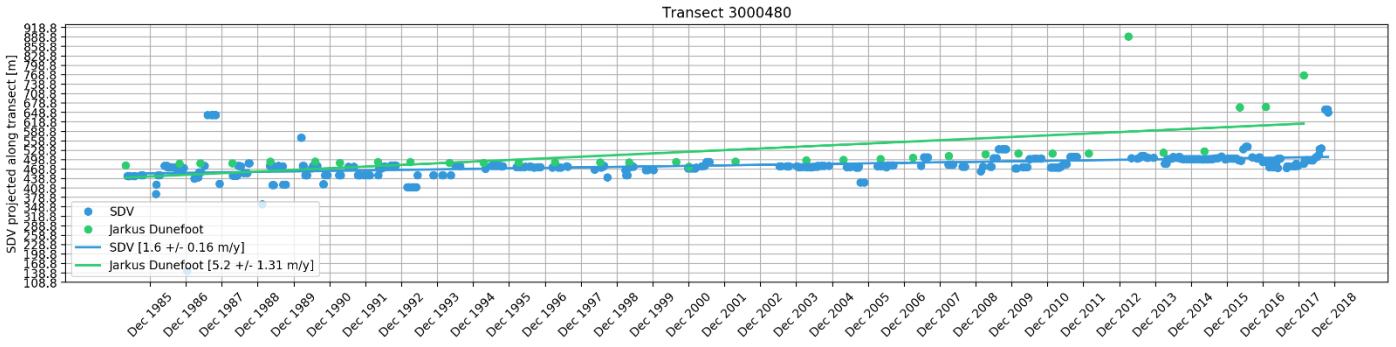
Figure 66 Position and Long-term trends of the Dunefoot and SDV along Transect 480

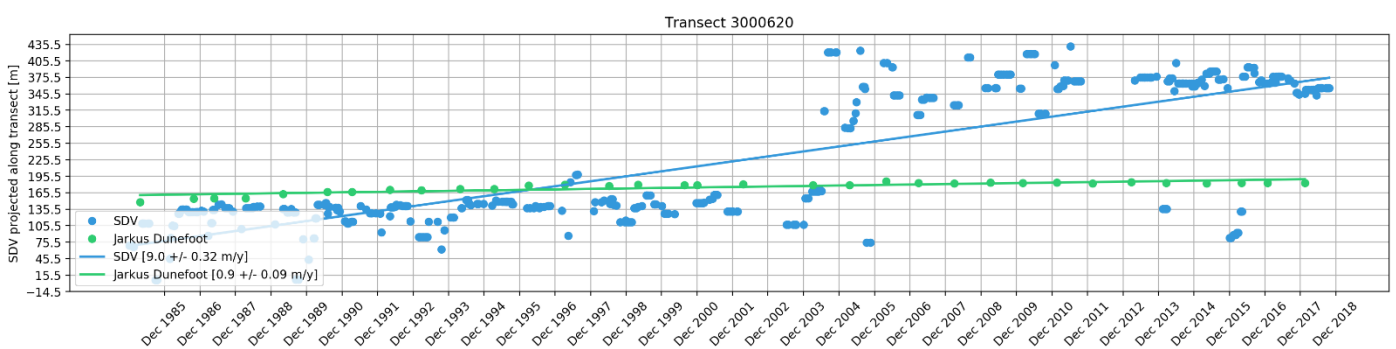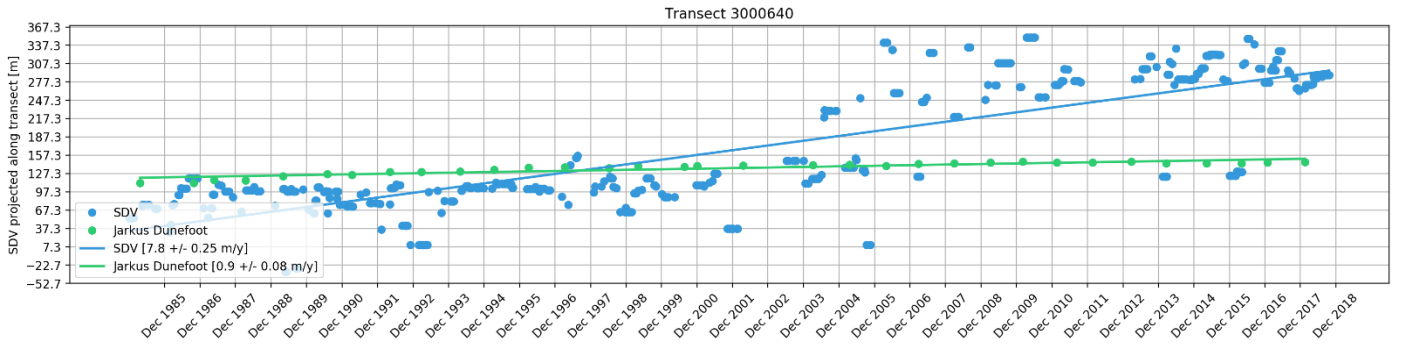*Figure 67 Position and Long-term trends of the Dunefoot and SDV along Transect 500*

Figure 68 Position and Long-term trends of the Dunefoot and SDV along Transect 520

Figure 69 Position and Long-term trends of the Dunefoot and SDV along Transect 540

Figure 70 Position and Long-term trends of the Dunefoot and SDV along Transect 560

Figure 71 Position and Long-term trends of the Dunefoot and SDV along Transect 580

Figure 72 Position and Long-term trends of the Dunefoot and SDV along Transect 600

Figure 73 Position and Long-term trends of the Dunefoot and SDV along Transect 620

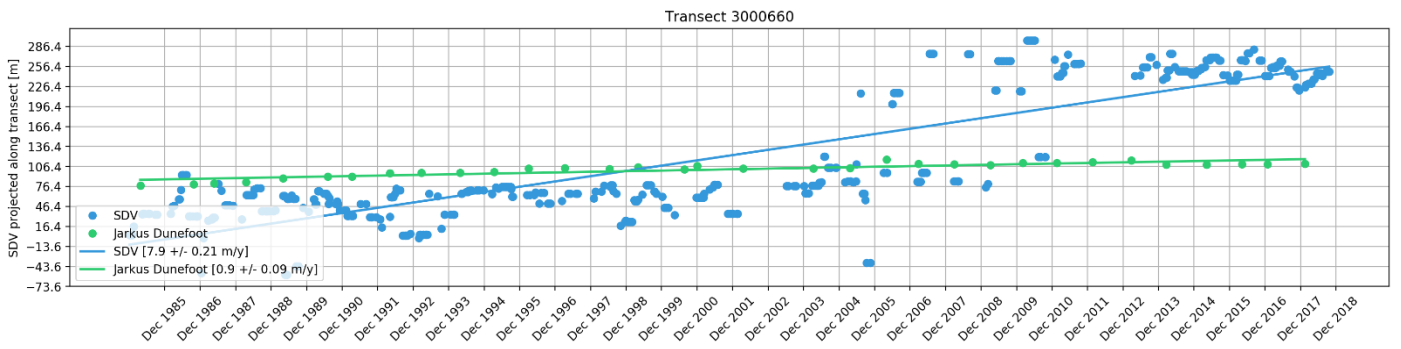*Figure 74 Position and Long-term trends of the Dunefoot and SDV along Transect 640*

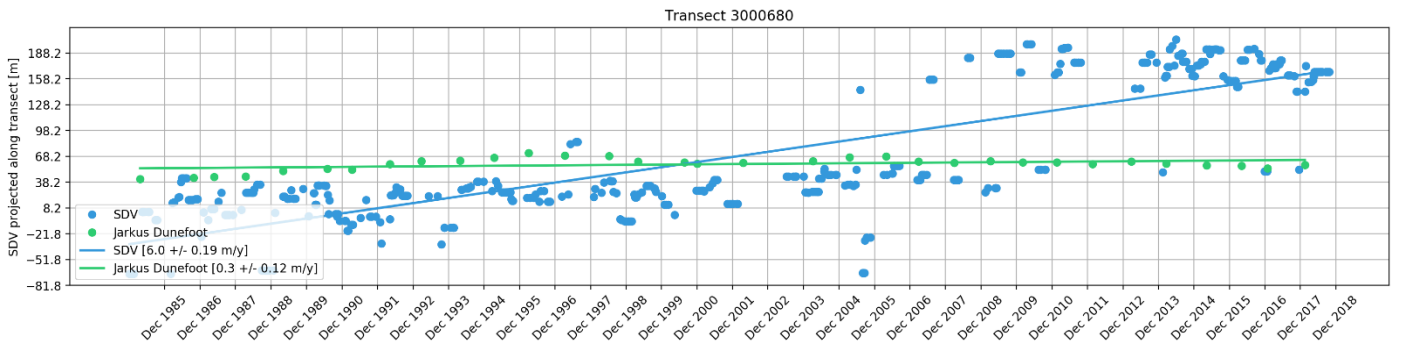*Figure 75 Position and Long-term trends of the Dunefoot and SDV along Transect 660*

Figure 76 Position and Long-term trends of the Dunefoot and SDV along Transect 680
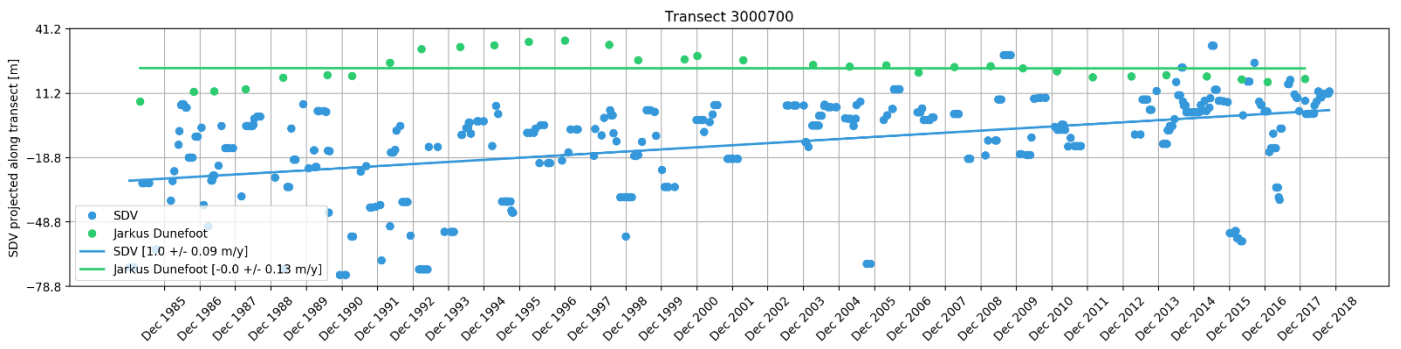

Figure 77 Position and Long-term trends of the Dunefoot and SDV along Transect 700